

CONTROLLABILITY OF ELECTROSPINNING AND
ELECTROSPRAYING - ADVANCES AND APPLICATION

SEBASTIAN HEINZ GERHARD NEUBERT

NATIONAL UNIVERSITY OF SINGAPORE

2010

CONTROLLABILITY OF ELECTROSPINNING AND
ELECTROSPRAYING - ADVANCES AND APPLICATION

SEBASTIAN HEINZ GERHARD NEUBERT

(Diplom-Ingenieur, TUM)

A THESIS SUBMITTED

FOR THE DEGREE OF MASTER OF ENGINEERING

DEPARTMENT OF MECHANICAL ENGINEERING

NATIONAL UNIVERSITY OF SINGAPORE

2010

Acknowledgements

The following research work was done in the “Healthcare and Energy Material Laboratories” (HEM) at Nanoscience and Nanotechnology Initiative (NUSNNI) and the Department of Mechanical Engineering at the National University of Singapore (NUS). The author would like to acknowledge and express his utmost gratitude to his project supervisor Prof. S. Ramakrishna, NUS Vice-President and Head of Healthcare and Energy Materials Laboratory for his guidance, his support and the fruitful discussions.

In addition, the author thanks all lab mates for the excellent collaboration and partnership in research. Especially, he thanks the research fellow Dr. D. Pliszka for his mentorship, his contributions and the numerous scientific discussions. In addition, he thanks Dr. V. Thavasi, Manager of Nanoscience – and Nanotechnology Initiative (NUSNNI), for his cooperation and the numerous discussions with him. Besides, he would like to thank the research fellows Dr. J. Venugopal, Dr. M. Prabhakaran and Dr. S. Sundarrajan for their help in the experimental part of his work. Furthermore, he thanks Ing. Cand. Stefan Grott, exchange student at NUSNNI from TUM, for his cooperation on the field of biocompatibility testing.

The author would like to acknowledge Prof. E. Wintermantel, Professor ordinarius of the Department and Institute of Medical Technology at TU Munich (TUM). He introduced the author to Prof. S. Ramakrishna and therefore deserves his utmost gratitude.

The author thanks the “German Academic Foundation” as well as the Dr. Jürgen Ulderup Foundation for their generous financial support of his stay at the National University of Singapore (NUS).

The author has special gratitude for his family for their encouragement and support for pursuing all endeavors.

Table of Contents

Acknowledgements	I
Table of Content	II
Summary	V
List of Scholarships and Awards	VII
List of Tables	VIII
List of Figures	X
List of Symbols	XV
1. Introduction	1
1.1 Motivation and aim	1
1.2 Thesis structure	5
2. Experimental techniques	7
2.1 Electrospinning	7
2.2 Electrospaying	10
2.3 Characterization	14

3.	Focused fibers deposition by electrospinning	17
3.1	Experimental details	17
3.1.1	Materials	17
3.1.2	Membrane fabrication	18
3.2	Results	19
3.2.1	Electrostatic lens systems	20
3.2.1.1	Single ring electrode	25
3.2.1.2	Guard electrode	27
3.2.1.3	Combinations of ring and tube electrodes	27
3.2.1.4	Geometry of the electrospinning setup	29
3.2.2	Optimized setup	31
3.3	Discussion	34
4.	Patterning with electrospinning	36
4.1	Experimental details	36
4.1.1	Materials	36
4.1.2	Membrane fabrication	37
4.1.3	Biocompatibility test	42
4.2	Results	45
4.2.1	Impact of setup design on pattern structure	45
4.2.2	Fibers morphology	63
4.2.3	Mechanical properties of the fibers structure	71
4.2.3.1	Elasticity	76
4.2.3.2	Tensile strength	81
4.2.4	Cell culturing with cardiomyocytes	83
4.3	Discussion	87

5.	Controllability of electro spraying	92
5.1	Experimental details	92
5.1.1	Materials	92
5.1.2	Membrane fabrication	94
5.2	Results	96
5.2.1	CSA doped PANi-PEO fibers	96
5.2.2	Effect of collectors on the adhesion of TiO ₂ nanoparticles	98
5.2.3	Catalytic performance of TiO ₂ -PANi-PEO fibrous membrane	103
5.3	Discussion	107
6.	Conclusions and future perspectives	109
	Appendix 1	111
	Bibliography	117

Summary

In this thesis, methods to control electrospinning and electrospaying are presented. Controllability of these processes is defined as the possibility of fibers deposition at a small spot as well as the capability to pattern fibers patterns.

Electrospinning of various polymers is focused by modifying the electric field with electrostatic lens systems consisting of additional ring, guard and tube electrodes to enhance the precision of electrospinning. Fibers deposition spot size with a diameter 3-4 mm are achieved. On moving collectors, fibers lines with a width of 0.15 ± 0.013 mm are fabricated. Additional electrodes are also found to be useful to control the pore size of electrospun fibers membranes.

To control the polymer electrospinning jet for patterning, switchable steering electrodes are introduced into the standard electrospinning setup. They are charged at a defined frequency with high voltage. Due to the switchable charging of the steering electrodes, the electrospinning polymer jet is set into a state of controllable oscillation. Control over the movement of the polymer jet in one direction is gained with one pair of steering electrodes. In one dimension, the polymer jet is controlled at the maximum over a width of ~33 mm. Two dimensional control is achieved with two pairs of steering electrodes acting perpendicular to each other. Square patterns with a size ~13 mm were achieved. The impact of the process parameters like frequency of the voltage signal, the voltage applied at the steering electrodes or by the geometric dimensions of the steering electrodes on the geometric dimensions of the patterns is shown. With defined fibers orientation, the mechanical properties are made more controllable with this method.

With the help of the steering electrodes, not only the fibers structure could be determined and modified, but also the fibers morphology. A buckling fibers morphology is observed for electrospinning. The combination of buckling structure and fibers patterns improves the elasticity of the fibrous membrane from an E-modulus ~19 MPa for random

fibers structure to ~2 MPa for patterns fibers with buckling morphology and does not affect the tensile strength. The E-modulus is further reduced to ~1 MPa by exposure to cell culture medium in order to model the cell culturing conditions for the fibrous membranes.

The mechanical properties are discussed for application in cardiac tissue engineering.

Electrospraying deposition is controlled by attracting the dispersed droplets on a nanostructured conductive collector. Controllability of droplet deposition at nanoscale is shown for electrospraying. The resulting composite structure is evaluated for photocatalytic application.

Controlled electrospraying is used for coating a porous fibrous membrane with photocatalytic TiO₂ nanoparticles. Besides the investigation of the fabrication mechanism, the mechanical stability and the photocatalytic activity are studied. This membrane combines the function of detoxification as well as filtration and therefore contributes to the protection of human health.

The developed methods to enhance controllability of electrospinning and electrospraying are tested for applications to protect and recover human health. The electrospun patterned fibers structures with buckling morphology are investigated to evaluate their potential for application as cardiac tissue engineering patch scaffold to recover myocardial infarction. Besides the structural, morphological and mechanical characterization, the biocompatibility of the membranes was tested with cardiomyocytes.

List of Scholarships and Awards

1. Fellowship of the German Academic Foundation
(Studienstiftung des deutschen Volkes)
2. Scholarship funded by the Dr. Juergen Ulderup Foundation for Master of
Engineering Program at the National University of Singapore (NUS)

Conference contributions

1. „Precise Patterning by Electrospinning – A Novel Tool for Tissue Engineering“
D. Pliszka, S. Neubert, S. Grott, S. Ramakrishna
MRS-S Trilateral Conference on Advances in Nanoscience:
Energy, Water and Healthcare, Aug. 11-13, Singapore

List of Tables

- Table 1.** Impact of ring electrode position with $d = 33$ mm on the fibers spot size and fibers diameter.
- Table 2.** Impact of varying position of the guard electrode on the spot size and the fiber quality. PVC solution A was electrospun with a flow rate 1.0 ml/h.
- Table 3.** Correlation between the elements of the electrostatic lens system, their combination, the applied voltages V_1 and V_2 and the fibers spot diameter. For all configurations, PVC solution A, a flow rate 1.0 ml/h and $D = 100$ mm were applied.
- Table 4.** Impact of the distance D between the spinneret tip and the collector on the fibers spot size. For all configurations, PVC composition A and a flow rate 1.0 ml/h were applied.
- Table 5.** Nylon, PLACL and PVC fibers were electrospun with $D = 70$ mm and a flow rate 1.0 ml/h. Components of the electrostatic lens system: guard electrode with $d = 50$ mm positioned at $x = -10$ mm, ring electrode 1 with $d = 25$ mm positioned at $x = 1$ mm and ring electrode 2 with $d = 30$ mm and positioned at $x = 17$ mm.
- Table 6.** Pattern width W_p fabricated with one pair of steering electrodes on a moving collector ($V_1 = 11.8$ kV; $V_2 = 11.5$ kV; $W = 12.5$ mm; $x_I = 5$ mm; $x_{II} = 20$ mm; $a = 50$ mm). With increasing frequency of the voltage signal f , the pattern width decreased.
- Table 7.** Pattern width fabricated with two pairs of flat steering electrodes ($V_1 = 11.8$ kV; $V_2 = 11.5$ kV; $W = 6.25$ mm; $x = 15$ mm; $a = 50$ mm). With increasing frequency f of the voltage signal the geometric dimensions of the fibers patterns (length L_p and width W_p) were decreased.
- Table 8.** Pattern width fabricated with two pairs of circular steering electrodes ($V_1 = 11.8$ kV; $V_2 = 11.5$ kV; $W = 12.5$ mm; $x = 10$ mm). Increasing voltage signal frequency f and increasing diameter of the circular electrodes resulted in smaller fibers patterns (length L_p and width W_p).
- Table 9.** Effect of plasma treatment on the fibers diameter and the hydrophilic characteristics of random and aligned PLACL fibers.

Table 10. E-modulus without DMEM

Table 11. E-modulus after 15 days exposure to DMEM.

Table 12. The E-modulus in AP direction of membranes fabricated with one pair of steering electrodes ($V_1 = 11.8$ kV; $W = 12.5$ mm; $x_I = 5$ mm; $x_{II} = 20$ mm; $a = 50$ mm). f and V_2 were the varied parameters. The E-modulus was compared with the maximum slope (Formula 7) of the function approximating the fibers wave pattern numerically (Formula 6).

Table 13. Tensile strength of the PLACL membranes with different structures and morphologies; non-plasma treated (N), and plasma treated (P) without DMEM exposure and after 15 days of DMEM exposure.

Table 14. The tensile strength in AP direction (AP: perpendicular to fibers wave direction) of membranes fabricated with one pair of steering electrodes ($V_1 = 11.8$ kV; $W = 12.5$ mm; $x_I = 5$ mm; $x_{II} = 20$ mm; $a = 50$ mm). f and V_2 were the varied parameters. The E-modulus was compared with the maximum slope (Formula 7) of the sine function approximating the wave pattern numerically (Formula 6).

Table 15. Composition of electrospun CSA/PANi-PEO solutions.

List of Figures

- Figure 1.** Structure of the thesis.
- Figure 2.** The polymer fiber is stretched from the spinneret tip on its way to the collector
a) Schematic drawing of standard electrospinning setup and electrospinning, and
b) photography of polymer jet during electrospinning.
- Figure 3.** For electrospaying, the solution breaks up into droplets directly at the needle tip and are dispersed.
- Figure 4.** Modes of electrospaying (Jaworek and Sobczyk, 2008).
- Figure 5.** The droplet size distribution of droplets close to the needle tip for electrospaying of solution of 5% (w/v) TiO₂ nanoparticles concentration and an electrospaying voltage of 6 kV (Pliszka et al. (2008)).
- Figure 6.** Gold electrode with a 5 μm distance on silica substrate.
- Figure 7.** Setup for electrospinning of polymer fibers with electrostatic lens system.
- Figure 8.** Equipotential lines in the spinneret - focusing ring - collector system:
a) ring at x = -15 mm, b) ring at x = 0 mm, and c) ring at x = 10 mm with voltage 25 kV.
- Figure 9.** Pore sizes without any additional electrode, with additional ring electrode (x = -15 mm) and with additional ring electrode (x = 0 mm) for Nylon, PCL, PLACL, and PVC.
- Figure 10.** Fibers electrospun under optimized conditions (Table 5) with flow rate 1.0 ml/h and D = 70 mm on a static collector. Components of the electrostatic lens system: guard electrode with d = 50 mm positioned at x = -10 mm, ring electrode 1 with d = 25 mm positioned at x = 1 mm and ring electrode 2 with d = 30 mm and positioned at x = 17 mm a) modelling, b) fibers spot size (PVC solution B), c) morphology of PVC solution B, and d) morphology of Nylon fibers.

-
- Figure 11.** PLACL fibers electrospun under optimized conditions (Table 5) with a flow rate 1.0 ml/h and $D = 70$ mm on a collector moving with ~ 0.1 m/s. Components of the electrostatic lens system: guard electrode with $d = 50$ mm positioned at $x = -10$ mm, ring electrode 1 with $d = 25$ mm positioned at $x = 1$ mm and ring electrode 2 with $d = 30$ mm and positioned at $x = 17$ mm. The fibers line had a width of 0.158 ± 0.013 mm.
- Figure 12.** Setup with one steering electrode pair. The distance between one pair of steering electrodes was denoted as a . The collector moved in line with the steering electrodes with a speed v .
- Figure 13.** Setup with two steering electrode pairs using a) flat electrodes design, and b) circular electrodes design.
- Figure 14.** Principle of the electro-mechanical controller.
- Figure 15.** Voltage signal provided by the electro-mechanical controller. At all four channels A, B, C and D, the same voltage signal was provided shifted by 0.5π , π and 1.5π to the reference voltage signal (Channel A).
- Figure 16.** Electronic principle of the steering electrodes. The controller (Figure 14) provided the RC-circuit consisting of a condensator and resistor with a defined voltage signal. The condensator and the resistor represent the electric field and the resistance R_{tot} between one steering electrode and the grounded collector respectively.
- Figure 17.** Design 1: For $R_{\text{tot}} \rightarrow \infty$, the expected voltage signal remains with the steering electrodes remaining charged (qualitative estimation).
- Figure 18.** Design 2: For $R_{\text{tot}} = 150 \text{ M}\Omega - 300 \text{ M}\Omega$, the expected voltage signal provided by the mechanical controller (qualitative estimation).
- Figure 19.** Single jet PLACL fiber extracted from the spinneret tip a) without steering electrodes ($V_1 = 11.8$ kV), and b) with one pair of flat steering electrodes ($V_1 = 11.8$ kV; $V_2 = 11.5$ kV; $W = 12.5$ mm; $x_1 = 5$ mm; $x_{11} = 20$ mm; $a = 50$ mm).
- Figure 20.** Distance between steering electrodes a) $a = 50$ mm, b) $a = 75$ mm and c) $a = 100$ mm with the following constant parameters ($V_1 = 11.8$ kV; $V_2 = 11.5$ kV; $W = 12.5$ mm; $x = 10$ mm).

-
- Figure 21.** Voltage applied at the steering electrodes a) $V_2 = 7.5$ kV, b) $V_2 = 9.5$ kV, c) $V_2 = 11.5$ kV and d) $V_2 = 13.5$ kV with the following constant parameters ($V_1 = 11.8$ kV; $W = 12.5$ mm; $a = 50$ mm; $x = 10$ mm).
- Figure 22.** The wave fibers structure fabricated with a one pair of steering electrodes and a moving collector was described by the period length (l_p) and the pattern width (W_p). Within this study, AP indicated the direction perpendicular to the wave structure and AA the direction in line with the wave structure.
- Figure 23.** Electrospinning was controlled by two pairs of electrodes with the electrodes A and C as well as B and D being charged in phase. A linear diagonal pattern was fabricated with two pairs of electrodes ($V_1 = 11.8$ kV; $V_2 = 11.5$ kV; $W = 6.25$ mm; $a = 50$ mm; $x = 15$ mm).
- Figure 24.** Fibers morphology of a) random fibers ($V_1=11.8$ kV), b) fibers aligned by deposition on rotating drum ($V_1=11.8$ kV), and c) wave structured fibers with buckling morphology fabricated with one pair of steering electrodes. ($V_1 = 11.8$ kV; $V_2 = 11.5$ kV; $W = 12.5$ mm; $x_I = 5$ mm; $x_{II} = 20$ mm).
- Figure 25.** Buckling fibers morphology achieved for fibers controlled with one steering electrode pair or two steering electrode pairs a) buckling structure, and b) overview SEM image ($V_1 = 11.8$ kV; $V_2 = 11.5$ kV; $W = 12.5$ mm; $x_I = 5$ mm; $x_{II} = 20$ mm).
- Figure 26.** Impact of plasma treatment on the fibers morphology a) random PLACL fibers before plasma treatment, and b) random plasma fibers after plasma treatment.
- Figure 27.** Effect of plasma treatment on the pore size of a) random PLACL fibrous membrane, b) aligned PLACL fibrous membrane collected on a rotating drum, c) PLACL fibrous membrane deposited with one steering electrode pair, and d) PLACL fibrous membrane deposited with two steering electrode pairs.
- Figure 28.** Stress (σ)-strain (ϵ) curves of random fibers structure fabricated with a $V_1 = 11.8$ kV (Same scale for all σ - ϵ curves).
- Figure 29.** Stress (σ)-strain (ϵ) curves of wave structure fabricated with one pair of flat steering electrodes at the following electrospinning conditions:
 $W = 12.5$ mm; $V_1 = 11.8$ kV; $V_2 = 11.5$ kV; $x_I = 5$ mm; $x_{II} = 20$ mm;
 $a = 50$ mm; $f = 50$ min⁻¹. These conditions were applied for the fabrication of wave structure fibers within the mechanical studied if not differently stated.
Measurement in a) in AA direction, and b) in AP direction.

-
- Figure 30.** Stress (σ)-strain (ϵ) curves of square structure membranes fabricated with two pairs of flat steering electrodes at the following electrospinning conditions: $W = 6.25$ mm; $V1 = 11.8$ kV; $V2 = 11.5$ kV; $x = 15$ mm; $a = 50$ mm; $f = 50$ min⁻¹. These conditions were applied for the fabrication of square structure fibers within the mechanical studied if not differently stated.
- Figure 31.** MTS assay for CM proliferation on TCP on PLACL fibrous membranes with random structure and wave structure with one pair of steering electrodes under standard conditions, after a) 5 days, b) 10 days, and c) 15 days of cell culturing.
- Figure 32.** Morphology of CMs after 10 days of cell culturing a) TCP, b) PLACL fibers without plasma treatment, and c) PLACL fibers with plasma treatment as substrate. After 15 days of cell culturing d) TCP, e) PLACL fibers without plasma treatment, and f) PLACL fibers with plasma treated fibrous substrate.
- Figure 33.** SEM images of CMs cultured for a) 10 days on plasma treated random PLACL fibers, b) 10 days on plasma treated PLACL fibers with wave structure, c) 15 days on non-plasma treated random PLACL fibers.
- Figure 34.** Structure of polymers and dopant used in this study.
- Figure 35.** Setup for a) electrospinning, and b) electrospraying.
- Figure 36.** PEO fibers with a) 6% PANi concentration, b) 12% PANi concentration, and c) 19% PANi concentration.
- Figure 37.** I-V curves of PEO fibers with a) 6% PANi concentration, b) 12% PANi concentration, and c) 19% PANi concentration.
- Figure 38.** PANi-PEO fibers a) 6% of PANi and aluminum foil as the collector, b) 12% of PANi and aluminum foil as the collector, c) 6% of PANi collected without aluminium foil, and d) 12% of PANi collected without aluminum foil.
- Figure 39.** Grounded PVC fibers a) without DMF/THF residual and without aluminum foil, b) with DMF/THF residuals and with aluminum foil, and c) with DMF/THF residuals and without aluminum foil.
- Figure 40.** Schematic explanation on the electric field distribution between the spinneret tip and conductive PANi-PEO fibers in the presence of a) no aluminum foil beneath, and b) with aluminum foil.
- Figure 41.** SEM image of 12.5% PANi-PEO fibers coated with TiO₂ nanoparticles (5 min of deposition) followed by sonication of the membrane.

-
- Figure 42.** UV spectrum of CEPS in heptane at concentration of 0.05‰ (v/v).
- Figure 43.** UV spectra for a) 6% TiO₂-PANI-PEO membranes after 0 min and 60 min UV light exposure, and b) 12% TiO₂-PANI-PEO membranes after 0 min and 60 min UV light exposure.
- Figure 44.** Photocatalytic decomposition of CEPS with respect to reaction time and TiO₂ quantity a), after 60 min UV light exposure, and b) 10 min UV light exposure.
- Figure 45.** Proposed photocatalytic action of TiO₂ nanoparticles towards CEPS under UV environment.
- Figure 46.** Application of the cardiac patch at the heart (Chen et al., 2008b) a) epicardial, and b) endoventricular heart patches.
- Figure 47.** Helix shape of the heart muscle. Therefore, the state of stress within the heart muscle is complex and multidirectional forces are induced into the muscle (Buckberg, 2002). To demonstrate the complex helix shape of the heart muscle, it is compared with the unfolding of a rope (Torrent-Guasp et al., 2001).

List of Symbols

a	distance between two steering electrodes of one pair
CMs	cardiomyocytes
c	constant
D	distance between spinneret tip and collector
d	additional
E	electric field strength
F	force
f	higher voltage signal frequency
g	grams
h	hour
kV	kilo volts
L_p	Square fibers pattern length
l	electrode length (applicable for all additional electrodes)
l_p	period length of fibers wave pattern
mA	milliampere
min	minutes
ml	milliliter
mm	millimeter
nm	nanometer
NPs	nanoparticles
q	charge
SEM	scanning electron microscopy
t	time
UV	ultra violet
UV-VIS	ultra violet and visible

V	volts; voltage
V1	electrospinning voltage between spinneret and collector
V2	voltage applied at the steering electrodes
v %	volume percentage
W	steering electrode width
W_p	fibers pattern width
w %	weight percentage
x	position of the additional electrodes
ε	strain
ε_E	permittivity of the space between the charges
Δ	distance between the charges
ρ	phase shift of voltage signal provided by electro-mechanical controller
σ	stress

1. Introduction

1.1 Motivation and aims

In present thesis, the controllability of two electro-hydrodynamic (EHD) methods, electrospinning and electrospraying are studied.

Electrospinning is a method where a high voltage is applied to the polymer solution drop emanating from the spinneret tip. A jet is resulted from the polymer drop, when the applied voltage surpasses the surface tension, undergoes curling and spiraling, resulting in the formation of fibers which are deposited on the grounded metallic collector (Reneker and Yarin, 2008). The electrospun fibers have been used as e.g. nerve grafts, blood vessels, wound dressings, batteries, gas, bio- and chemical sensors and catalyst (Choi et al., 2003; Choi et al., 2004; Huang et al., 2003; Li et al., 2004). For electrospraying, ceramic solution driven out into the electric field disperses to nanodroplets. These nanodroplets are collected on collectors. Electrospraying is used for thin film deposition and for functional layer formation (Jaworek et al., 2009).

With a conventional electrospinning setup, the fibers are deposited randomly on the collector with a spot size exceeding 100 mm and usually cover the whole collector. Over the last years, efforts have been made to make electrospinning and electrospraying a precise and very well determined process. Most studies to improve the controllability of the fibers deposition were based on the modification of the electric field distribution by the variation of electrospinning process parameters and by setup modification.

For focused and therefore precise fibers deposition with electrospinning, circular or conical auxiliary electrodes reduce the fibers spot size to 5 mm (Bellan et al., 2006; Bellan and Craighead, 2009; Kim, 2006; Kim and Kim, 2008). Besides, the impact of a flat metal

plate above the spinneret was studied to stabilize the polymer jet with a more uniform electric field (Yang et al., 2008). With close distance electrospinning, a distance between the spinneret tip and the collector of few millimeters prevented bending instability of the polymer jet and therefore high precisions of fibers deposition were achieved (Hellmann et al., 2009).

For one directional fibers alignment, rotating drums as collector were widely used. In order to enhance the alignment effect, the setup was accomplished with different auxiliary electrodes (Wu et al., 2007) and with knife-edged bars (Teo et al., 2005). In addition, the metal plate as conventional fibers collector was replaced by sharpened electrodes (Secasanu et al., 2009) to enhance the fibers alignment. Yang et al. (2009) applied e.g. spherical collector shapes to achieve more uniform fibrous membranes thicknesses. In addition, one directional fibers alignment was achieved with two parallel collector electrodes. The fibers were stretched between the collector electrodes and therefore aligned between these (Ishii et al., 2009; Kim, 2006; Kim and Kim, 2006; Lee et al., 2007; Yan et al., 2009; Zhang et al., 2008). With one pair of positively charged secondary electrodes applied perpendicular to the primary electric field, aligned fibers with a length of 10 mm were fabricated by steering the polymer jet (Acharya et al., 2008).

An attempt for the fabrication of two dimensional fibers patterns was the collection of electrospun fibers on patterned electrodes. Collector electrodes with ring, rectangular, triangular openings allowed the patterning of fibers structures in two dimensions (Kim and Kim, 2006; Li et al., 2005; Zhang et al., 2008). Furthermore, Bellan et al.(2006) reported the controllability of electrospun fibers lines in two dimensions in a ~1 mm range with the help of a circular steering electrodes system. It consists of four electrodes elements being charged at a defined frequency resulting in a time varying electric field (Bellan and Craighead, 2009).

Theoretical and numerical methods to determine the electrospinning process and its fibers deposition have been performed (Heikkila et al., 2007; Xu, 2009).

For electrospaying, Jaworek and Krupa (1996) reported focusing with the help of guard electrodes. Due to their small size, the charged nanodroplets dispersed easily and therefore a defined deposition was challenging. Above studies and their results were further discussed in context of the results of this work.

The aim of this work was to advance the controllability of the electro-hydrodynamic (EHD) methods: electrospinning and electrospaying.

For electrospinning, the work was concentrated on two aspects:

- Precise fibers deposition by focusing the electrospinning process. Focused and precise fibers deposition is required for the breakthrough of electrospinning in mass production of high quality products. Besides, it is a prerequisite for controlled fibers deposition.
- Patterning with electrospinning. Defined linear, square and circular fibers patterns had to be achieved. One aspect was the maximization of the pattern dimensions. With defined fibers structure the mechanical properties of the fibrous membrane should be made determinable.

In this study, electrostatic lens systems were developed to achieve focused electrospinning. Steering electrodes with time varying electric field were used to control the electrospinning polymer jet.

For electrospaying, a more precise and uniform deposition of the dispersed nanodroplets was the aim. The effect of conductive nanostructured collectors was studied.

In this thesis, methods to improve the controllability of electrospinning and electrospaying were developed for applications to protect and recover human health.

With defined fibers deposition, a fibrous scaffold could be fabricated which for potential application as a cardiac patch. Electrospun fibrous scaffolds were widely used in the field of tissue engineering (Ito et al., 2005; Venugopal et al., 2008) due to the fact that fibrous scaffolds met the following requirements being important for tissue engineering:

- highly porous structure scaffold with large interconnected pores to facilitate mass transport,
- hydrophilic to enhance cell adhesion,
- structural stability to withstand the shearing forces during bioreactor cultivation,
- biodegradability, and
- non-immunogenicity.

However, for cardiac tissue engineering, the mechanical properties play a central role. Due to complex superposition of forces in the heart muscle of different states of stress like tensile stress, compression stress and torsion stress (Appendix 1) determinable mechanical properties of the scaffolds were required. Therefore, fibers orientation in the electrospun fibrous scaffold had to become more controllable. In addition, the elasticity and tensile strength of the scaffold had to meet the values of human cardiac muscle with an E-modulus of 0.2-0.5 MPa and a tensile strength of 3-15 kPa (Biomechanical background of these requirements explained and discussed in Appendix 1) (Nagueh et al., 2004; Nakano et al., 1990; Watanabe et al., 2006). However, most electrospinning approaches reported did not meet the requirement of cardiac tissue engineering in that respect. E.g. with aligned fibers deposited on rotating drums, defined fibers structures were achieved, but highly anisotropic mechanical properties, too. As the cardiac muscle and therefore the cardiac patch were exposed to multidirectional forces, such a structure was not useful for cardiac tissue engineering.

For electrospaying, the aim of this study was to enhance the precision of the electrospaying droplet deposition. In this study, electrospayed droplets were deposited on conductive nanostructured and porous material. The nanostructured and porous collector material was to cover with catalytic nanoparticles enhancing the activity due to the maximized active surface area. Highly precise nanoparticles deposition was required because the blockage of the pores with nanoparticles had to be avoided.

Controllable electrospaying was used for the fabrication of a catalytic filtration membrane. As pollution and chemical agents have become major threats to human health, there was a demand for nanostructures combining the function of filtration and catalysis (Künzli et al., 2000). The function of filtration was performed by the conductive electrospun fibrous scaffold; the catalytic activity was provided by the embedded ceramic nanoparticles. In that way both particles could be filtered and toxic gases could be degraded.

1.2 Thesis structure

In this study, methods to enhance the controllability of two electro-hydrodynamic methods (EHD) electrospinning and electrospaying were developed and investigated for applications saving human lives as well as preserving human health. After motivating the research proposed in the “Introduction” (Chap. 1), the fabrication methods electrospinning and electrospaying as well as the applied characterization methods were presented in “Experimental Techniques” (Chap. 2). In Chapt. 3, the methods developed for “Focused fibers deposition by electrospinning” (Chap. 3) were presented and the impact of focusing methods on the fibers deposition spot size, the membrane pore size and the fibers morphology were studied. Focused electrospinning and therefore determinable fibers deposition and orientation were the requirement for “Patterning with electrospinning” (Chap.

4). In that way, the fibers structure as well as the fibers morphology and therefore their mechanical properties could be influenced. The fibers structures were investigated for potential application as cardiac tissue engineering scaffold. In Chap. 5, the “Controllability of electrospaying” was studied. A method was developed, to control electrospaying at nanoscale by using conductive fibers as collector. The developed membrane was studied for application in environmental engineering like catalytic filtration applications. In Chap. 6, “Conclusions and future perspectives” controllability of electrospinning and electrospaying were compared and challenges for the future were identified (Figure 1).

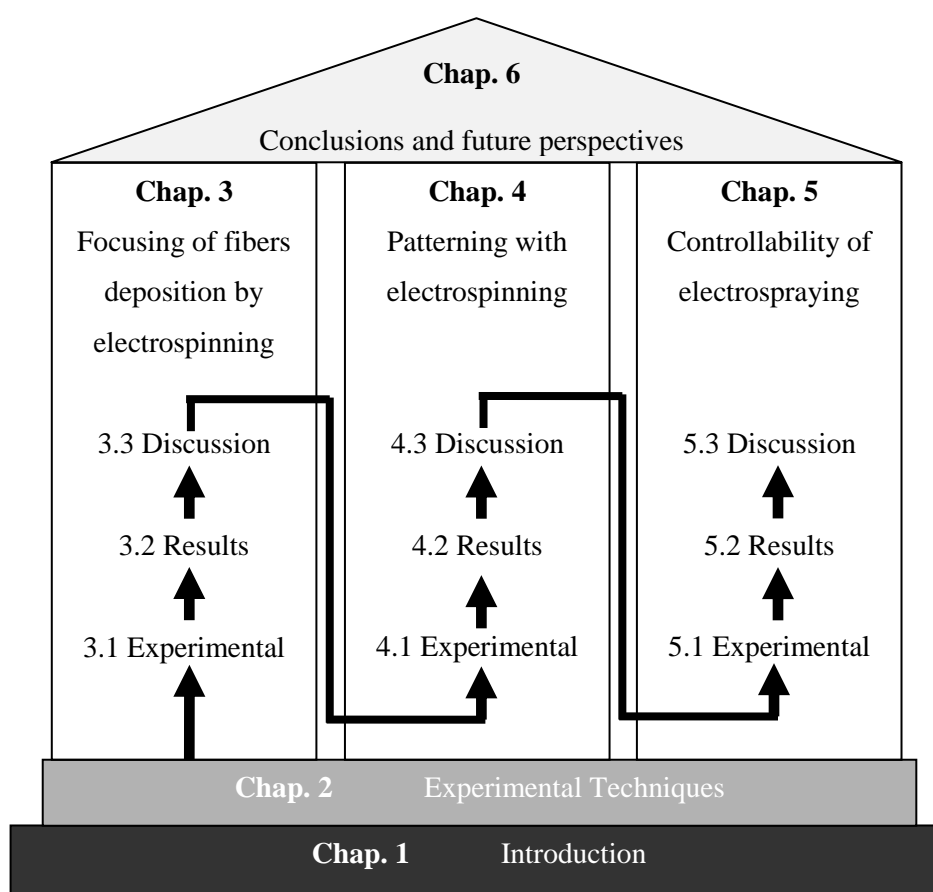


Figure 1. Structure of the thesis.

2. Experimental Techniques

In this chapter, the two fabrication techniques used for membrane fabrication in this study are introduced. Both electrospinning and electrospaying are electro-hydrodynamic methods (EHD). The setup used for both techniques is similar, however different process conditions result in different structures. In this chapter, fundamental information about the principle of electrospinning and electrospaying is presented. More detailed information about the used electrospinning and electrospaying setups within this work are described in the corresponding chapters.

2.1 Electrospinning

Electrospinning is a technique to fabricate continuous fibers with the help of an electric field (Greiner and Wendorff, 2007). The diameter of the electrospun fibers ranges between 10s of nm up to several μm . With electrospinning, polymers and ceramics can be processed to fibers (Greiner and Wendorff, 2007), whereas in this study only polymer fibers are electrospun.

Charges of different polarity result in forces of attraction. Electrospinning is based on attraction of different polarities. For point charges, the attraction force (or repulsion in case of same polarity) is given by Coulomb's Law.

$$F = \frac{q_1 q_2}{4\pi\epsilon_E \Delta^2} \quad (\text{Formula 1})$$

When the electric field is defined as a region where a charge feels a force created by other charges. Its magnitude is defined by the electric field strength E .

$$F = qE \quad (\text{Formula 2})$$

For a charge q , the field strength at a distance d is described as

$$E = \frac{q}{4\pi\epsilon_E \Delta^2} \quad (\text{Formula 3})$$

For electrospinning, the solution is usually supplied by a syringe pump system through a spinneret. After the fiber formation within the spinneret, the surface tension of the droplet is overcome, a charged jet of polymer solution is ejected by the spinneret due to the electrostatic field effect. Due to electrical conductivity of most solvents, the solution is charged positively or negatively. Therefore, the polymer jet is stretched longer and thinner, until it solidifies on the way towards the collector. Typically, a voltage 15-30 kV is applied (Ramakrishna et al., 2005). The route of the charged polymer jet is controlled by the electrostatic field. First, the jet is a stable "straight jet" (Figure 2). Second, due to repulsive forces between the charges carried with the jet, it is set into a state of bending instability and forms a cone shape (Figure 2). To enhance the precise fibers deposition with electrospinning, the state of bending instability has to be suppressed (Ramakrishna et al., 2005). The fibers are attracted on the grounded collector and a fibrous membrane is fabricated.

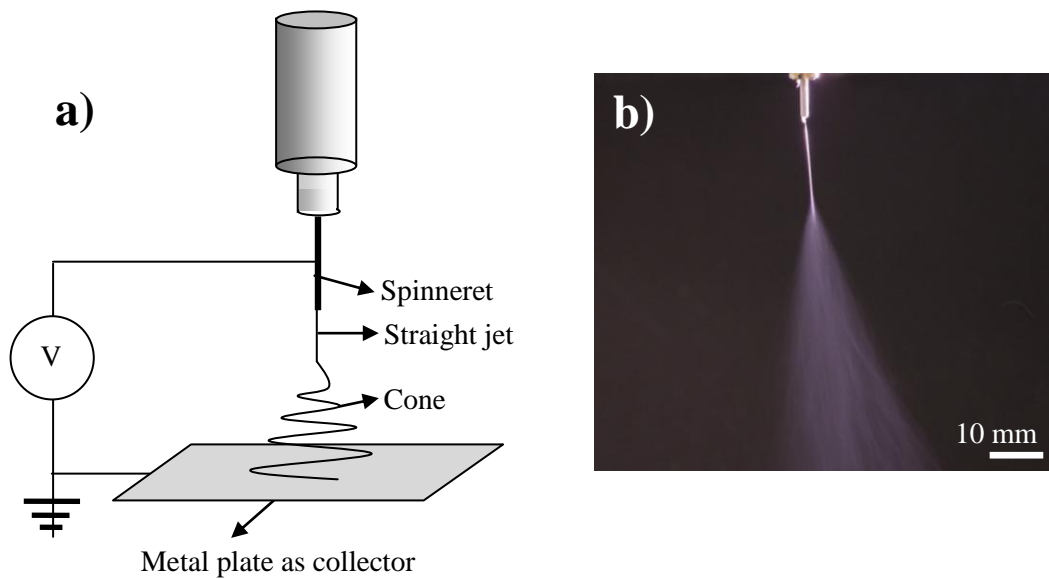


Figure 2. The polymer fiber is stretched from the spinneret tip on its way to the collector
a) Schematic drawing of standard electrospinning setup and electrospinning,
and b) photograph of polymer jet during electrospinning.

The described process and the properties of the resulting fibers structure are determined by three main aspects:

- properties of the electrospun solution
like e.g. the molecular weight and solution viscosity, the molecular weight distribution, the surface tension of the solution, the solution conductivity, the dielectric effect of solvent and the architecture of the polymer chains (branched, linear etc.) (Chronakis et al., 2005; Ramakrishna et al., 2005).
- electrospinning process conditions
like e.g. the voltage, solution flow rate, the distance between the spinneret tip and collector, the temperature, the effect of collector, the diameter of spinneret needle and the charge carried by the polymer spinning jet (Chronakis et al., 2005; Ramakrishna et al., 2005).
- ambient parameters

like e.g. humidity, type of atmosphere and pressure (Ramakrishna et al., 2005).

These process parameters determine the morphology of the fibrous membranes like the fiber diameter, the pore size and porosity and other relevant membrane properties like elasticity, tensile strength etc. The electrospinning parameters have to be optimized to achieve fibers with the properties required for their determined application. The impact of two important electrospinning parameters, the impact of the distance between the spinneret tip and the collector D and the solution viscosity on the resulting fibers structure are discussed.

With increasing viscosity of the solution, the surface tension of the solution is reduced and therefore the fiber defects like beads, broken fibers etc. are avoided.

The distance between the spinneret tip and the collector D directly influences the flight time and the strength of the electric field. By reducing D , the flight time of the polymer jet is reduced because it has a shorter distance to travel and the electric field is strengthened resulting in higher acceleration of the polymer. In order to avoid melted fibers, a minimum distance has to be maintained to allow the solvents to evaporate from the electrospinning polymer. Besides, the stretching time results in higher fiber diameter.

All electrospinning parameters mentioned influence the strength and the distribution of the electrostatic field. To achieve more controlled fibers deposition, modifying the electric field either permanently or temporarily were reported to be useful to achieve controlled fibers deposition electrospinning. Reported approaches have been reviewed in Chapter 1.1.

2.2 Electrospaying

Electrospaying is a method similar to electrospinning. E.g. the same setup and the applied process parameters used for both of these methods are very similar (Figure 3). The main

difference is the property and composition of the processed solution. In contrary to electrospinning, electro spraying aims at breaking up the processed solutions in droplets smaller than 1 μm . For electro spraying, solutions with high surface tension and high viscosity are required. These solution properties are achieved with low material concentration or low molecular weight of the dissolved material. As a result, the solution breaks up into droplets when exposed to the electric field. The droplets dispersed homogeneously in the electric field are attracted to the collector due to their positive charge (Jaworek, 2007).

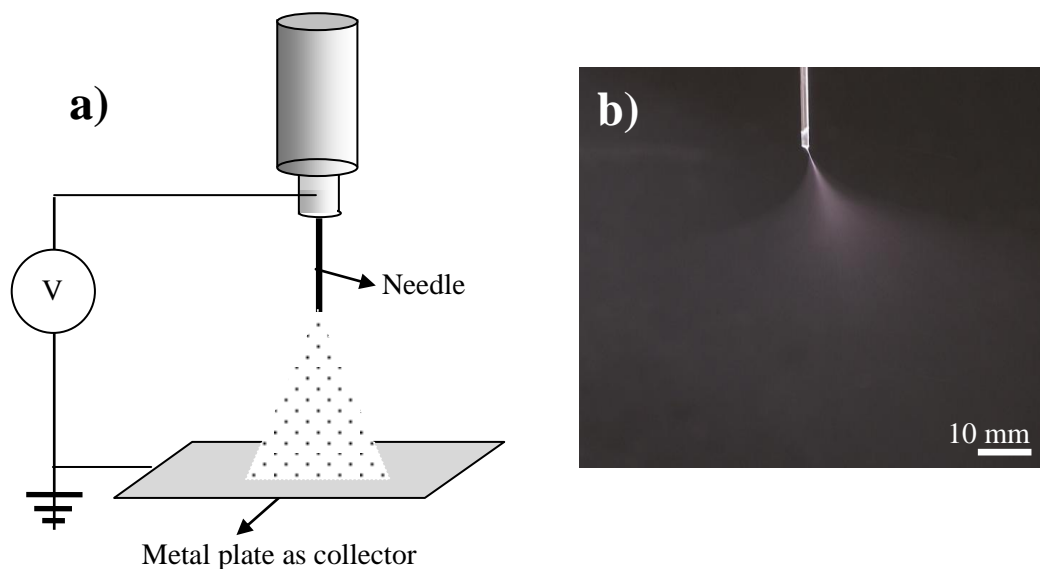


Figure 3. For electro spraying, the solution breaks up into droplets directly at the needle tip and are dispersed.

- a) Schematic drawing of standard electro spraying setup, and
- b) photography of droplet dispersion during electro spraying.

The size of the droplets and therefore uniformity of the coating is determined by the applied electro spraying mode varying in number, shape and size of the released droplets (Figure 4).

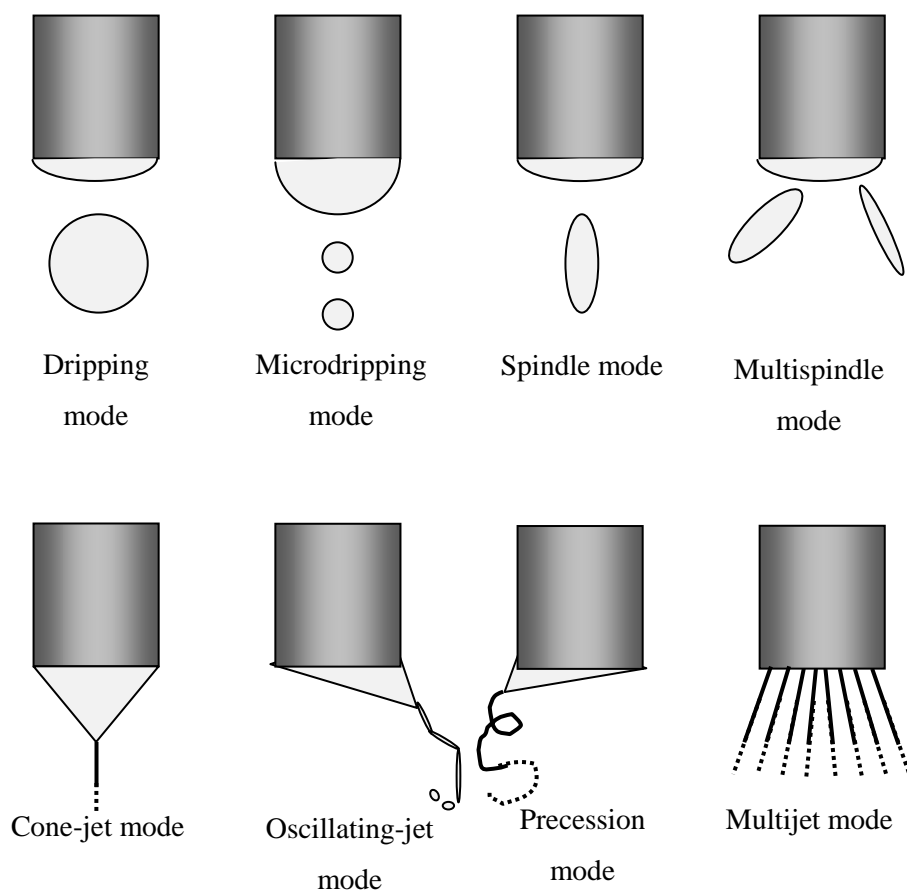


Figure 4. Modes of electrospaying (Jaworek and Sobczyk, 2008).

In this study, exclusively the multi-jet mode was strived because small droplet size was necessary (Jaworek and Sobczyk, 2008). Pliszka et al. (2008) have investigated the multi-jet mode of electrospaying and have determined the droplet size achieved with electrospaying at the needle tip with a Particle Image Velocimetry (PIV) system. They showed that microdroplets with a size down to 10 μm could be achieved with electrospaying of TiO_2 nanoparticles (25 nm size nanoparticles size) at the needle tip. The average microdroplet size measured at different electrospaying voltages was $\sim 20 \mu\text{m}$. Due

to further dispersion of the droplets on their way to the collector, droplets with a size at nanometer range were observed.

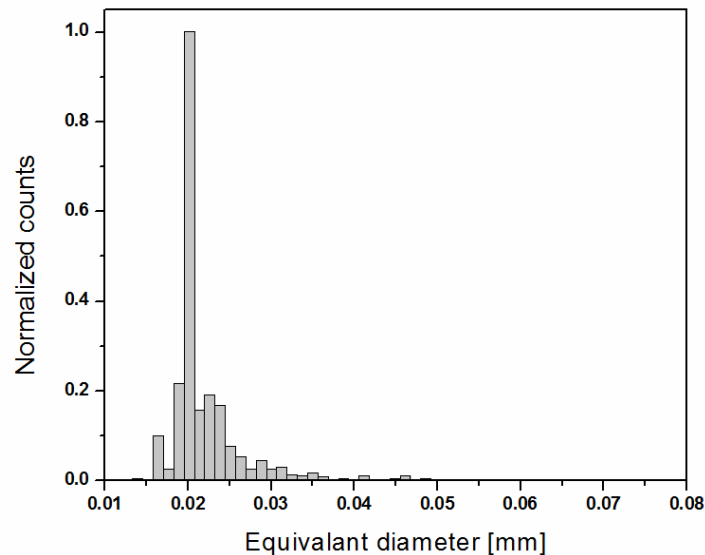


Figure 5. The droplet size distribution of droplets close to the needle tip for electro spraying of solution of 5% (w/v) TiO_2 nanoparticles concentration and an electro spraying voltage of 6 kV (Pliszka et al. (2008)).

Electro spraying has some advantages in comparison with conventional mechanical spraying systems with droplets charged by induction (Jaworek, 2007):

- Droplets are smaller than those available from conventional methods like for instance mechanical spraying atomizers, and can be smaller than $1 \mu\text{m}$.
- The size distribution of the droplets is usually narrow, with low standard deviation, however only for dripping and microdripping modes droplets can be of equal size.
- Charged droplets are self-dispersing in the space. Hence, there are no droplet agglomeration and coagulation.
- The motion of charged droplets can be easily controlled (introducing deflection or a piezoelectric focusing) by electric fields.

- The deposition efficiency of charged spray on an object is much higher than for uncharged droplets.

2.3 Characterization

The stability of electrospinning in combination additional electrodes (steering electrodes) was investigated with a Dantec Dynamic Camera System (Denmark).

In order to evaluate the fibers morphology, the fibrous membranes were coated with gold by sputtering (JEOL JFC-1600, Auto Fine Coater, Japan) and examined by scanning electron microscope (SEM) QUANTA 200F from FEI (Netherlands) at an accelerating voltage of 10 kV. The diameters of the electrospun fibers were analyzed from the SEM images using image analysis software (Image J, National Institutes of Health, USA).

The pore size distribution was determined from bubble point measurements on the basis of wet up/dry up method using a capillary flow porometer (Porous Materials Inc, USA) by complete wetting of the membranes with Galwick (Porous Materials Inc, USA) (Porter, 1990).

The hydrophilic nature of the electrospun fibrous membranes was investigated based on sessile drop water contact angle measurement using VCA Optima Surface Analysis system (AST products, Billerica, MA). Droplets of distilled water were dripped onto the fibrous membranes. The contact angle indicated their hydrophilicity.

Tensile properties of fibrous membrane were determined at 20°C with an Instron 5845 Microtester (USA). A cross-head speed of 10 mm/min and a load of 10 N were applied. Force (F)-strain (ϵ) curves were recorded. In combination with the geometric dimensions (width, thickness and length of the samples) of the fibers samples, stress (σ) - strain (ϵ) curves were derived (Formula 4).

$$\sigma = \frac{F}{w * q} \quad (\text{Formula 4})$$

The E-modulus was determined on the slope of the first linear part of the stress (σ)-strain (ϵ) curve (Formula 5).

$$E = \frac{\Delta\sigma}{\Delta\epsilon} \quad (\text{Formula 5})$$

To determine the tensile strength of fibrous membranes, the maximum values of tensile stress was used.

For I-V measurements, the fibrous membrane was deposited on silica, which has gold electrodes at both ends (Figure 5). The conductive nature of fibrous membranes was studied by I-V measurement using potentiostat (Autolab PGSTAT30, The Netherlands).

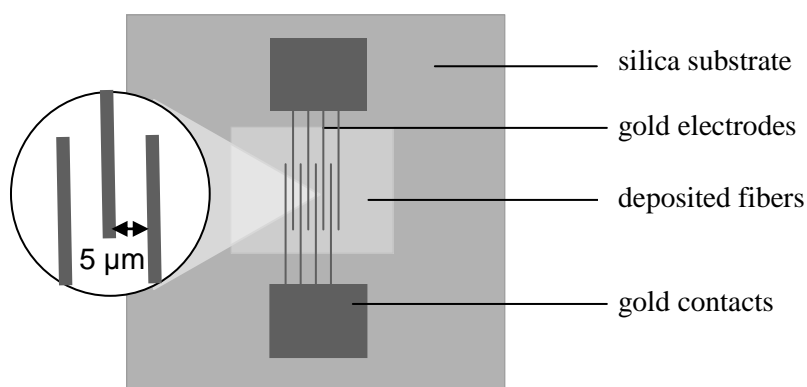


Figure 5. Gold electrode with a 5 μm distance on silica substrate.

The photocatalytic activity of membranes was estimated adding a defined quantity to a solution containing the substance to be degraded. Then the samples were exposed to UV light for 10 min and 60 min and the absorbance decay at characteristic peaks of substance to be degraded photocatalytically.

The binding stability of nanoparticles onto fibrous membranes was tested by sonicating the solution at 30% intensity level for 1 h in diethyl ether medium using ultrasonic liquid processor (VCX 500 Sonic).

3. Focused fibers deposition by electrospinning

In the first subchapter of this thesis, defined fibers deposition with electrospinning was achieved by focusing of electrospinning. The focusing effect was tested for various polymers and solvents in order to achieve a general result. As precise fibers deposition has relevance for tissue engineering and filter applications, the effect was studied for biocompatible and non-biocompatible polymers.

3.1 Experimental details

3.1.1 Materials

For this study, the polymers Nylon-6 (UBE, Japan), polycaprolactone (PCL) (M_w 80 000 Da; Sigma-Aldrich, USA), poly(L-lactic acid)-copoly-(3-caprolactone) (PLACL) (70:30, M_w 150 000 Da; Boehringer Ingelheim Pharma GmbH & Co., Germany) and poly(vinyl chloride) (PVC) (M_w 233 000 Da; Sigma-Aldrich, USA) were electrospun.

Therefore, they were dissolved in chloroform (purity \geq 99.8 %; Merck, Germany), methanol (purity \geq 99.8%; Sigma-Aldrich, Germany), N,N-dimethylformamide (DMF) (ACS reagent, \geq 99.8%; Sigma-Aldrich, Germany), tetrahydrofuran (THF) (purity \geq 99.0%; Merck, Germany), dichloromethane (DCM) (purity \geq 99.8%; Merck, Germany) and 1,1,1,3,3,3-hexafluor-2-propanol (HFP) (purity \geq 99%; Sigma-Aldrich, Germany) without any further purification.

3.1.2 Membrane fabrication

Nylon solution A and B: Nylon was dissolved in HFP at a concentration of 10% (w/v) and 26% (w/v) respectively.

PCL solution: PCL at 10% (w/v) concentration was dissolved in methanol and chloroform with a ratio 5:8 (v:v). After 24 h of stirring, the solution was electrospun by using a modified electrospinning setup.

PLACL solution A and B: PLACL was dissolved in HFP at a concentration of 10% (w/v) and 26% (w/v) respectively.

PVC solution A: PVC was dissolved at a concentration of 10% (w/v) in DMF and THF used in equal amounts.

PVC composition B: 0.3 g of PVC was added to DMF, THF and DCM used in equal amounts (1 ml) and stirred for 2 h at 35°C. After another 24 h of stirring at 20°C, 1.5 ml of THF was added. This solution was stirred for another 24 h.

These solutions were electrospun with GAMMA High Voltage Research (USA) and Glassman High Voltage, Inc. (USA) power supplies. V1 denoted the voltage applied between the spinneret and the collector, V2 the voltage between the electrostatic lens system and the collector.

The electrode position was defined by the coordinate axis x in vertical direction with the spinneret tip as zero point ($x = 0$). The electrode position was defined from their bottom edge. The diameter was defined as geometric dimensions for all components of the electric lens system. The length was only a relevant parameter for the tube electrode. The distance between the spinneret tip and the collector was defined as D . All dimensions were given in mm (Figure 6).

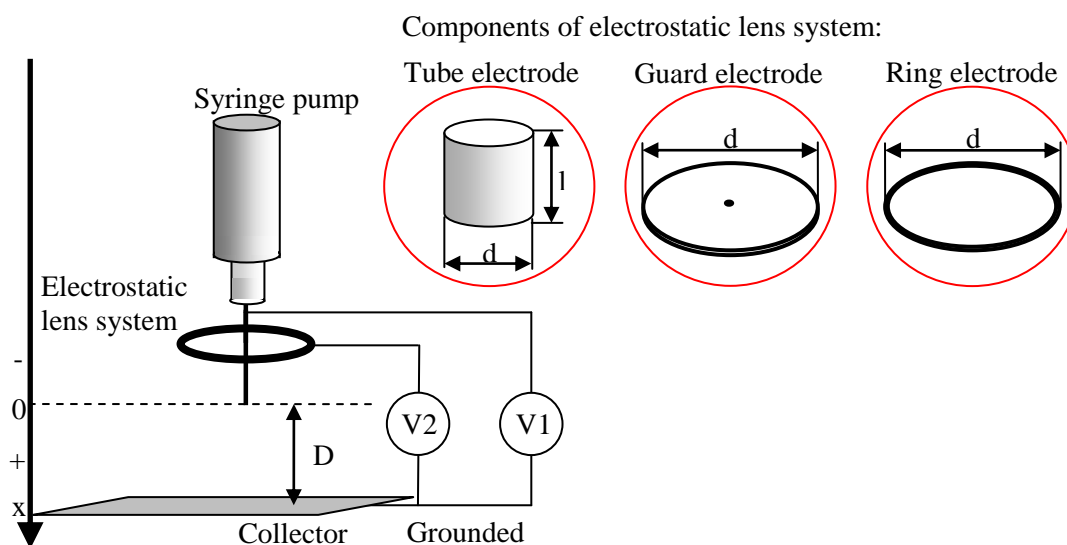


Figure 6. Setup for electrospinning of polymer fibers with electrostatic lens system.

The following electrospinning parameters were defined by the setup:

- D distance between the spinneret tip and the collector,
- $V1$ voltage between the spinneret tip and the collector,
- $V2$ voltage between the electrostatic lens system and the collector,
- x position of the components of the electrostatic lens system,
- d diameter of the components of the electrostatic lens system, and
- l length of the components of the electrostatic lens system.

3.2 Results

After the fibers formation and polymer jet having left the spinneret, the electrospinning polymer jet is a "straight jet". Due to its electrical charging, the polymer jet is set into a state of bending instability and forms a cone shape. At the collector the fibers are deposited. In this study, increasing the length of the "straight jet" and limiting bending instability as well as a stabilization of the cone axis contributed to smaller fibers spot sizes

achieved by electrostatic lens systems, collector size modification and adaption of distance between the spinneret and the collector D.

3.2.1 Electrostatic lens systems

Different combinations of the electrostatic lens system consisting of tube electrodes, ring electrodes and guard electrodes were implemented in order to modify the electrostatic field.

3.2.1.1 Single ring electrode

An electrostatic lens system consisting of one ring with $d = 33$ mm was added to the electrospinning setup (Figure 1) for Nylon, PCL, PLACL and PVC fibers fabrication with the electrospinning conditions as in Table 1.

The same voltage was applied between the spinneret and the collector as well as the electrostatic lens system and the collector. D was maintained at 120 mm.

Table 1. Impact of ring electrode position with $d = 33$ mm on the fibers spot size and fibers diameter.

Polymer solution	Electrode position x [mm]	Voltage V1 and V2 [kV]	Flow rate [ml/h]	Spot size [mm]	Fibers diameter [nm]
Nylon A	-	14	1.0	not defined	357 ± 62
	-15	14	1.0	59.6 ± 3.5	495 ± 88
	0	21	1.0	33.5 ± 1.9	1141 ± 293
PCL	-	19	0.7	not defined	368 ± 120
	-15	19	0.7	69.2 ± 4.4	379 ± 40
	-10	19	0.7	59.8 ± 3.6	406 ± 67
	-5	25	0.5	41.4 ± 2.7	420 ± 126
	0	26	0.5	31.6 ± 1.9	523 ± 154
PLACL A	-	14	1.0	not defined	602 ± 106
	-15	14	1.0	59.6 ± 3.4	631 ± 135
	0	21	1.0	31.3 ± 2.1	1351 ± 174
PVC A	-	10	1.0	not defined	607 ± 127
	-15	10	1.0	69.5 ± 2.1	632 ± 96
	0	17	1.0	32.5 ± 1.2	765 ± 153

Without any additional electrodes, drying polymer solution could cause a partly blockage of the spinneret tip resulting in deflection of the electrospinning cone. The deflection of the electrospinning cone was eliminated. Second, the length of the straight jet was elongated due

to the electrostatic field modified by the ring electrode. The result was a smaller electrospinning cone and therefore a smaller fibers spot size (see Table 1).

Without any additional electrode, electrospinning was not locally defined and therefore the whole collector was covered with fibers. With the help of a ring electrode ($x = -15$ mm), a defined spot size with a diameter 60 - 70 mm was achieved for all electrospun polymers. Shifting the ring electrode towards the spinneret tip, the spot size could be decreased to a defined size of ~30 mm diameter. Simultaneously, the voltage was increased by 7 kV in order to maintain stable electrospinning. The spot size slightly varied due to different molecular weight and properties of the electrospun polymers and due to the different solution properties. Electrospinning of PCL solution was studied with the additional ring electrode at different position between $x = -15$ mm and $x = 0$ mm. A correlation between the position of the additional ring electrode and the fibers spot size was found (Table 1).

The experimentally achieved results were compared with numerical modeling. The electrostatic field was investigated by SIMION Version 8.0 (Scientific Instrument Services, INC., USA) on the basis of equipotential line simulations and its impact on the behavior of the polymer jet was predicted.

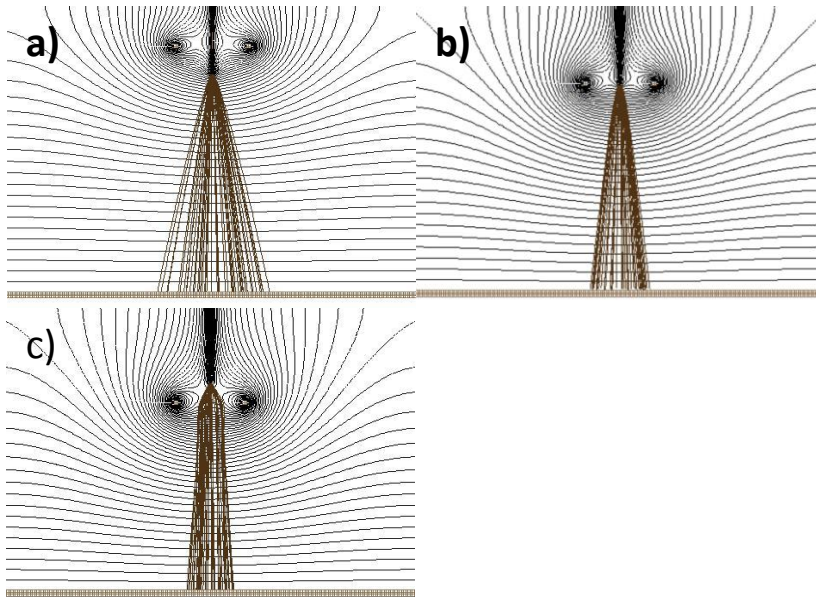


Figure 7. Equipotential lines in the spinneret - focusing ring - collector system:
a) ring at $x = -15$ mm, b) ring at $x = 0$ mm, and c) ring at $x = 10$ mm with voltage 25 kV.

The numerical modeling is in good qualitative agreement with the experimental results because the fibers spot size was halved by shifting the ring electrode from $x = -15$ mm to $x = 0$ mm (Figure 7a and Figure 7b). As indicated by modeling, positioning the ring electrode under the spinneret tip showed an even more significant decrease of the fibers spot diameter (Figure 7c). In the experiment positioning one ring electrode underneath the spinneret tip resulted in a highly unstable electrospinning due to the electrostatic field weakened by a charged ring electrode below the spinneret tip.

The ring electrode position also had an impact on the average fibers diameter (Table 1). With enhanced focusing effect, bending instability of the polymer jet was reduced and therefore the way the polymer jet was stretched was reduced. The degree of this effect varied depending on the polymer and the polymer solution property. Not only was the average diameter increased by shifting the metal ring towards the needle tip, but the fibers diameter uniformity also increased. Consequently, the diameter homogeneity of the fibers was

affected by positioning the additional ring electrode close to the spinneret tip and by the enhanced focusing effect.

For all investigated polymers, the pore size of the membrane (size of the space between the fibers being an important scaffold characteristic for tissue engineering and filtration) was reduced by applying an additional ring electrode ($x = -15$ mm). The trend of reducing the pore size was continued by shifting the additional ring electrode toward the spinneret tip ($x = 0$ mm) and by increasing the voltage by 7 kV (Figure 8). The development of the pore size could be correlated to the fibers spot size. With focused fibers deposition and therefore a high density of fibers, the pore size decreased and could therefore be influenced by the application and position of additional electrodes. Besides, the tendency observed for the pore size diameter could be partly explained by fibers diameters. One explanation for the quantitative pore size differences comparing the fibrous membranes consisting of different polymer were the different fibers diameters (Figure 8).

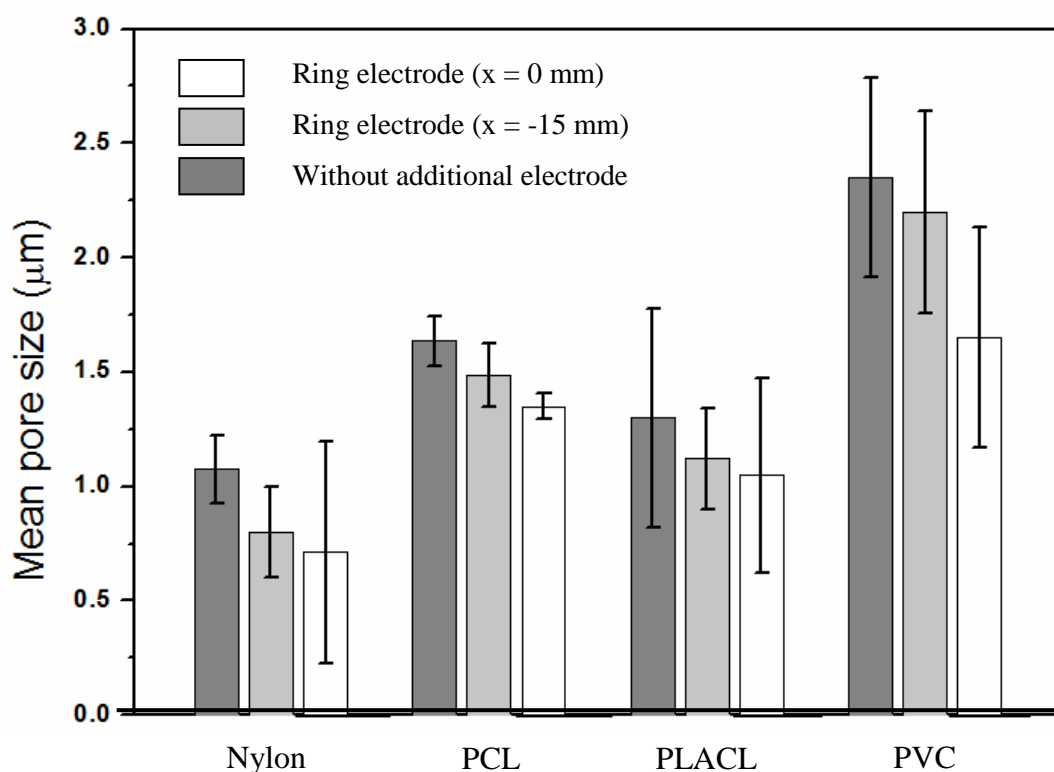


Figure 8. Pore sizes without any additional electrode, with additional ring electrode ($x = -15$ mm) and with additional ring electrode ($x = 0$ mm) for Nylon, PCL, PLACL, and PVC.

As the behavior of electrospinning of all studied polymers was similar, PVC solution A was chosen for further optimization.

3.2.1.2 Guard electrode

A guard electrode was a metal disc fixed co-axially at the spinneret. Modeling indicated a more homogeneous electrostatic field with the guard electrodes. The stabilizing effect of guard electrodes was reported for electrospraying (Jaworek et Krupa, 1996). With a guard electrode, the electrospinning cone axis was more stable, the electrospinning cone angle was narrower due to a more homogeneous electrostatic field distribution, the length of

the straight jet in the electrospinning process was increased and the system could be operated in a wider voltage range.

Table 2. Impact of varying position of the guard electrode on the spot size and the fiber quality. PVC solution A was electrospun with a flow rate 1.0 ml/h.

Electrode diam. d [mm]	Position x [mm]	Voltage V1 and V2 [kV]	Spot size [mm]
50	-15	10	36.4 ± 1.6
50	-5	10	23.9 ± 0.9
20	-5	10	31.4 ± 2.0

Guard electrodes of various diameters were applied at different positions (Table 2). Large guard electrodes with $d = 100$ mm suppressed the electrospinning process at any position. The electrostatic field between the needle tip and the collector was too weak to release any fiber. For a smaller guard electrode with $d = 50$ mm and positioned at $x = -15$ mm electrospinning was not interrupted and the fibers spot diameter was 30 mm. The fibers spot diameter could be decreased further to 25 mm by positioning the guard electrode closer to the spinneret tip at $x = -5$ mm. Due to the weakened electrostatic field between the spinneret tip and the collector, stretching the jet could not be maintained and therefore electrospinning was interrupted. This effect did not occur for a guard electrodes with $d = 20$ mm. Fibers were produced at any guard electrode position, however the fibers spot diameter was comparatively large with 35 mm at the minimum. Therefore, there was a compromise between the focusing effect of guard electrodes and the weakening of the electrostatic field between the spinneret tip and the collector resulting in unstable fiber formation.

The quality of the fibers produced in the system with guard electrodes was not significantly affected by the variation of the guard electrode position.

3.2.1.3 Combinations of ring and tube electrodes

Several combinations of the electrostatic lens system were studied. In setup 1 and 2, investigating the impact of the tube diameter, a reduction of the tube electrode diameter from $d = 11$ mm to $d = 3$ mm decreased the fibers spot diameter for $\sim 17\%$ and therefore enhanced the focusing effect (see Table 3).

Table 3. Correlation between the elements of the electrostatic lens system, their combination, the applied voltages V1 and V2 and the fibers spot diameter. For all configurations, PVC solution A, a flow rate 1.0 ml/h and $D = 100$ mm were applied.

Setup	Electrode	Diameter d [mm]	Length l [mm]	Position x [mm]	Voltage V1 [kV]	Voltage V2 [kV]	Spot size [mm]
1	Tube	3	20	-1	12.0	12.0	34.7 ± 1.6
2	Tube	11	20	-1	12.0	12.0	42.8 ± 2.5
3	Tube Ring	11 20	20 -	-1 8	11.0	7.0	20.9 ± 1.6
4	Ring 1 Ring 2	25 30	- -	-1 16	10.0	7.8	13.4 ± 1.8

Tube electrodes with smaller diameter increased the average fiber diameter. The average fiber diameter was 660 ± 298 nm for a tube electrode with $d = 3$ mm and $l = 20$ mm and positioned at $x = -1$ mm. Fibers spun with a tube electrode with $d = 11$ mm and the other

parameters remaining the same had a diameter of 521 ± 211 nm. Fibers spun with a small tube diameter showed significant diameter variation, but did not show any other defects.

In order to improve the controllability of the electrostatic field and therefore the electrospinning process, a different voltage was applied at the components of the electrostatic lens system.

Based on the achieved modeling results (Figure 7), a hypothesis was derived that an electrostatic lens system positioned below the spinneret tip could enhance the focusing effect. Using one electrode at this position resulted in the interruption of electrospinning. Positioning components of the electrostatic lens system below the spinneret tip in combination with maintained electrospinning were achieved by combining two electrodes and decreasing the voltage applied to the electrostatic lens system. Therefore, one electrode was positioned above the spinneret tip, the other one below. A voltage of 1-2 kV lower than for the voltage between the spinneret tip and the collector was applied to the electrostatic lens system in order to avoid the interruption of electrospinning. The effectiveness of electrostatic lens setup 3 and 4 considering focusing was investigated (see Table III). Setup 4 with two ring electrodes was found to reduce the fibers spot diameter more efficiently than the tube-ring combination (Setup 1-3). By setting ring electrode 1 at $x = 16$ mm, the length of the straight jet was increased and could therefore pass through ring electrode 2 positioned under the spinneret tip ($x = -1$ mm). The voltage applied at the electrostatic lens system 8.4 kV had to be set incrementally increased in order to maintain electrospinning. Applying the 2-ring electrodes combination, the fibers spot diameter was reduced by over 40 % in comparison with tube-ring electrode combination to 12 mm (Table 3). However, the fiber quality was unsatisfactory for the 2-ring electrodes combination because of fused fibers due to the insufficient solvent evaporation. Insufficient solvent evaporation was explained by the

smaller electrospinning cone size and therefore the shorter way the fiber took from the spinneret tip to the collector. Furthermore, the average fiber diameter was larger than 1 μm .

3.2.1.4 Geometry of the electrospinning setup

By reducing the collector size and replacing the aluminum square collector with an edge length of 150 mm by a aluminum stripes with 16 mm and 6 mm width as well as by a 0.1 mm copper wire, the fibers spots had the shape of an ellipsis with a minor axis of 10 mm at the minimum and an undefined major axis size. With decreasing collector size, a weakened electrostatic field between the spinneret tip and the collector was observed. Due to the weak electrostatic field between the spinneret tip and the collector, no combination of a small collector and electrostatic lens systems could be achieved. Therefore, the focus was shifted from studying the impact of reduced collector size to the effect of a smaller D.

According to the geometry intercept theorem, the fibers spot size could be reduced with decreasing distance D if the cone angle ϕ was maintained constant. The correlation between D and the fibers spot diameter hypothesis was confirmed by numerical modeling.

Halving D from 100 mm to 50 mm and applying a tube electrode as the electrostatic lens system (Table 4), the fibers spot diameter was decreased by 25 % from 30 mm to 22 mm for optimized electrospinning conditions. However, for smaller D, the average fiber diameter increased from 511 ± 211 nm (for D = 100 mm) to 547 ± 177 nm (D = 50 mm) and the fiber deposition showed less uniformity. These negative effects of smaller D were explained with the shorter way to stretch the fibers in the electrostatic field.

Table 4. Impact of the distance D between the spinneret tip and the collector on the fibers spot size. For all configurations, PVC composition A and a flow rate 1.0 ml/h were applied.

D [mm]	Electrode	Diameter d [mm]	Length l [mm]	Position x [mm]	Voltage V1 [kV]	Voltage V2 [kV]	Spot size [mm]
100	Tube	11	20	-1	12.0	12.0	42.8 ± 2.5
50	Tube	11	20	-1	12.0	12.0	25.5 ± 1.4
116	Ring 1	25	-	-1	10.0	7.7	13.4 ± 1.8
	Ring 2	30		16			
66	Ring 1	25	-	-1	10.0	7.7	4.55 ± 0.38
	Ring 2	30		16			

The application of an electrostatic lens system consisting of two ring electrodes resulted in a stronger focusing effect (Table 4). The fibers spot diameter was reduced from 12 mm to 6 mm with D = 116 mm and D = 66 mm respectively. Due to the reduced travel distance of the fibers between the spinneret tip and the collector, the fibers were fused together after their deposition on the collector. In addition, the fiber diameter increased significantly with decreasing D. In order to facilitate solvent evaporation from the electrospun fibers, a hot air draft was introduced into the setup perpendicular to the collector and at a 45° angle. With hot air, the solvent could evaporate comparatively fast. However, spindles and beads degraded the fiber quality. Besides, the hot air increased the fibers spot diameter due to the turbulences. Therefore, the application of the hot air was not taken consideration to enhance solvent evaporation.

3.2.2 Optimized setup

Since one of the two most effective methods to reduce the fibers spot size was the reduction of D , the fibers fusion had to be prevented. Two approaches were studied: First, the amount of solvent had to be reduced and therefore the polymer concentration increased. Second, solvents were substituted by solvents with lower vapor pressure and therefore faster evaporation.

For PVC, the electrospinning setup accomplished with an electrostatic lens system was optimized consisting of a guard electrode with $d = 50$ mm positioned at $x = -10$ mm combined with two ring electrodes with the dimension $d = 25$ mm positioned at $x = 1$ mm and $d = 30$ mm positioned at $x = 17$ mm. Distance between the spinneret tip and the collector was $D = 70$ mm and the flow rate of the electrospinning solutions was 1 ml/h (Figure 4).

PVC solution B with faster evaporating solvents was applied. The solvents DMF and THF were partly substituted by solvent with higher vapor pressure. Therefore, besides DCM, DMF and THF were used as solvent for PVC composition B due to its high vapor pressure of 46700 Pa in comparison with a vapor pressure of 347 and 17200 Pa for DMF and THF respectively. Because of the very viscous solution, and a electrospinning spot size of 3.74 ± 0.37 mm (Figure 4B, Table V) and thin fibers with a diameter 193 ± 40 nm (Figure 9c, Table 5) were fabricated.

With the electrospinning setup optimized for PVC, Nylon and PLACL fibers were tested. Therefore, the polymer solutions were adapted by increasing the polymer concentration to 26 % (w/v) (Nylon solution B and PLACL solution B). The spot size was reduced to 3-4 mm diameter, however due to the high polymer concentration and therefore high solution viscosity, the fibers diameter exceeded 1000 nm in both cases (Figure 9).

Table 5. Nylon, PLACL and PVC fibers were electrospun with $D = 70$ mm and a flow rate 1.0 ml/h. Components of the electrostatic lens system: guard electrode with $d = 50$ mm positioned at $x = -10$ mm, ring electrode 1 with $d = 25$ mm positioned at $x = 1$ mm and ring electrode 2 with $d = 30$ mm and positioned at $x = 17$ mm.

Polymer solution	Voltage V1 [kV]	Voltage V2 [kV]	Spot size [mm]	Fiber diameter [nm]
Nylon B	14.0	9.5	3.65 ± 0.58	1201 ± 250
PLACL B	14.0	9.5	3.71 ± 0.47	1790 ± 422
PVC B	12.8	10.2	3.74 ± 0.37	193 ± 40

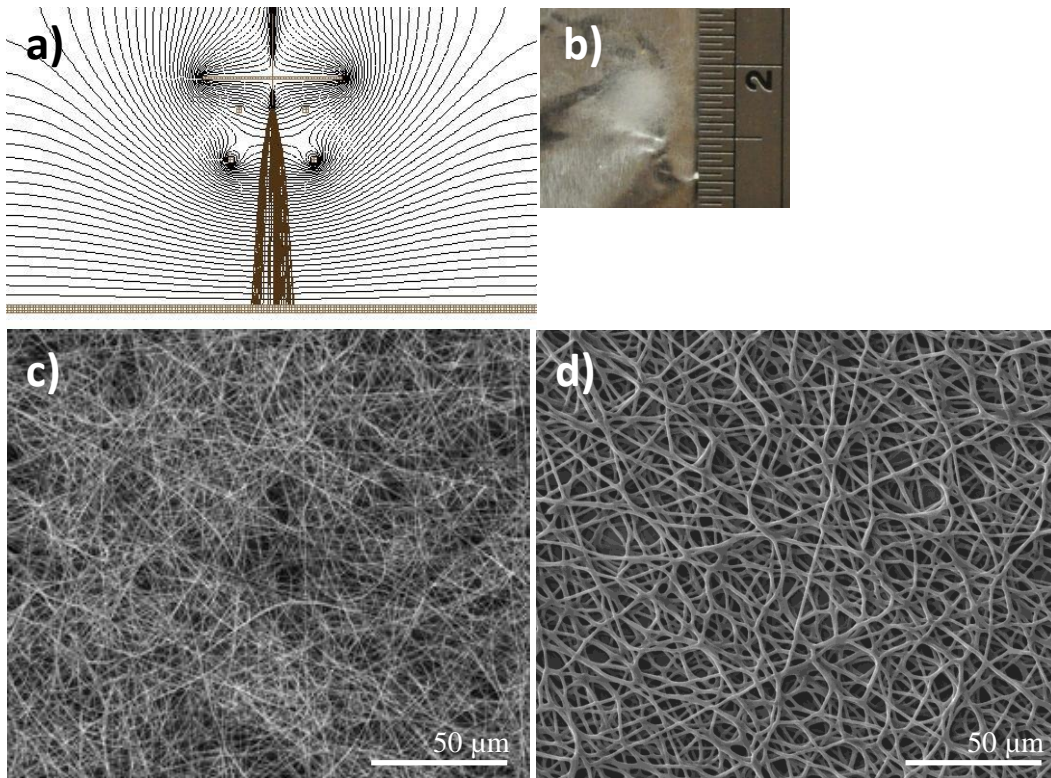


Figure 9. Fibers electrospun under optimized conditions (Table 5) with flow rate 1.0 ml/h and $D = 70$ mm on a static collector. Components of the electrostatic lens system: guard electrode with $d = 50$ mm positioned at $x = -10$ mm, ring electrode 1 with $d = 25$ mm positioned at $x = 1$ mm and ring electrode 2 with $d = 30$ mm and positioned at $x = 17$ mm a) modeling, b) fibers spot size (PVC solution B), c) morphology of PVC solution B, and d) morphology of Nylon fibers.

For the PCL solution, high quality fibers with a strong focusing effect as with the other polymers could not be achieved in combination with the solvents chloroform and methanol. Therefore, this study demonstrated that the presented methods for precise fibers deposition were applicable for a wide variety of polymers, but also had some limitation considering the choice of solvent and polymer.

A long deposition time of the fibers on a single spot caused a creation of solid button-like structure due to high solvent concentration and redissolving of the fibers. With a

collector moving with a speed of ~ 0.1 m/s, fibers lines with a width of 0.158 ± 0.013 mm were electrospun. Because of the stretching of the polymer due to the collector movement, the fibers diameters were reduced to 833.1 ± 115.6 nm and 1177.8 ± 122.7 nm for Nylon and PLACL respectively. These lines were a promising tool for the precise deposition of fibers and the fabrication of fine structures (Figure 10).

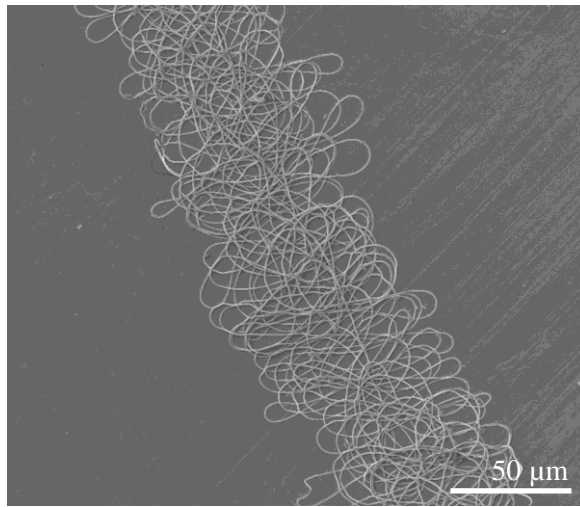


Figure 10. PLACL fibers electrospun under optimized conditions (Table V) with a flow rate 1.0 ml/h and $D = 70$ mm on a collector moving with ~ 0.1 m/s. Components of the electrostatic lens system: guard electrode with $d = 50$ mm positioned at $x = -10$ mm, ring electrode 1 with $d = 25$ mm positioned at $x = 1$ mm and ring electrode 2 with $d = 30$ mm and positioned at $x = 17$ mm. The fibers line had a width of 0.158 ± 0.013 mm.

3.3 Discussion

Control over the pore size of electrospun fibrous membranes has high relevance for both tissue engineering scaffolds and filter membranes (Thavasi et al., 2008). However, achieving the required pore size is a challenge for conventional electrospinning. Electrostatic

lens systems were found to be good methods to control the pore size. The correlations were proven for a variety of polymers.

Besides the pore size, electrostatic lens systems were shown to be useful to control electrospinning, which has fibers spot diameters exceeding 100 μm with undefined boundaries with conventional electrospinning setup. During the last years, efforts have been done to focus electrospinning in order to establish this method for mass production. Kim et al. (Kim et al., 2007) applied cylindrical auxiliary electrodes above the spinneret to achieve a stable electrospinning of polycaprolactone (PCL) microfibers. The obtained microfiber spot diameter was 22 μm . By introducing positively charged series of ring electrodes between the spinneret tip and the collector, Deitzel et al. (2001) electrospun polyethylene oxide (PEO) ~300 nm diameter fibers with water based solution and achieved a fibers spot diameter of 10 μm . Bellan et al. (Bellan et al., 2006) achieved a fibers spot diameter of 5 μm for PCL dissolved in water. To focus electrospinning, a complex four electrode device was positioned between the spinneret tip and collector.

In contrary to these studies, we used solutions based on organic solvents and could therefore achieve results applicable for a wider range of polymers. In addition, we could reduce the electrospinning spot diameter to 3-4 μm for the polymers Nylon, PLACL and PVC in combination with good fibers morphology.

Defined fibers deposition was essential for the next part of this thesis aiming at the fabrication of defined fibers patterns in order to enhance the control over the mechanical properties of a fibrous membrane.

4 Patterning with electrospinning

In the previous subchapter, the emphasis was set on focusing electrospinning and therefore on minimizing the area of fibers deposition. A small and defined area of fibers deposition was the requirement for controlled fibers deposition. Controllability of electrospinning was achieved by introducing steering electrodes charged positively at a defined frequency. In the first step, the electrospinning polymer jet was controlled in one direction and therefore one dimensional fibers orientation was achieved. In the second step, control was gained over the electrospinning polymer jet in two dimensions and therefore two dimensional fibers patterns like square or circular fibers patterns were fabricated.

For this part of the study, PLACL was chosen as the polymer for electrospinning due to its good biocompatibility and its biodegradability with a degradation time of 6 - 12 months (Ananta et al., 2009; Prabhakaran et al., 2009).

4.1 Experimental details

4.1.1 Materials

The electrospun polymer poly(L-lactic acid)-copoly-(3-caprolactone) (70:30, M_w 150 000 Da) (PLACL) was purchased from Boehringer Ingelheim Pharma GmbH & Co., Germany. The solvent 1,1,1,3,3,3-hexafluor-2-propanol (HFP) was used as purchased without any purification.

For biocompatibility tests, cardiomyocytes (CMs) were obtained from rabbit heart tissue. Dulbecco's modified eagle's medium (DMEM), fetal bovine serum (FBS), antibiotics and trypsin-EDTA were purchased from GIBCO Invitrogen (Carlsbad, CA, USA). For final

washing, ethanol (Fisher Scientific, UK) and hexamethyldisilazane (HMDS) (Sigma-Altrich, USA) were used.

4.1.2 Membrane fabrication

PLACL was dissolved in HFP at 26 % (w/v), stirred for 24 h and electrospun at a flow rate of 0.2 ml/h by using the electrospinning setup accomplished by one steering electrode pair (Figure 11) as well as by two electrodes pairs (Figure 12). The distance between the spinneret tip and the collector D was set at 50 mm in order to minimize the instability of the electrospinning polymer jet and therefore enhance the precision of the fibers deposition (compare with Chap. 3.2.1.4). The effect was enhanced with a guard electrode ($d = 20$ mm) positioned ~ 6 mm above the spinneret tip. An electrospinning voltage V_1 of 11.8 kV was chosen. To achieve a voltage signal as shown in Figure 14, an electro-mechanical controller as described in Figure 13 was used. The steering electrodes were charged by the electro-mechanical controller with a voltage signal f (Figure 13).

With the voltage signal provided by the electro-mechanical controller, the electrodes were positively charged like the electrospinning polymer jet (Figure 11 and Figure 12). Due to the switchable charging of the steering electrodes, the electrospinning polymer jet was set into a state of controllable oscillation. On this principle, control was gained over the movement of the polymer electrospinning jet and therefore local control was gained over the fibers deposition. The steering electrodes were contacted with the grounded collector over a resistance $R_{\text{tot}} = 4 R$.

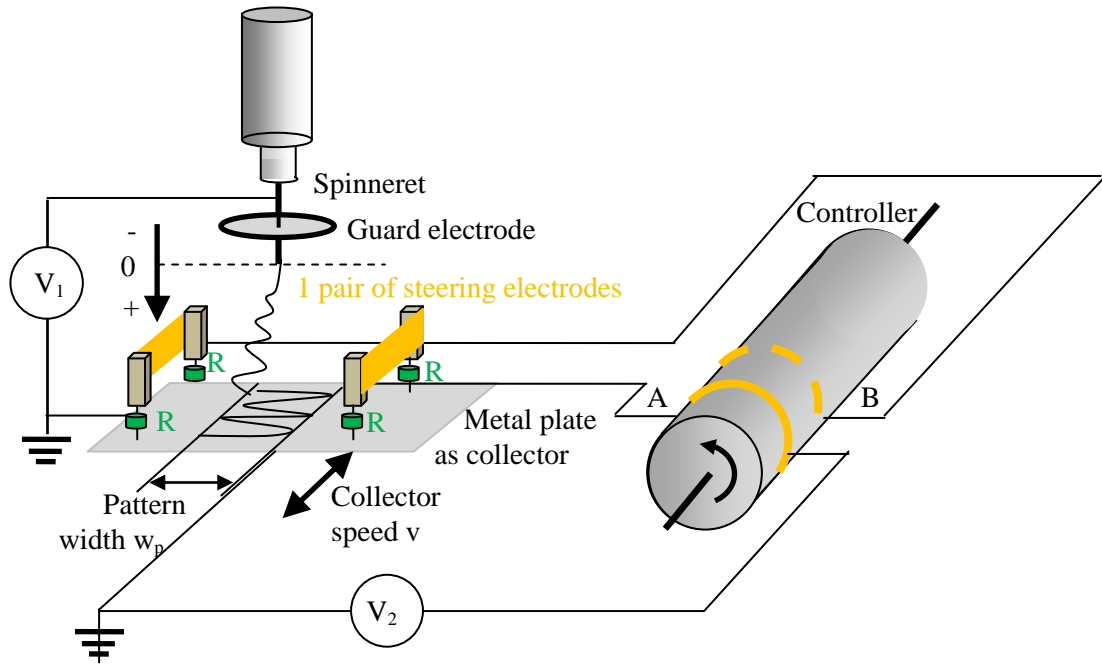


Figure 11. Setup with one steering electrode pair. The distance between one pair of steering electrodes was denoted as a . The collector moved in line with the steering electrodes with a speed v .

The dimensions of the steering electrodes were defined by the electrode length l for flat steering electrodes and by the diameter d for circular steering electrode. Together with the width W , the position x , the applied voltage V_2 and the distance between the steering electrodes a , the parameters for the electrospinning process were defined in one set of parameters. When two steering electrodes positioned parallel and therefore acting in the same direction were applied, their position was defined with x_I and x_{II} .

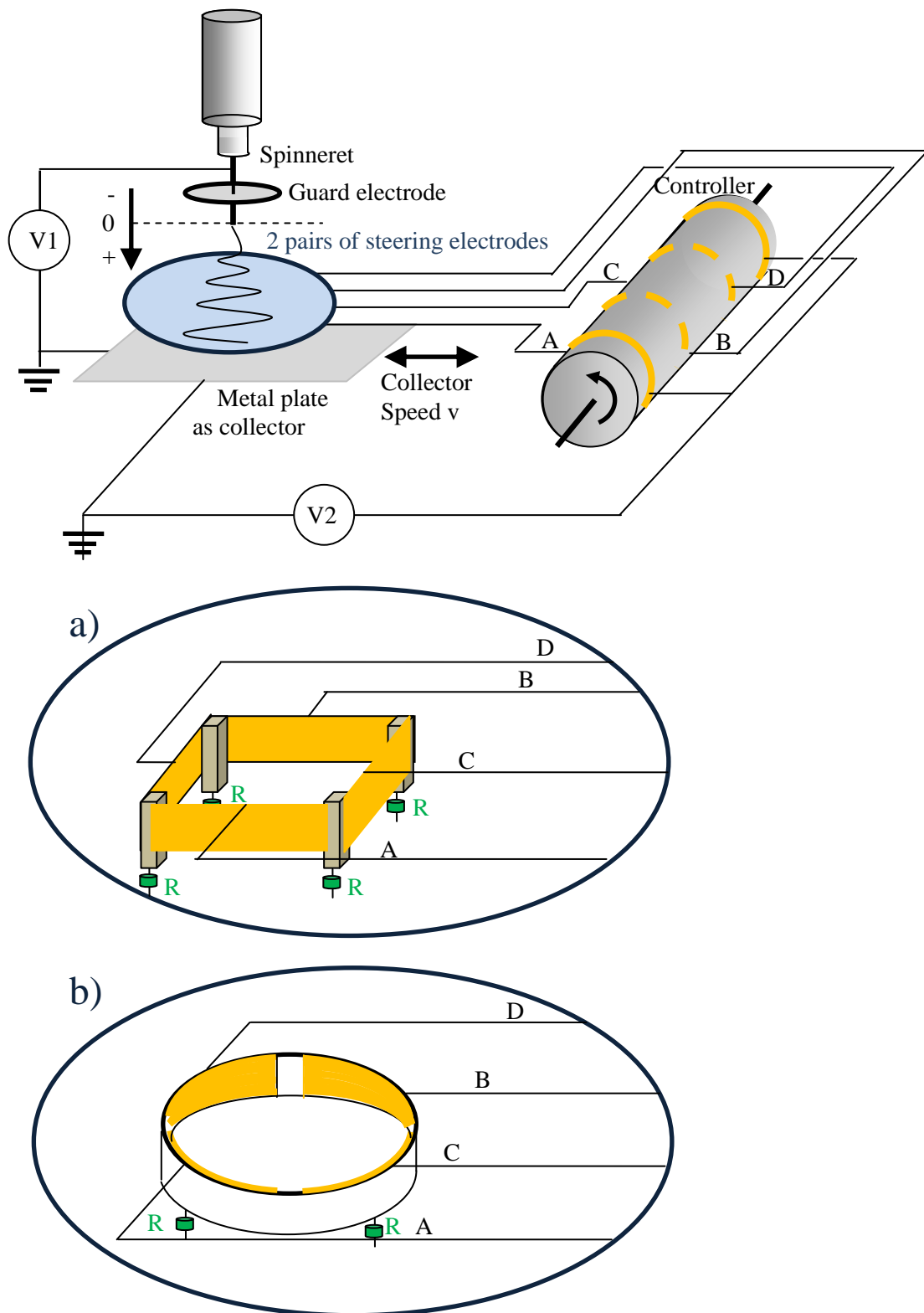


Figure 12. Setup with two steering electrode pairs using
a) flat electrodes design, and b) circular electrodes design.

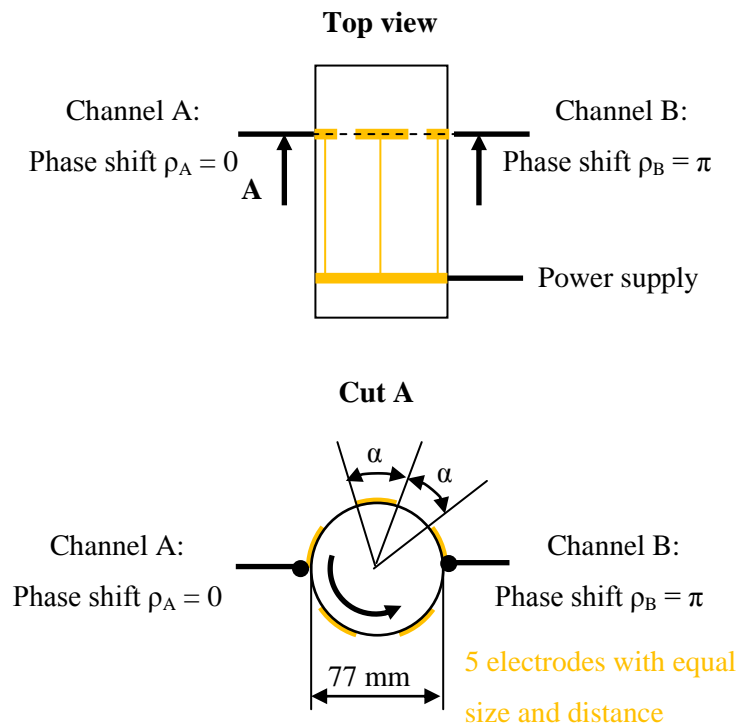


Figure 13. Principle of the electro-mechanical controller

Five metal electrodes with equal size and equal gaps ($\alpha = 36^\circ$) were attached on the rotating drum with a diameter of 77 mm. The gaps were covered with insulating material. The electrodes were charged by a second metal stripe besides, which covered the whole circumference of the drum.

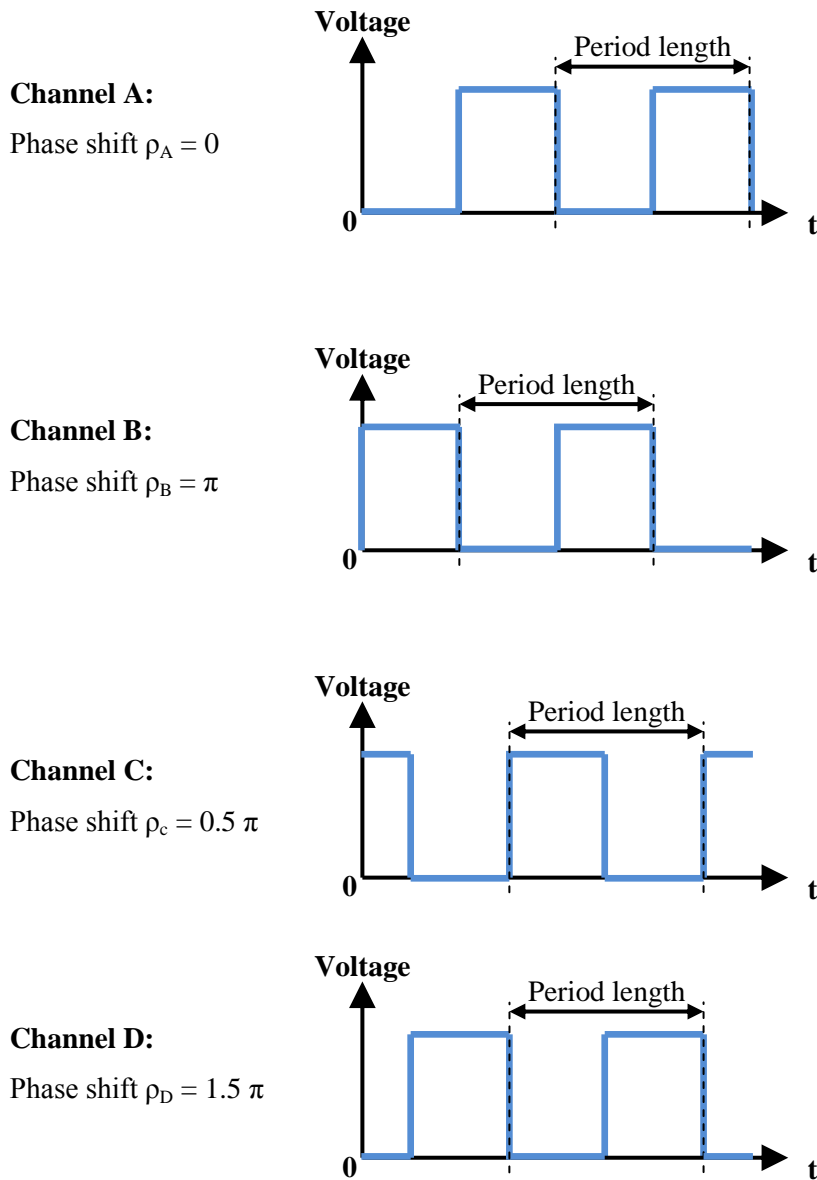


Figure 14. Voltage signal provided by the electro-mechanical controller. At all four channels A, B, C and D, the same voltage signal was provided shifted by 0.5π , π and 1.5π to the reference voltage signal (Channel A).

The effect of the following parameters to control electrospinning was studied:

- steering electrodes position x ,
- distance between one pair of flat electrodes a (Figure 11),
- steering electrodes width W ,
- voltage applied on the steering electrodes V_2 ,
- length of the electrodes in case of two steering electrode pairs positioned perpendicular to each other (Figure 12a), and
- diameter of two steering electrode pairs with circular design (Figure 12b).

For the whole study, the speed of the collector movement was maintained at 0.008 m/s. Due to the design of the drive mechanism, the collector stopped after a movement of 80 mm for ~0.5 s.

For comparison, aligned PLACL fibers were electrospun and deposited on a rotating drum as a grounded collector. The drum with a diameter of 200 mm was operated at 30 U/s. Therefore, the fibers were deposited on a surface moving at a rotational speed of 0.32 m/s.

For plasma treatment, the fibrous membranes were plasma treated for 1 min at high intensity with a Plasma Cleaner/ Sterilizer (Harrick, USA).

4.1.3 Biocompatibility test

Electrospun fibers (PLACL) were collected on 15 mm glass coverslips and placed in 24 well plates and pressed with stainless steel rings to ensure complete contact with the fibrous scaffold. Before cell culture, the samples were sterilized under UV light (3 h), washed with phosphate buffer saline (PBS), and immersed in DMEM overnight before cell seeding on fibers.

Cardiomyocytes (CMs) obtained from rabbit heart tissue was cultured in DMEM high glucose with 10% FBS and 1% antibiotics and antimycotic solutions (Invitrogen Corp, USA). CMs were grown in 75 cm² cell culture flasks and detached by adding 1 ml of 0.25% trypsin containing 0.1% EDTA. The detached cells were centrifuged and counted by trypan blue assay using a hemocytometer. CMs were seeded at a density of 1x10⁴ cells/well on fibrous scaffold and left in the incubator at 37°C to enhance cell growth. Cells were incubated at 37°C for 15 days maximum in a humidified atmosphere containing 5% CO₂. The culture medium was changed every 3 days. As reference, CMs were grown on tissue culture polystyrene (TCP) and the cell growth was compared with that on fibrous scaffold.

The cell adhesion and proliferation on the fibrous scaffolds were analyzed on the basis of colorimetric MTS assay (CellTiter⁹⁶ Aqueous One Solution, Promega, Madison, WI, USA). Dehydrogenase enzymes secreted by mitochondria of metabolically active cells reduced the yellow tetrazolium salt in MTS (3-(4,5-dimethylthiazol-2-yl)-5-(3-carboxymethoxyphenyl)-2-(4-sulfophenyl)-2H-tetrazolium) to form purple formazan crystals. The amount of formed formazan crystals is directly proportional to the number of cells was assayed at 492 nm, MTS was used as a method to quantify the cell growth on fibrous membrane. For MTS assay, the samples were rinsed with PBS to remove the dead cells and incubated with 20% MTS reagent at 37°C for 3 hrs. The obtained dye was measured spectrophotometric plate reader (FLUO-star OPTIMA, BMG lab Technologies, Germany). Cell proliferation was determined by MTS assay after 5, 10 and 15 days of cell culturing.

CMs seeded on PLACL fibers with a random and controlled fibers structure as well as on control TCP were stained with fluorescent 5-chloromethylfluorescein diacetate (CMFDA cell tracker green, Promega) for fluorescent microscopy observation of their phenotype after 10 and 15 days. Cells were incubated with 5 μM of CMFDA for 60 min at 37°C in the CO₂

incubator. The dye was removed after incubation, washed with PBS and supplemented with respective culture media. This mixture was incubated at 37°C for an additional 24 h period then washed with PBS, mounted in mounting media and observed by confocal laser scanning microscope at a fluorescent light wavelength of 490 nm.

The morphology study of the *in vitro* cultured CMs on both random PLACL and PLACL fibers deposited controlled by steering electrodes and having a buckling structure. After 10 and 15 days of cell culturing, the scaffolds were investigated by SEM. The scaffolds were rinsed twice with PBS and fixed in 3% glutaraldehyde for 3 h. Subsequently, the scaffold was rinsed in DI water then dehydrated with upgrading concentrations of ethanol (50%, 70%, 90%, 100%) twice for 15 min each. Finally the samples were washed with 100% ethanol and dried in hexamethyldisilazane (HMDS) overnight.

4.2 Results

4.2.1 Impact of setup design on pattern structure

The steering electrodes were integrated with the electrospinning setup in two different designs:

Design 1: The steering electrodes were completely isolated from the grounded collector with $R_{\text{tot}} \rightarrow \infty$.

Design 2: The steering electrodes were shortened with the grounded collector over a resistance $R_{\text{tot}} = 150 \text{ M}\Omega - 300 \text{ M}\Omega$ with a permanent current flow of 0.04 mA - 0.08 mA.

For Design 1 applied with a single electrode pair ($W = 12.5 \text{ mm}$; $V_1 = 11.8 \text{ kV}$; $V_2 = 11.5 \text{ kV}$; $x_I = 5 \text{ mm}$; $x_{II} = 20 \text{ mm}$; $a = 50 \text{ mm}$), a pattern width of $9.3 \pm 0.5 \text{ mm}$ was achieved. Moreover, a focusing effect on electrospinning was observed especially for the application of two steering electrode pairs in flat and circular design. Only a static fibers spots with 5 mm diameter was achieved, but no controlled movement of the electrospinning cone and therefore a defined fibers deposition with Design 1. Therefore, Design 1 was not taken into consideration anymore.

For Design 2 applied with a single electrode pair ($W = 12.5 \text{ mm}$; $V_1 = 11.8 \text{ kV}$; $V_2 = 11.5 \text{ kV}$; $x_I = 5 \text{ mm}$; $x_{II} = 20 \text{ mm}$; $a = 50 \text{ mm}$), a significantly bigger pattern of $33.6 \pm 4.0 \text{ mm}$ was achieved. However, for currents exceeding 0.08 mA and therefore for R_{tot} smaller than 150 M Ω , a decreasing pattern size was observed.

Therefore, the controlled discharging current from the steering electrodes over a resistance $R_{\text{tot}} = 150 \text{ M}\Omega - 300 \text{ M}\Omega$ to the grounded collector was identified as essential to

enhance the pattern width. This observation was confirmed for patterns fabricated by two steering electrode pairs.

In order to explain this phenomenon observed experimentally, two different explanations were hypothesized:

- 1) The electric field at a voltage $V_2 = 11.5$ kV was too strong. Therefore, the partly discharging of the steering electrodes and therefore the weakening of the electric field was essential. However, this explanation could not be confirmed because smaller voltages applied to the electrodes resulted in smaller pattern width W_p for Design 1 and 2.
- 2) The current flow between the steering electrodes and therefore the discharging effect between the steering electrodes and the collector was essential due to the design of the electro-mechanical controller.

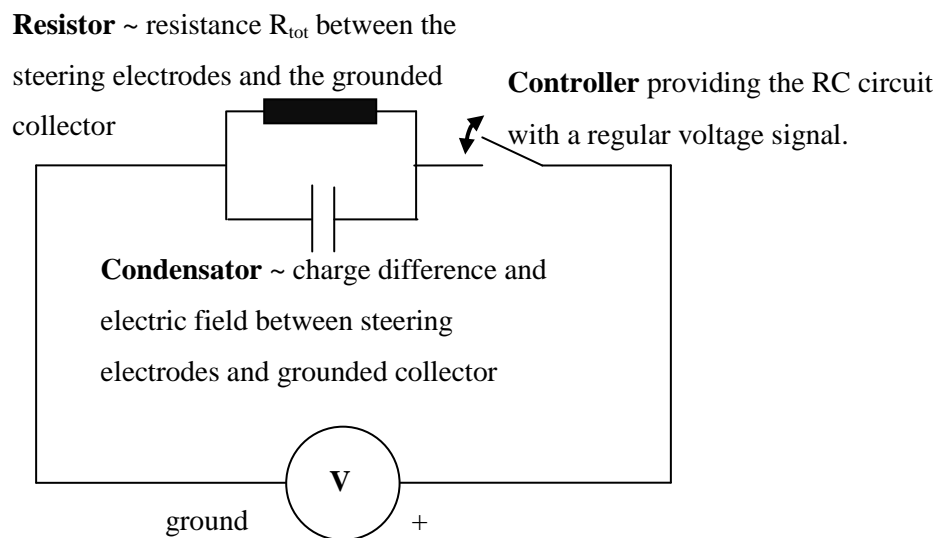


Figure 15. Electronic principle of the steering electrodes. The controller (Figure 13) provided the RC-circuit consisting of a condensator and resistor with a defined voltage signal. The condensator and the resistor represent the electric field and the resistance R_{tot} between one steering electrode and the grounded collector respectively.

With $R \rightarrow \infty$, the condenser representing the electric field between the steering electrode and the grounded collector was hardly discharged due to the high frequency of the voltage signal exceeding 250 min^{-1} and the lacking discharging mechanism (Figure 16). Both electrodes of the electrode pair were permanently positively charged and therefore repelled the positively charged polymer jet. As a result, the polymer jet was focused and the pattern width was affected.

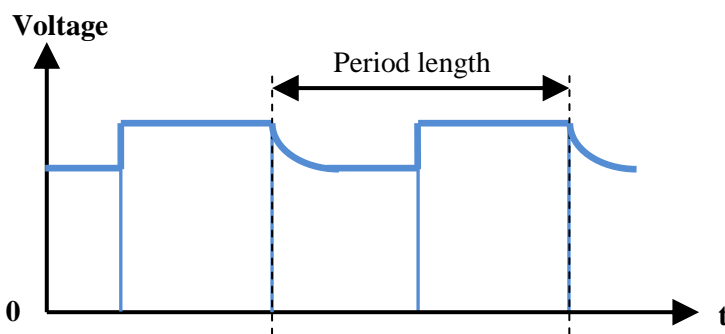


Figure 16. Design 1: For $R_{\text{tot}} \rightarrow \infty$, the expected voltage signal remains with the steering electrodes remaining charged (qualitative estimation).

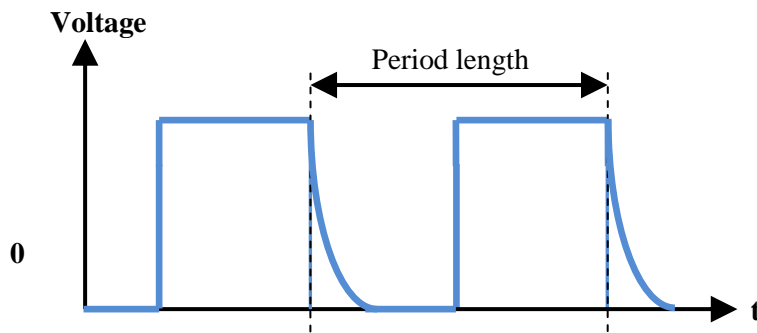


Figure 17. Design 2: For $R_{\text{tot}} = 150 \text{ M}\Omega - 300 \text{ M}\Omega$, the expected voltage signal provided by the mechanical controller (qualitative estimation).

By introducing resistances with $R_{\text{tot}} = 150 \text{ M}\Omega - 300 \text{ M}\Omega$ between the steering electrodes and the collector, the electrodes were discharged as soon as the charge supply was interrupted by the electro-mechanical controller (Figure 17). With R_{tot} smaller than $150 \text{ M}\Omega$ and discharge currents exceeding 0.08 mA , the strength of the electric field, the repulsion

force on the polymer jet and therefore the pattern width W_p were affected. With $R_{tot} = 150 \text{ M}\Omega - 300 \text{ M}\Omega$, a compromise between a sufficient discharging effect and maintaining the strength of the electric field of the steering electrodes was found.

As explanation 2 met the experimental observation in all points, it was used as the basis for further discussions. Besides, Design 2 was chosen for all coming electrode designs.

In order to assure the quality of the fibers for electrospinning in combination with switchable steering electrodes, the stability of the polymer jet was optically analyzed with a high speed camera (Figure 18). It was shown that the stability of electrospinning was not by the steering electrodes under the optimized conditions. Since no droplets and no multi-jet electrospinning occurred, evidence for a very stable electrospinning was given.

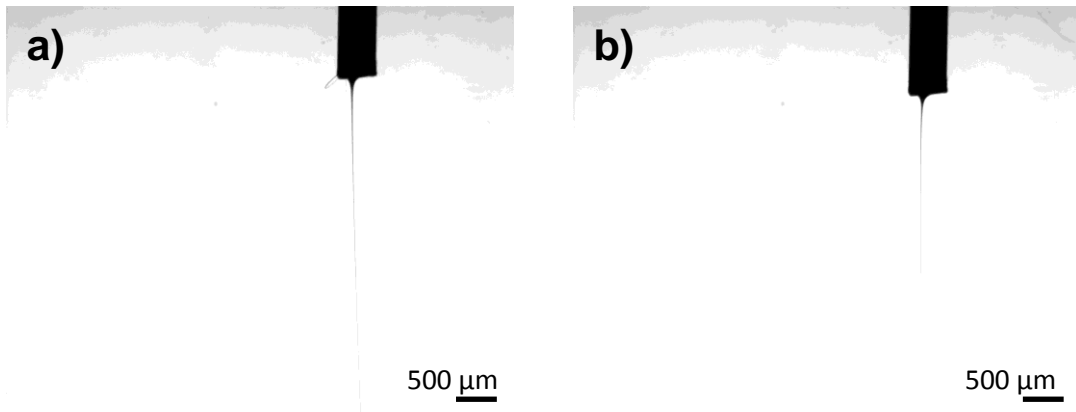


Figure 18. Single jet PLACL fiber extracted from the spinneret tip a) without steering electrodes ($V_1 = 11.8 \text{ kV}$), and b) with one pair of flat steering electrodes ($V_1 = 11.8 \text{ kV}$; $V_2 = 11.5 \text{ kV}$; $W = 12.5 \text{ mm}$; $x_I = 5 \text{ mm}$ $x_{II} = 20 \text{ mm}$; $a = 50 \text{ mm}$).

In order to maximize the pattern size, the focus was firstly set on controlling electrospinning with one pair of flat steering electrodes in one direction. To identify the main process parameters, five parameters were varied experimentally and the impact of the

experimentally studied parameters was partly confirmed by modeling with SIMION Version 8.0 (Scientific Instrument Services, INC., USA), a software usually used for ion beam trajectories modeling, which has also been found useful for electrospinning. Simulation results were equipotential lines of the electric field and charged particles trajectories, which could be taken as an electrospun fibers approximation:

1. Steering electrodes position

Increasing the distance between the spinneret tip and the electrodes x resulted in larger pattern sizes. An increase of x from 0 mm to 20 mm resulted in an increasing pattern width W_p by about a factor of two. However, increasing x and therefore shifting the steering electrodes towards the collector was limited by shorting occurring between the positively charged steering electrode ($V_2 = 11.5$ kV) and the grounded collector for distances smaller than 17.5 mm.

2. Steering electrodes width W

With increasing steering electrode width W , the length of the polymer jet being exposed to electric field effect forces was larger. Therefore, wider steering electrodes were more effective to control electrospinning and to achieve large fibers patterns. But with the steering electrodes width W exceeding 25 mm (other electrospinning parameters: $V_1 = 11.8$ kV; $V_2 = 11.5$ kV; $a = 50$ mm; $x = 10$ mm), fibers were deposited on the steering electrodes or electrospinning was completely suppressed due to the strong additional electric field.

3. Distance between flat steering electrodes a

With decreasing distance between the steering electrodes, the electric field was strengthened (Formula 2). Therefore the deflection of the polymer jet and the pattern width W_p was enhanced. For a distance between the steering electrodes $a = 100$ mm, W_p did not exceed 5 mm, whereas W_p increased to over 20 mm for $a = 50$ mm. But with steering electrodes distance a being smaller than 50 mm (other electrospinning parameters set as in the modeling part), either fibers were collected on the steering electrodes or electrospinning was completely suppressed due to the strong additional electric field. The impact of the distance between the steering electrodes was confirmed by modeling (Figure 19).

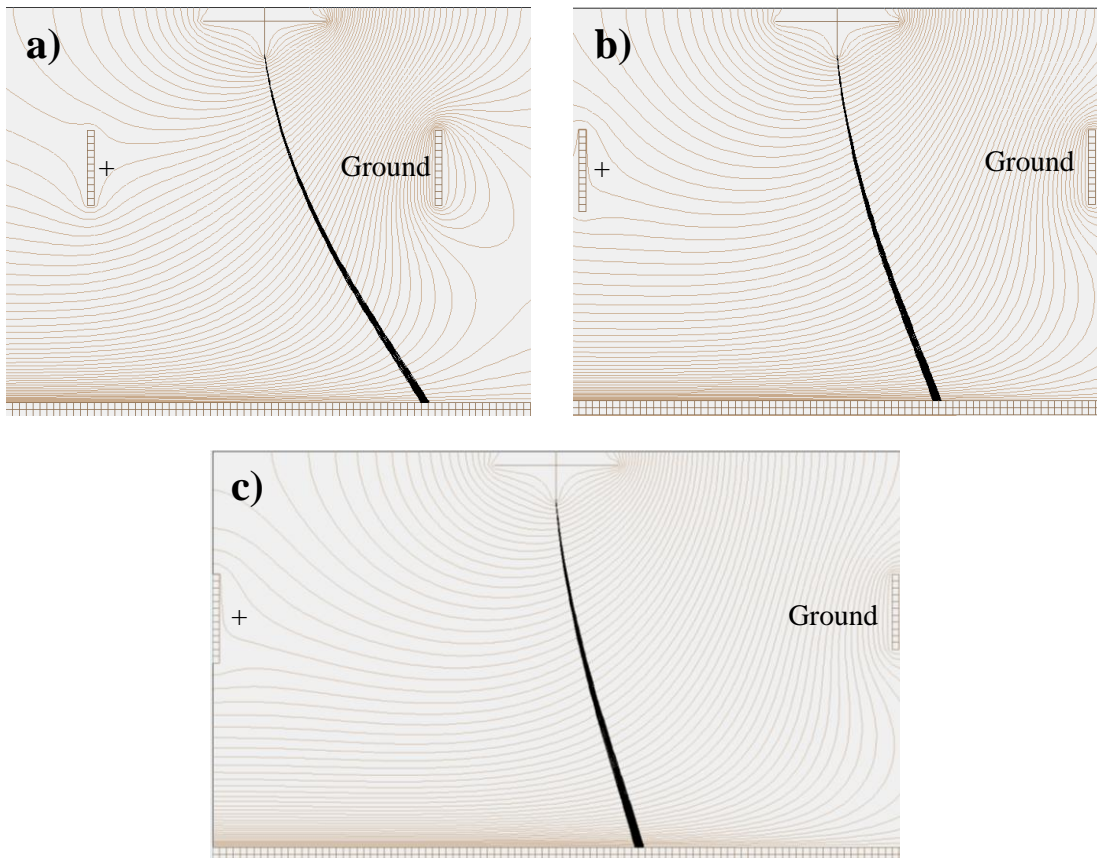


Figure 19. Distance between steering electrodes a) $a = 50$ mm, b) $a = 75$ mm and c) $a = 100$ mm with the following constant parameters ($V1 = 11.8$ Kv; $V2 = 11.5$ kV; $W = 12.5$ mm; $x = 10$ mm).

4. Voltage applied at the steering electrodes V2

Higher voltage applied at the steering electrodes V2 resulted in larger W_p . For most experiments a slightly lower voltage than between the spinneret tip and the collector was chosen and $V2 = 11.5$ kV was used (other electrospinning parameters set as for the modeling (Figure 18)). Only in cases of high voltage signal frequency f and large distances between the steering electrodes a , $V2$ up to 13.5 kV allowed electrospinning. Otherwise, electrospinning was suppressed. The hypothesis, that higher $V2$ resulted tendentially in stronger deflection, was confirmed with the help of modeling (Figure 20).

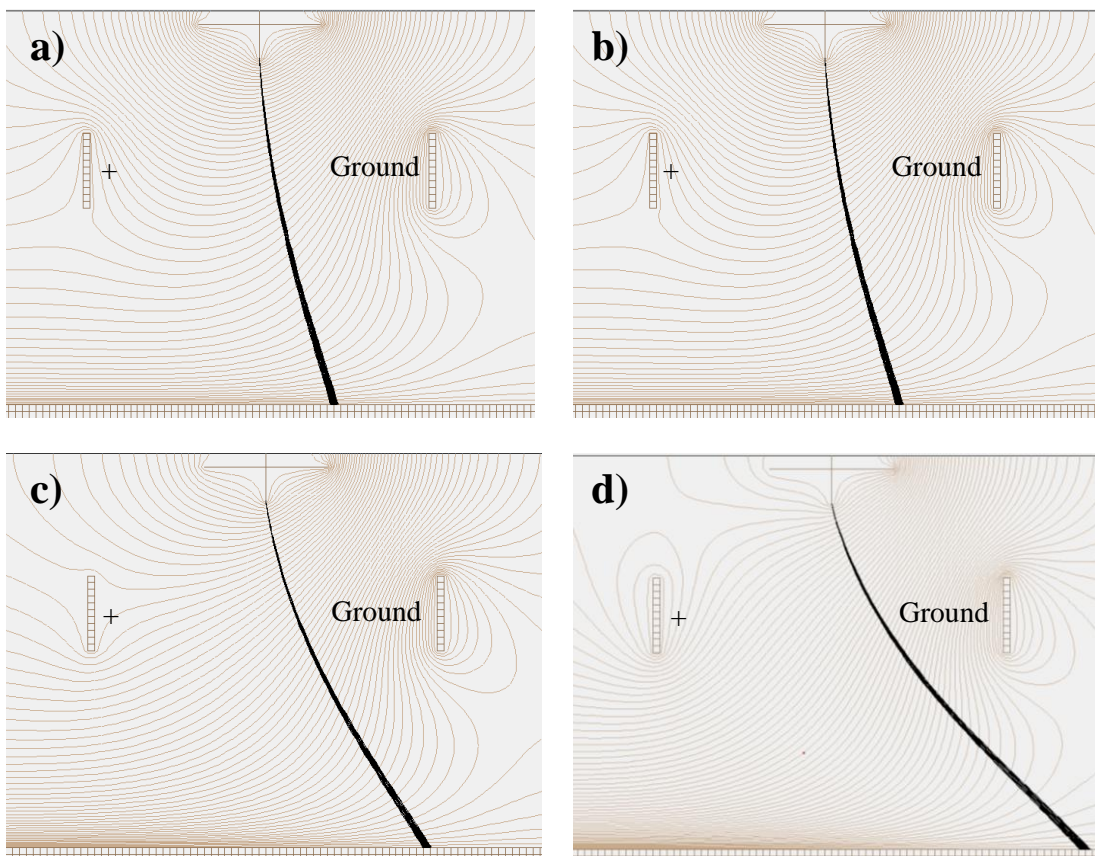


Figure 20. Voltage applied at the steering electrodes a) $V2 = 7.5$ kV, b) $V2 = 9.5$ kV, c) $V2 = 11.5$ kV and d) $V2 = 13.5$ kV with the following constant parameters ($V1 = 11.8$ kV; $W = 12.5$ mm; $a = 50$ mm; $x = 10$ mm).

On the basis of these correlations between electrospinning process parameters and the pattern width W_p , the following setting was identified as the optimum to maximize W_p .

Compromises between fibers pattern width W_p and stable electrospinning was found:

- Steering electrodes width $W = 12.5$ mm
- Electrospinning voltage $V1 = 11.8$ kV
- Steering electrodes voltage $V2 = 11.5$ kV
- Steering electrodes distance $a = 50$ mm
- Steering electrodes positions $x_I = 5$ mm and $x_{II} = 20$ mm

If not differently stated, the optimized conditions were used for one dimensional control of electrospinning.

With a static collector, one dimensional fibers patterns were achieved. As membranes with anisotropic mechanical properties were the aim of this study, two dimensional structures were fabricated by combining one pair of steering electrodes with a collector moving perpendicular to the electric field effect at a speed v (Figure 11). With this configuration, wave fibers structures similar to that of a sine function were fabricated.

The key parameter to influence the fibers pattern width W_p and the period length l_p (Figure 21) was the frequency f of the voltage signal applied on the steering electrodes. In addition, the speed of the collector movement determined the period length l_p of the wave pattern.

The linear correlation between the speed of the collector movement and the period length l_p was obvious. Therefore, the speed of the moving collector was set constant with 0.008 m/s and its impact was not further investigated. Owing to the design of the drive mechanism, the collector stopped for ~0.5 s after a movement of 80 mm before changing the

moving direction. Every stopping of the collector resulted in a shift of the sine like fibers pattern. As a result, a uniformly thick fibrous membrane was fabricated.

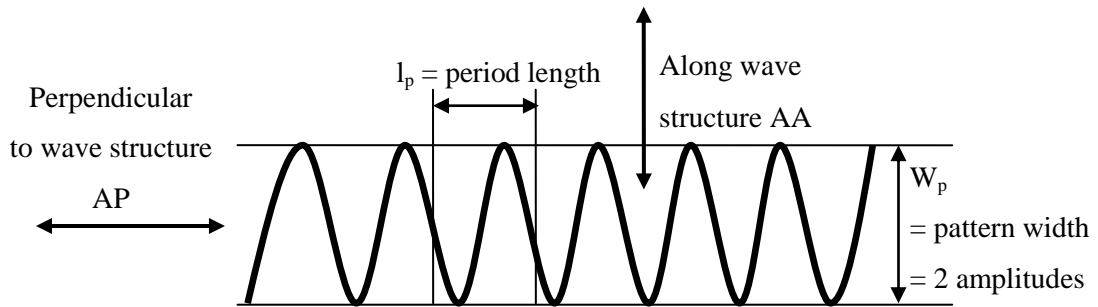


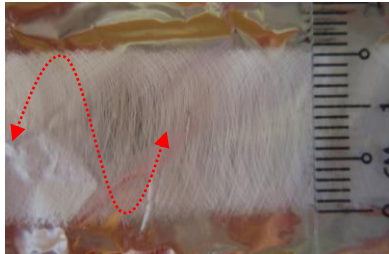
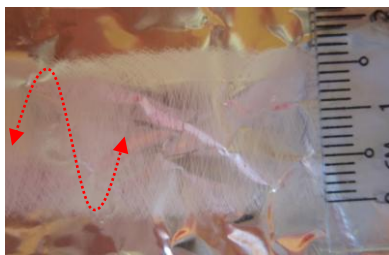
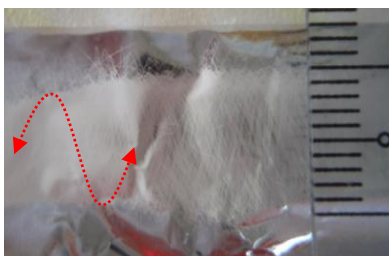


Figure 21. The wave fibers structure fabricated with a one pair of steering electrodes and a moving collector was described by the period length (l_p) and the pattern width (W_p). Within this study, AP indicated the direction perpendicular to the wave structure and AA the direction in line with the wave structure.

The process parameter studied more in depth was the speed of the frequency f of the voltage signal applied on the steering electrodes. Its impact on the period length (l_p) and the pattern width (W_p) were studied experimentally as summarized in Table 6.

Table 6. Pattern width W_p fabricated with one pair of steering electrodes on a moving collector ($V_1 = 11.8$ kV; $V_2 = 11.5$ kV; $W = 12.5$ mm; $x_I = 5$ mm; $x_{II} = 20$ mm; $a = 50$ mm). With increasing frequency of the voltage signal f , the pattern width decreased.

Frequency f Steering electrodes voltage V_2	Wave pattern	Pattern width W_p [mm], Period length l_p [mm]
$f = 250 \text{ min}^{-1}$ $V_2 = 11.5 \text{ kV}$		$W_p = 33.7 \pm 4.0$ $l_p = 47.4 \pm 1.6$
$f = 500 \text{ min}^{-1}$ $V_2 = 11.5 \text{ kV}$		$W_p = 22.1 \pm 1.1$ $l_p = 25.6 \pm 1.0$
$f = 1000 \text{ min}^{-1}$ $V_2 = 11.5 \text{ kV}$		$W_p = 14.7 \pm 0.7$ $l_p = 15.1 \pm 0.6$
$f = 1000 \text{ min}^{-1}$ $V_2 = 13.5 \text{ kV}$		$W_p = 17.9 \pm 0.7$ $l_p = 14.6 \pm 0.6$
$f = 1500 \text{ min}^{-1}$ $V_2 = 13.5 \text{ kV}$		$W_p = 9.4 \pm 1.5$ $l_p = 10.2 \pm 2.1$

The fabricated waved fibers patterns were described by the sine function $y(x;f)$ with the function variables x as the position in horizontal direction and f as the voltage signal frequency

$$y(x; f) = \frac{W_p(f)}{2} * \sin\left(c * \frac{f * x}{v}\right) \quad (\text{Formula 6})$$

where the speed of the moving collector v was ~ 0.008 m/s and $W_p(f)$ was the pattern widths, which were experimentally achieved at voltage signal frequencies f ranging from 250 and to 1500 min^{-1} (Table 6). Constant c was set $c = 0.25$ to fit the sine function to the dimensions of the experimentally fabricated fibers patterns. The function $y(x;f)$ fitted the experimental with errors smaller than 1 mm. With the function $y(x;f)$, an approximate value for the period length of the wave fibers patterns was provided for $250 \text{ min}^{-1} < f < 1500 \text{ min}^{-1}$, under the precondition that the corresponding pattern width W_p (or amplitude) was known.

For higher voltage signal frequencies ($f > 1000 \text{ min}^{-1}$), voltages applied on the steering electrodes V_2 could exceed $V_1 = 11.8$ kV by up to 2 kV. By increasing the frequency from 250 min^{-1} to 1000 min^{-1} , the time, for which the steering electrodes remained charged, was decreased from 0.12 s to 0.03 s. The shorter period of charged state explained the avoided suppression of electrospinning. Therefore, higher V_2 could be applied for higher voltage signal frequencies f . With $f = 1000 \text{ min}^{-1}$, V_2 could be increased from 11.5 kV to 13.5 kV. This strengthened the electric field and therefore the pattern width could be enhanced from 15.8 ± 0.7 mm to 17.9 ± 0.7 mm, whereas the period length l_p was maintained nearly constant. It was shown that the voltage applied at the steering electrodes V_2 could influenced the pattern width W_p without changing the period length l_p , whereas the voltage signal frequency f influenced both of these wave fibers pattern dimensions. Hence, V_2 and f were identified as parameters having different impact on the geometric structure of the wave fibers pattern.

Second, the correlations gained from the experimental and modeling work with one pair of steering electrodes were transferred to a two pairs of electrodes design (Figure 12). The aim with the two electrodes design was to control the polymer jet in two dimensions. However, the optimized electrodes designs achieved for the one steering electrodes design required modification and adaption for the transfer to the two electrodes design. It could not be transferred from the design with one pair of steering electrodes without modification because electrospinning was suppressed by the strong two dimensional electric field. The same effect was observed with positioning the steering electrodes close to the collector with $x = 20$ mm.

To prove, that the method developed for one dimensional control with one steering electrode pair was also applicable for two steering electrode pairs, the voltage signal in channel A and B as well as C and D were set in phase and therefore the electrodes A and C as well as B and D were simultaneously positively charged (Figure 12). Therefore, a linear diagonal pattern was expected and experimentally achieved (Figure 22). Since the experimental results met the expected pattern, the functionality of both the electro-mechanical controller and the steering electrodes was proven. In addition, evidence was given for the controllability of electrospinning in two dimensions.

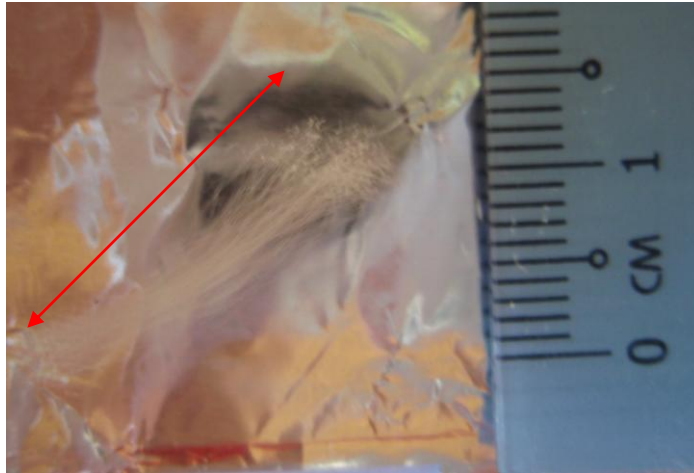


Figure 22. Electrospinning was controlled by two pairs of electrodes with the electrodes A and C as well as B and D being charged in phase. A linear diagonal pattern was fabricated with two pairs of electrodes (Fibers orientation arrow) ($V1 = 11.8$ kV; $V2 = 11.5$ kV; $W = 6.25$ mm; $a = 50$ mm; $x = 15$ mm).

Applying voltage signals on the steering electrodes with phase shifts as in Figure 14, two dimensional fibers patterns, like square fibers patterns and circular fibers patterns, were fabricated.

The electrodes design as optimized for one pair of steering electrodes could not be transferred to the design with two pairs of electrodes because the electrode surface was too large and therefore suppressed electrospinning.

The parameters 1-4 studied and discussed for one pair of steering electrodes were also investigated for the case of two pairs of steering electrodes.

1. Steering electrodes position

Steering electrodes were shown to be more effective with increasing distance from the spinneret tip. However, the maximum distance from the spinneret tip was found to be $x = 10$ mm. Larger distance resulted in the suppression of electrospinning or in fibers collections on the steering electrodes.

2. Steering electrodes width W

For the two steering electrodes, larger width did not enhance the pattern size. However, it was limited to 12.5 mm, as larger electrodes attracted fibers.

3. Geometry and dimensions of the electrodes

Both flat and steering electrodes were investigated considering the achieved fibers pattern size. They were studied depending on the electrode length (Table 7; Table 8). It was defined by the length of the electrodes and the circular electrodes by their diameter. Large electrodes resulted in a decrease of the pattern

For flat electrodes, shorter electrodes resulted in larger pattern size because the electrodes were closer to the positively charged polymer fiber. For $f = 250 \text{ min}^{-1}$, fibers patterns fabricated with steering electrodes length of 50 mm were ~22% larger than that fabricated with a steering electrodes length of 75 mm. For higher voltage signal frequencies ($f > 1000 \text{ min}^{-1}$), an enhancing effect of shorter electrodes was not observed. With a steering electrodes length of 100 mm, no defined fibers patterns were achieved, but random fibers deposition. The experimental results indicated the loss of controllability of the polymer jet by the electric field with increasing electrodes length, therefore increasing distance of the polymer jet from the electrodes and weakened electric field. Instead, a focusing effect of electrospinning was observed.

The same tendency was observed for circular electrodes. Larger diameter and therefore larger distance of the electrodes from the polymer jet resulted in smaller pattern (Table 8). For a circular electrode with 100 mm diameter, uncontrolled fibers deposition was achieved, too.

4. Frequency of the voltage signals f

Like for one pair of steering electrodes, the frequency of the voltage signals f was the parameter chosen to determine the size of the fibers pattern due to its simple changeability. For all electrodes geometries studied, increasing voltage signal frequency f resulted in a decrease of fibers pattern size (Table 7; Table 8).

Table 7. Pattern width fabricated with two pairs of flat steering electrodes ($V_1 = 11.8$ kV; $V_2 = 11.5$ kV; $W = 6.25$ mm; $x = 15$ mm; $a = 50$ mm). With increasing frequency f of the voltage signal the geometric dimensions of the fibers patters (length L_p and width W_p) were decreased.






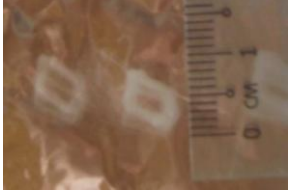

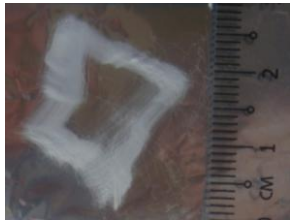
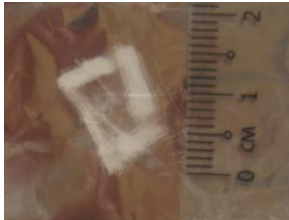
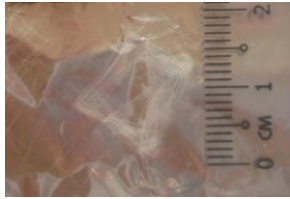
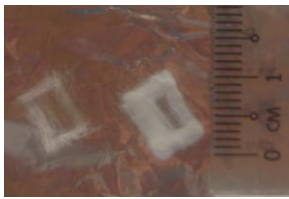

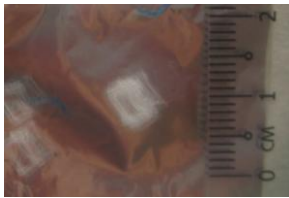


Frequency f [min ⁻¹]	Pattern Dimensions [mm]	
	Plane electrode length 50 mm	Plane electrode length 75 mm
	250	 $L_p = 13.4 \pm 1.2$ $W_p = 12.2 \pm 1.0$
500	 $L_p = 12.3 \pm 1.1$ $W_p = 9.1 \pm 0.3$	 $L_p = 8.3 \pm 0.9$ $W_p = 6.1 \pm 0.7$
1000	 $L_p = 6.6 \pm 0.6$ $W_p = 4.8 \pm 0.6$	 $L_p = 6.3 \pm 0.6$ $W_p = 5.3 \pm 0.2$
1500	 $L_p = 5.1 \pm 0.6$ $W_p = 3.5 \pm 0.2$	 $L_p = 5.1 \pm 0.2$ $W_p = 4.1 \pm 0.2$

Table 8. Pattern width fabricated with two pairs of circular steering electrodes ($V_1 = 11.8$ kV; $V_2 = 11.5$ kV; $W = 12.5$ mm; $x = 10$ mm). Increasing voltage signal frequency f and increasing diameter of the circular electrodes resulted in smaller fibers patterns (length L_p and width W_p).

Frequency f [min^{-1}]	Steering electrodes Dimensions [mm]	
	Circular electrodes diameter 50 mm	Circular electrodes diameter 75 mm
250	 $L_p = 13.6 \pm 2.3$ $W_p = 12.6 \pm 1.7$	 $L_p = 10.9 \pm 0.5$ $W_p = 7.3 \pm 0.8$
500	 $L_p = 10.8 \pm 1.0$ $W_p = 9.1 \pm 0.7$	 $L_p = 7.5 \pm 0.4$ $W_p = 5.2 \pm 0.3$
1000	 $L_p = 5.6 \pm 0.3$ $W_p = 4.6 \pm 0.7$	 $L_p = 4.7 \pm 0.1$ $W_p = 3.2 \pm 0.3$
1500	 $L_p = 4.4 \pm 0.2$ $W_p = 2.8 \pm 0.2$	 $L_p = 4.1 \pm 0.3$ $W_p = 2.9 \pm 0.2$

Comparing the pattern sizes achieved by flat and circular electrodes, the effect of the steering electrodes geometry was shown to have no significant impact on the fibers pattern size (Table 7; Table 8).

5. Voltage applied on the steering electrodes V2

For all investigated devices consisting of two steering electrode pairs, the voltage applied on the steering electrodes was $V_2 = 11.5$ kV, slightly lower than the voltage between the spinneret tip and the collector $V_1 = 11.8$ kV. Higher V_2 resulted in the suppression of electrospinning.

The shape of the fibers patterns as rectangles or squares reflected the square voltage signal provided by the electro-mechanical controller (Figure 14). Ideally, square fibers patterns were expected, however small inaccuracies in the fabrication of the electro-mechanical controller and the steering electrodes design explained the stretching of the square to a rectangle.

In addition, with increasing voltage signal frequency f , the square fibers pattern evolved to a circular pattern. Explanations therefore were that due to the higher speed of the rotating drum the square voltage signal evolved to a signal similar to a sine signal because of some sparking between the electrodes patches applied at the rotating controller drum and the electrodes connected with the channels (Figure 14). Another explanation therefore was the inertia of the polymer jet. Due to the inertia, the polymer fibers movement could not follow the accelerated electric signal.

Besides the patterns size, the quality of the fibers morphology and the impact of the steering electrodes on the fibers morphology was investigated in the following subchapter.

4.2.2 Fibers morphology

The fibers morphology of random fibers, of fibers aligned on a rotating drum and of wave and square pattern fibers fabricated with one and two pairs of steering electrodes was investigated and compared. The fibers morphology electrospun in all this configurations was good.

Fibers aligned on a rotating drum showed a highly one directional orientation because of the high speed of the rotating drum used as collector (Figure 23b). In contrast to the fiber deposition on the rotating drum, electrospinning controlled by one or two pairs of steering electrodes resulted in wave and square structured fibers with a buckling morphology (Figure 24a and Figure 24b). After the deposition of multiple layers of fibers, an overlapping of the buckling structure occurred and therefore the buckling structure was not visible in the SEM image anymore (Figure 23c).

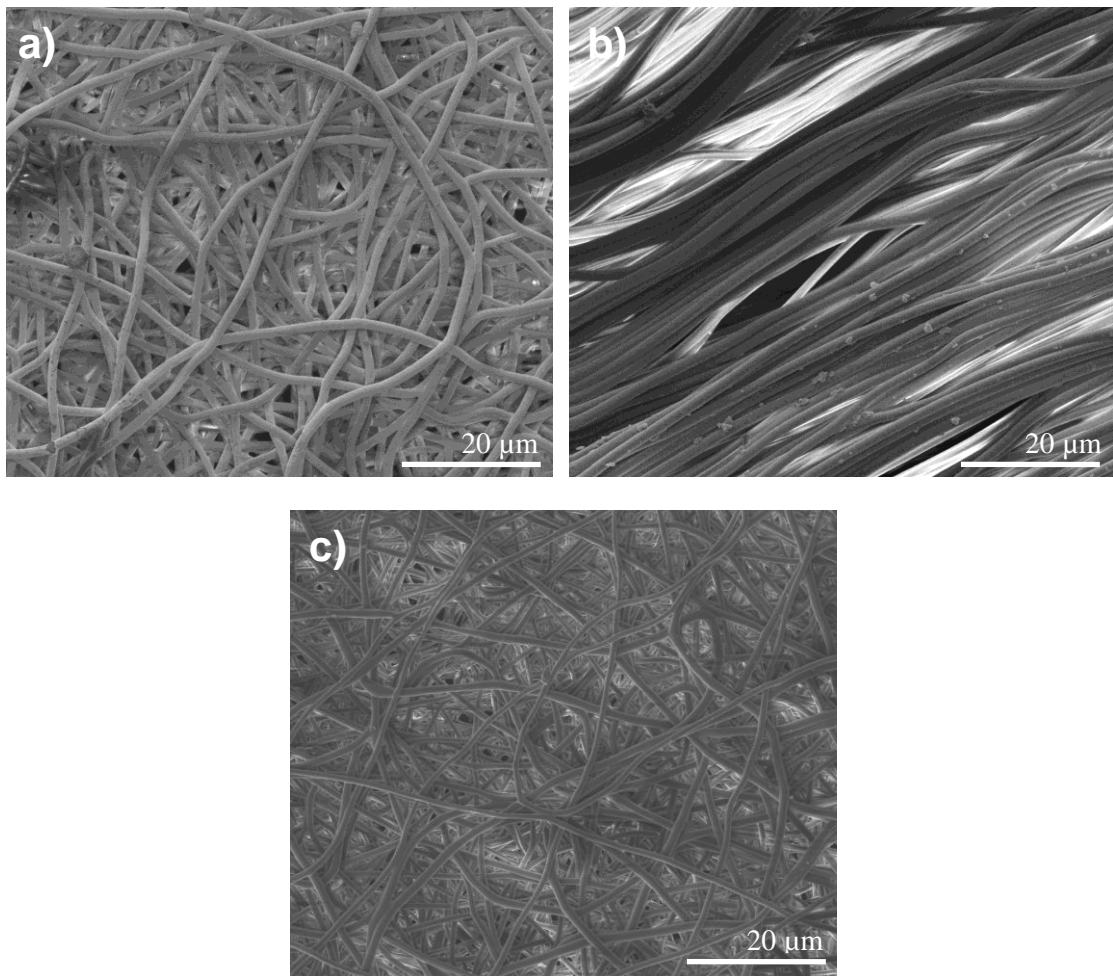


Figure 23. Fibers morphology of a) random fibers ($V_1=11.8$ kV), b) fibers aligned by deposition on rotating drum ($V_1=11.8$ kV), and c) wave structured fibers with buckling morphology fabricated with one pair of steering electrodes ($V_1 = 11.8$ kV; $V_2 = 11.5$ kV; $W = 12.5$ mm; $x_I = 5$ mm; $x_{II} = 20$ mm).

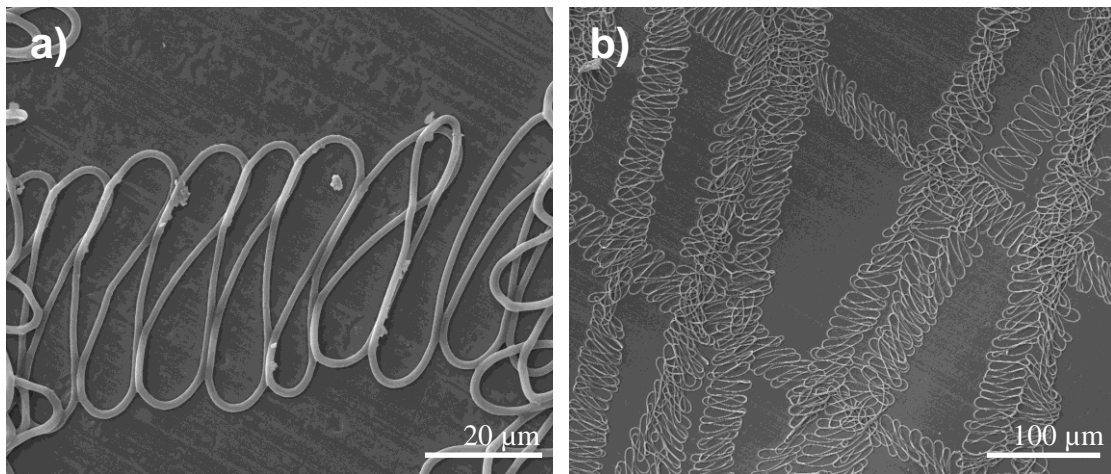


Figure 24. Buckling fibers morphology achieved for fibers controlled with one steering electrode pair or two steering electrode pairs a) buckling structure, and b) overview SEM image (V1 = 11.8 kV; V2 = 11.5 kV; W = 12.5 mm; $x_I = 5$ mm; $x_{II} = 20$ mm;).

The width of the PLACL buckling structure was $37.1 \pm 1.8 \mu\text{m}$, whereas electrospinning focused with electrostatic lens systems achieved a fiber stripe width of $158.0 \pm 13.1 \mu\text{m}$ deposited on a collector moving at ~ 0.1 m/s (Chapter 3.2.2). Han et al. (2007) have reported buckling fibers structures by fibers collection on a moving collector (speed up to 3 m/s). Depending on the electrospinning parameters, e.g. the electrospun polymers, the moving speed of the collector, buckling fibers structures with a width ranging between $10 \mu\text{m}$ and $50 \mu\text{m}$ were fabricated. As in this thesis, Han et al. (2007) reported buckling structures for electrospinning with comparatively small distance between the spinneret tip and the collector D.

The hypothesis was derived that a certain relative speed between the collector movement and polymer jet was essential in order to achieve a buckling structure and to avoid fibers with fibers agglomerations. The polymer jet movement was driven by the electric field effect based on charging and discharging of the steering electrodes. The polymer jet moved with a speed higher than 0.3 m/s at the collector surface. The collector speed of 0.1 m/s

applied in this study was not sufficient in order to achieve a buckling structure because the relative speed between the polymer jet and the collector was not sufficient and therefore resulted in a thicker and wider fibers stripe.

One explanation for the phenomenon of the buckling structure was the bending instability of the polymer jet. Due to its small width, the instability had to occur very close to the collector surface. This explanation was in accordance with that given by T. Han. et al. (2007).

The comparatively short distance between the spinneret tip and the collector $D = 50$ mm and therefore short in comparison to conventional electrospinning conditions as well as the high polymer concentration and therefore high solution density resulted in membrane with a fibers diameter of 1154.8 ± 147.5 nm. Controlling electrospinning with steering electrodes further eliminated instabilities of the polymer jet, therefore further decreased the stretching length of the polymer jet and therefore resulted in fibers with even larger diameter with 1306.9 ± 162.1 nm. The PLACL fibers deposited on the rotating drum had a diameter of 1289.2 ± 236.1 nm because the same PLACL solution and the same electrospinning conditions as for the random PLACL and the PLACL fibers controlled with steering electrodes were applied.

The polymer jet being controlled with two steering electrode pairs did not differ from that controlled with one steering electrode pair. As only the direction of the polymer jet movement differed, the membrane morphology was equal, but the fibers structure of the membrane differed as discussed in the subchapter 4.2. Whereas with one pair of steering electrode, wave fibers structures were fabricated on moving collectors, square and circular fibers structures were fabricated with two pairs of steering electrodes.

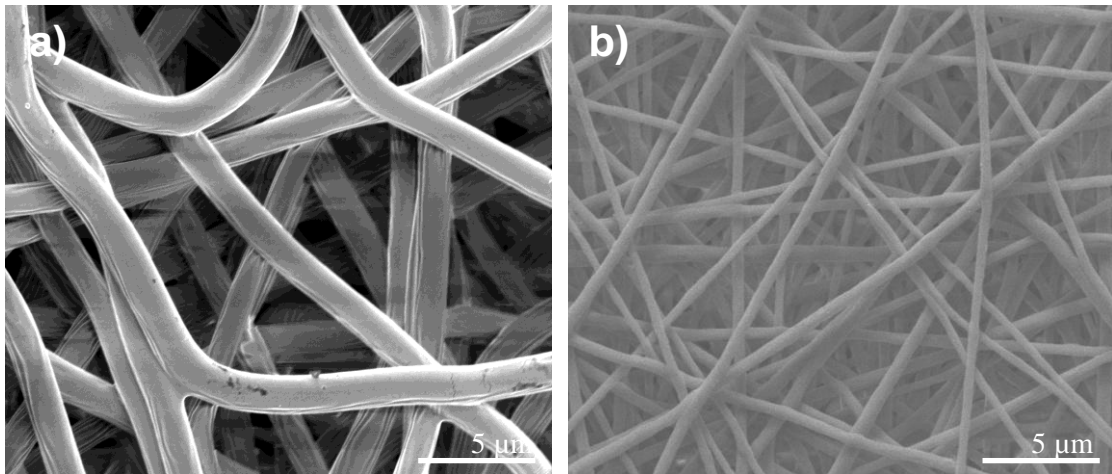


Figure 25. Impact of plasma treatment on the fibers morphology a) random PLACL fibers before plasma treatment, and b) random plasma fibers after plasma treatment.

Plasma treatment resulted in a smaller fibers diameter. After one minute of plasma treatment, a reduction of the fibers diameter of about 55 % and 35 % was measured for random and aligned fibers, respectively. The decrease of the fibers diameter could be explained by the degradation of the polymer due to plasma exposure. Besides the fibers diameter, the effect of plasma treatment on the wettability and the pore size of the membrane were investigated (Table 9).

Table 9. Effect of plasma treatment on the fibers diameter and the hydrophilic characteristics of random and aligned PLACL fibers.

Fibers structure	Plasma treatment	Fibers diameter [nm]	Hydrophilic characteristics (Contact angle)
Random	non-plasma treated	1154.8 ± 147.5	122.2 ± 7.0
	plasma treated	498.9 ± 110.2	53.2 ± 6.5
Aligned with electrodes	non-plasma treated	1306.9 ± 162.1	125.9 ± 2.1
	plasma treated	858.5 ± 89.0	47.1 ± 10.0

On the basis of contact angle studies, the highly hydrophobic nature of PLACL fibers without any further processing was found. With the help of plasma treatment, the contact angle could be substantially reduced indicating the enhanced wettability of the PLACL fibers with an approximately equal effect for both random and aligned fibers (Figure 13). Evidence for the improved wettability due to the plasma treatment were on average about two time thicker fibrous membranes after a 15 days exposure to cell culture medium in case of plasma treatment. This effect was explained with the improved hydrophilic properties of the fibrous membranes. Because of the enhanced wettability of the fibrous membrane, plasma treatment was expected to improve the cell growth.

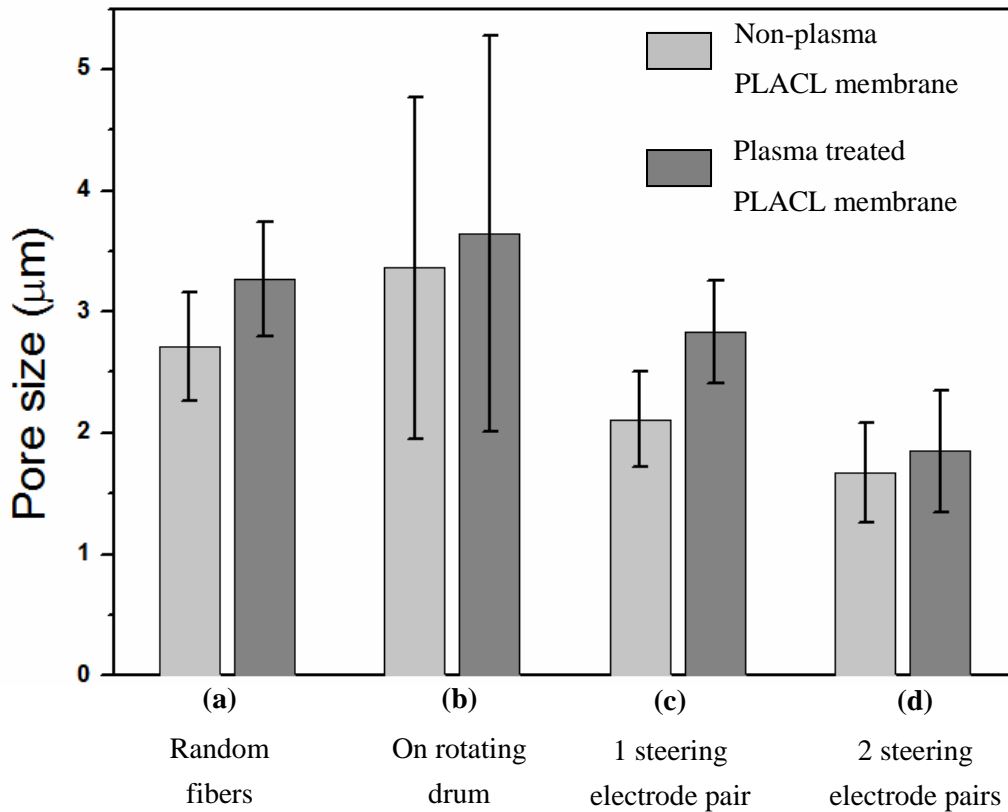


Figure 26. Effect of plasma treatment on the pore size of a) random PLACL fibrous membrane, b) aligned PLACL fibrous membrane collected on a rotating drum, c) PLACL fibrous membrane deposited with one steering electrode pair, and d) PLACL fibrous membrane deposited with two steering electrode pairs.

The pore size was shown to be affected by fibers structure and morphology. The usage of steering electrodes and therefore controlled electrospinning resulted in a decrease of the pore size of ~15-30%. The decrease of the pore size was explained with the changed fibers morphology due to the buckling structure, with the increased fibers diameter and with the more focused fibers deposition resulting in smaller pore size as described in chapter 3.2.1.1. In contrast, membranes with fibers aligned on a rotating drum had larger pores than membranes with random fibers because the membrane had a very loose structure perpendicular to the fibers orientation.

With plasma treatment, the fibers diameter was reduced and therefore bigger pore sizes were achieved. The reason for this effect was the polymer degradation on the fibers surface and of the therefore decreasing fibers diameter. The plasma treatment was expected to have high relevance for cell growth due to its positive effect on the pore size and the hydrophilic properties of the membrane.

In the context of cardiac tissue engineering, other researchers identified the scaffold pore size as a central property. In literature, a wide range of pore sizes being the optimum for cardiac tissue engineering has been reported. On the one hand, a sufficient average pore size is beneficial for a good mass transport and to allow sufficient vascularization of the scaffold following transplantation. Pore sizes of 50-100 μm were reported to be sufficient to allow the vascularization of the freeze dried collagen scaffold following transplantation (Radisic et al., 2005). On the other hand, excessively large pores could impair vascularization because endothelial cells were not able to bridge pores greater than the cell diameter. The pore sizes of the electrospun fibrous membranes of 1.8 – 3.5 μm were much smaller than these of the freeze dried scaffolds. However, fibrous scaffolds with typically few micrometers pore size have been found suitable for spreading and holding the cells by filapodia like structure for the proliferation. Due to interconnected pores, uniform distribution of cells was achieved and good diffusion of oxygen and nutrients was shown for fibrous scaffolds (Ito et al., 2005; Venugopal et al., 2008, Venugopal et al., 2010; Zhang et al., 2007). Therefore, the achieved pore size was evaluated as sufficient for tissue engineering.

4.2.3 Mechanical properties of patterned fibers structures

One of the main aims within this study was to enhance the elasticity of the fibrous membrane structure. The relevance of a highly elastic material for cardiac tissue engineering is described in the Appendix 1. To characterize and compare the different PLACL fibers structures, stress-strain curves were recorded for the following membrane structures:

- Random fibers structure (Figure 27).
- Aligned fibers collected on a rotating drum.
- Wave structured fibers with buckling morphology electrospun with one pair of steering electrodes (AA: in fibers wave direction; AP: perpendicular to fibers wave direction) (Figure 28).
- Square structured fibers with buckling morphology electrospun with two pairs of steering electrodes (Figure 29).

On their basis, mechanical properties elasticity and the tensile strength of the fibrous membrane were determined. The different fibers structures and morphology were studied as deposited, after plasma treatment, after exposure to DMEM and after plasma treatment combined with exposure to DMEM.

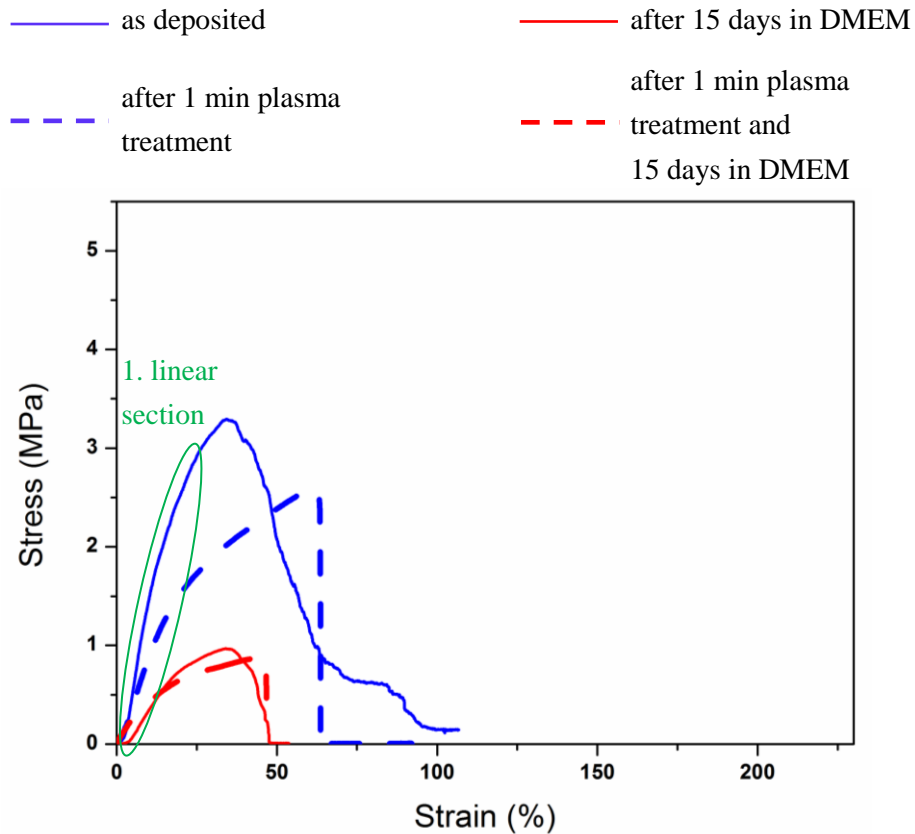
PLACL Fibrous

Figure 27. Stress (σ)-strain (ϵ) curves of random fibers structure fabricated with a $V_1 = 11.8$ kV (Same scale for all σ - ϵ curves).

Comparing the stress-strain curves of non-plasma treated and plasma treated random PLACL fibers, plasma treated fibrous membranes showed an abrupt breakage and therefore a more brittle behavior in comparison with non-plasma treated fibrous membranes (Figure 27). Tendentiously, this observation also occurred for wave and square fibers structures with buckling morphology (Figure 28, Figure 29). However, these structures tended to a more abrupt breakage even before plasma treatment than random fibers structures.

Besides, the stress-strain curves of fibrous membranes with random fibers structure showed one section with linear correlation between strain and stress indicating the elastic part of the stress-strain curves (Figure 27). In contrary to random fibers structures, wave and

square fibers structures with buckling morphology showed two sections with linear correlation between strain and stress with different slopes (Figure 28, Figure 29). The first section was steeper and therefore this part of the strain-stress curve indicated a higher E-modulus, whereas the second slope was significantly flatter and therefore indicated a lower E-modulus than the first section.

It was hypothesized that the reason of this phenomenon was the buckling morphology of the fibers. Fusion and therefore weak bonding of the buckling curves could explain this strain-stress behavior. Before debonding of the fibers fusion, the fibrous membrane was comparatively stiff representing the first linear section of the stress-strain curve. After a non-linearity of this curve explained with the process of debonding at the buckling curves, a second very elastic part of the stress-strain curve was identified. In second section, the low E-modulus and therefore high elasticity were explained with the flexible fibers structure because of the debonded buckling curves.

The proportion between the first and the second slope of the stress-strain curves as well as the force required to overcome the first stiffer section gave evidence for this hypothesis (Figure 28, Figure 29). By plasma treatment, heat was induced to the fibers and therefore the fusion bondings were strengthened. Therefore, the first stiffer section of the stress-strain curve was more shaping than without plasma treatment, whereas the second section became shorter with plasma treatment. In addition, after plasma treatment, higher forces had to be applied in order to overcome the stiffer first section of the stress-strain curve (Figure 28; Figure 29).

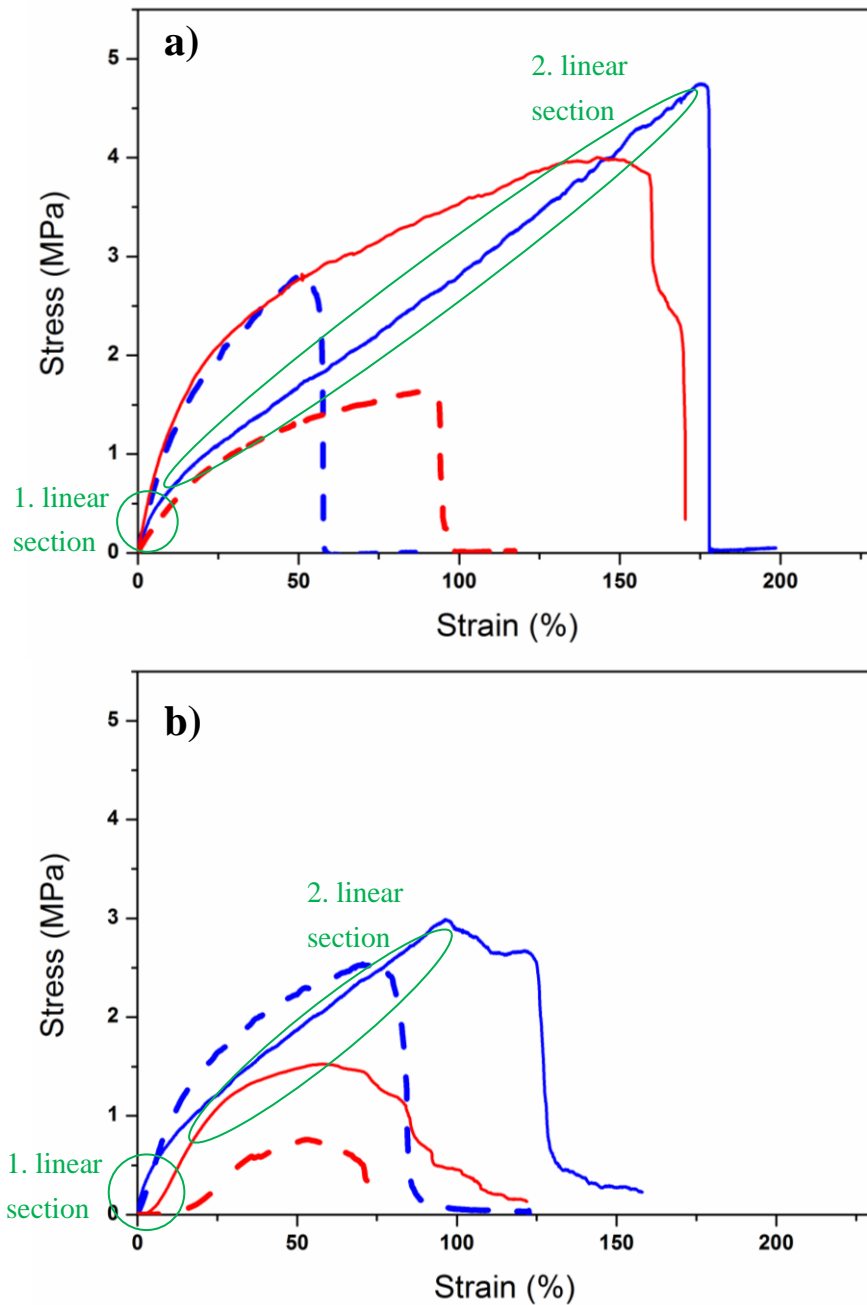


Figure 28. Stress (σ)-strain (ϵ) curves of wave structure fabricated with one pair of flat steering electrodes at the following electrospinning conditions: $W = 12.5$ mm; $V_1 = 11.8$ kV; $V_2 = 11.5$ kV; $x_I = 5$ mm; $x_{II} = 20$ mm; $a = 50$ mm, $f = 50$ min⁻¹. These conditions were applied for the fabrication of wave structure fibers within the mechanical studied if not differently stated. Measurement in a) in AA direction, and b) in AP direction.

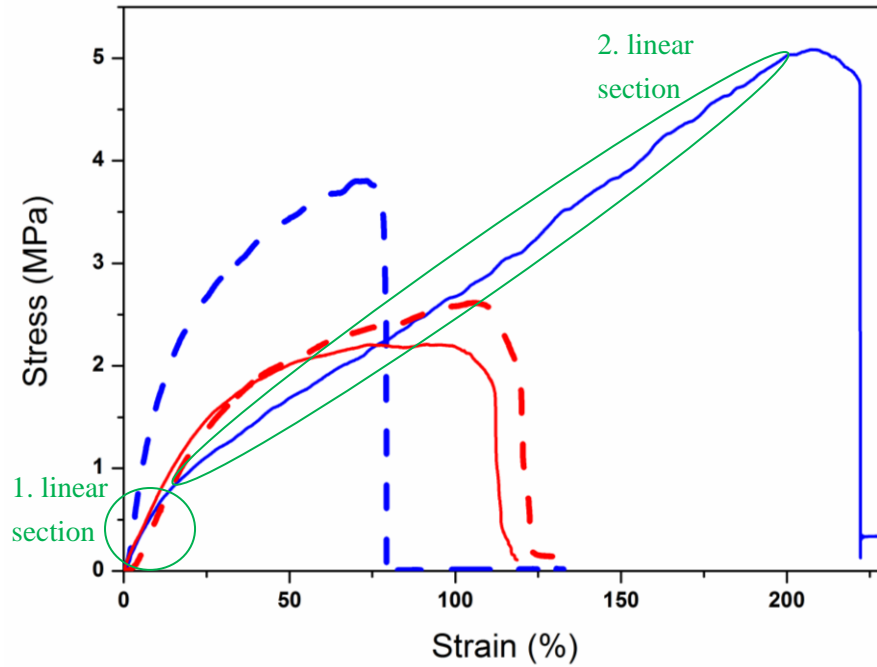


Figure 29. Stress (σ)-strain (ϵ) curves of square structure membranes fabricated with two pairs of flat steering electrodes at the following electrospinning conditions: $V_1 = 11.8$ kV; $V_2 = 11.5$ kV; $W = 6.25$ mm; $x = 15$ mm; $a = 50$ mm, $f = 50$ min⁻¹. These conditions were applied for the fabrication of square structure fibers within the mechanical study if not differently stated.

In order to give a complete description of the mechanical properties, both the slope of the first and second linear section were determined and the E-modulus before and after debonding of the buckling curves was determined in the following subchapter. The explanation stated here was used as the basis for discussions of the E-modulus and the tensile strength.

4.2.3.1 Elasticity

Aligned PLACL fibers deposited on a rotating drum had highly anisotropic E-modulus with 36.80 ± 13.54 MPa in fibers direction and 0.023 ± 0.005 MPa perpendicular to the fibers direction (Table 10).

The E-modulus of random fibers structure was higher by a factor of two than wave or square patterns with buckling morphology before debonding of the buckling curves.

Comparing the E-modulus before and after debonding of the buckling structure, the E-modulus was by a factor of 4-5 times lower. Therefore, the fused buckling fibers structure could advance the elasticity of the fibrous membrane.

Non-plasma treated samples had a lower E-modulus before debonding of the buckling curves in AA direction than in AP direction, whereas after plasma treatment the difference in elasticity was not measured anymore. This effect was explained by the buckling morphology enhancing the elasticity in AA direction before plasma treatment. After plasma treatment, the fibers fusion was strengthened; the buckling structure hardly contributed to the elasticity before bonding and explained the increase of the E-modulus of the fibrous membrane. The elasticity of the membrane was approximately isotropic. The same effect was also observed in the section after debonding of the buckling structure (Table 10).

Table 10. E-modulus without DMEM

Studied parameter: fibers structure and morphology depending on fabrication technique; no plasma treatment (N), with plasma treatment (P).

(AA: in fibers wave direction; AP: perpendicular to fibers wave direction)

Fibers structure	Plasma treated	Before debonding of buckling structure		After debonding of buckling structure	
		E-modulus [MPa]	Standard deviation [MPa]	E-modulus [MPa]	Standard deviation [MPa]
Random	N	19.83	4.27		
	P	13.75	7.42		
Rotating drum perpendicular to fibers direction	N	0.023	0.005		
Rotating drum in fibers direction	N	36.80	13.54		
Wave structure AP direction	N	9.70	3.59	2.60	0.84
	P	10.24	4.47	2.45	1.39
Wave structure AA direction	N	5.39	2.06	1.39	0.47
	P	9.54	4.43	3.03	1.13
Square structure	N	7.30	2.41	2.37	0.80
Square structure	P	11.63	5.43	2.18	0.89

In order to simulate the effect of cell culturing and exposure to DMEM on the E-modulus of the fibrous membrane, they were kept in DMEM for 15 days at 37°C (Table 11).

After 15 days in DMEM, random, wave and square fibers structures showed enhanced elasticity. For wave and square fibers structures with buckling morphology, the decrease of the E-modulus was varied before debonding of the buckling structure, whereas after

debonding of the buckling structure, the E-modulus was decreased by a factor of ~2 to an E-modulus of ~1 MPa (Table 11).

An exception was the E-modulus in fibers direction of aligned fibers deposited on a rotating collector. The E-modulus was maintained at 34.94 ± 11.71 MPa and was therefore hardly reduced by DMEM. The fiber structure was too loose to apply forces perpendicular to the fibers direction after 15 days in DMEM (Table 11).

Table 11. E-modulus after 15 days exposure to DMEM.

Studied parameter: fibers structure and morphology depending on fabrication technique; no plasma treatment (N), with plasma treatment (P).

(AA: in fibers wave direction; AP: perpendicular to fibers wave direction)

Fibers structure	Plasma treated	Before debonding of buckling structure		After debonding of buckling structure	
		E-modulus [MPa]	Standard deviation [MPa]	E-modulus [MPa]	Standard deviation [MPa]
Random	N	6.74	2.18		
	P	5.55	1.77		
Rotating drum in fiber direction	N	34.94	11.71		
	P	25.09	8.78		
Wave structure AP direction	N	5.01	1.44	1.03	0.25
	P	3.98	1.55	1.25	0.43
Wave structure AA direction	N	5.94	1.26	1.11	0.34
	P	4.56	1.46	1.18	0.57
Square structure	N	6.91	1.58	1.03	0.31
	P	6.57	2.24	1.08	0.39

The correlation between the dimensions of the wave fibers structures and the E-modulus was studied in-depth (Table 12). These correlations were of relevance in order to be able to influence the E-modulus of the fibrous membrane in a defined way.

With Formula 6, an approximate description of the wave fibers structure was developed depending on the voltage signal frequency f , the pattern width W_p and the collector speed v . Besides, higher voltage V_2 applied at the steering electrodes had an influence on the dimensions of the wave fibers structure. Since the buckling morphology was hypothesized to play a central role to reduce the E-modulus, the slope of the fibers waves had an impact on the E-modulus of the membrane. With a higher maximum slope of the wave fibers structure, the buckling morphology was assumed to contribute less to the elasticity of the fibrous membrane in AP direction. The slope of the wave fibers structure was approximately determined by the derivation of the Formula 6

$$\frac{\partial y(f)}{\partial x} = \frac{W_p(f) * c * v * f}{2} * \cos\left(c * \frac{f * x}{v}\right) \quad (\text{Formula 7})$$

As for Formula 6, W_p was measured experimentally, $c = 0.25$ was chosen and $v = 0.008$ m/s was maintained constant. With increasing f from 250 to 1000 min^{-1} and at the same time decreasing W_p , the E-modulus in AP direction before and after debonding of the buckling structure increased and therefore followed the hypothesized correlation (Table 12). (Only one E-modulus value after debonding of the buckling structure with $f = 250$ min^{-1} and $V_2 = 11.5$ kV did not follow this correlation and was explained with tolerances in fabrication and measurement of the membrane). Increasing V_2 to 13.5 kV ($f = 1000$ min^{-1}) resulted in a higher maximum slope of the wave fibers pattern (Table 6). Therefore the E-modulus in AP direction after debonding of the buckling structure was higher (Table 12).

Table 12. The E-modulus in AP direction of membranes fabricated with one pair of steering electrodes ($V_1 = 11.8$ kV; $W = 12.5$ mm; $x_I = 5$ mm; $x_{II} = 20$ mm, $a = 50$ mm). f and V_2 were the varied parameters. The E-modulus was compared with the maximum slope (Formula 7) of the function approximating the fibers wave pattern numerically (Formula 6).

(AP: perpendicular to fibers wave direction)

Wave fibers structure		Before debonding of buckling structure		After debonding of buckling structure		Max. slope calculated on basis of Formula 7
f [min^{-1}]	V_2 [kV]	E-modulus [MPa]	Standard deviation [MPa]	E-modulus [MPa]	Standard deviation [MPa]	
250	11.5	9.80	3.59	2.02	0.45	± 2.19
500	11.5	12.81	4.11	1.72	0.32	± 2.88
1000	11.5	14.08	3.57	2.08	0.55	± 3.83
1000	13.5	12.14	2.91	3.05	0.73	$> 3.83,$ < -3.83

4.2.3.2 Tensile strength

Besides the elasticity, the tensile strength, which is the maximum stress the scaffold can carry, was another relevant mechanical characteristic of the tissue engineering scaffold.

Table 13. Tensile strength of the PLACL membranes with different structures and morphologies; non-plasma treated (N), and plasma treated (P) without DMEM exposure and after 15 days of DMEM exposure.

(AA: in fibers wave direction; AP: perpendicular to fibers wave direction)

Fibers structure	Plasma treated	Without DMEM exposure		After DMEM exposure	
		Tensile strength [MPa]	Standard deviation [MPa]	Tensile strength [MPa]	Standard deviation [MPa]
Random	N	3.69	1.46	1.03	0.40
	P	2.42	0.96	0.84	0.35
Rotating drum					
Perpendicular to fiber direction	N	0.80	0.32		
Rotating drum in fiber direction	N	19.4	3.79	6.15	2.16
	P			5.89	1.74
Wave structure					
AP direction	N	3.34	0.59	0.93	0.04
	P	2.75	0.87	0.57	0.17
Wave structure					
AA direction	N	2.95	1.24	1.84	0.44
	P	2.65	1.18	1.53	0.68
Square structure					
	N	4.81	1.72	2.09	0.61
	P	3.74	1.66	2.01	0.72

The tensile strength was affected by both plasma treatment and DMEM exposure. After plasma treatment of the PLACL membranes, a consistent decrease of the tensile

strength was measured. The decrease varied between 10% and 34% (Figure 9). The decrease of the tensile strength could be explained with the polymer degradation during the plasma treatment resulting in smaller fibers diameter (Chapter 4.2.2).

In addition, exposing the fibrous membrane to DMEM for 15 days reduced the tensile strength for 38% - 80% depending on the fibers structure and membrane morphology. With exposure to DMEM, the tensile strength developed in an anisotropic way. In AP direction, it lost about ~80% of its tensile strength due to the lack of fibers interconnections. In contrary, the fibrous membrane with wave structure lost only ~38% in AA direction because the buckling waves were oriented in this direction. In contrary the wave fibers structure, the loss of tensile strength of the square fibers structure was ~57% isotropic and was between the value for AA and AP of the wave fibers structure (Figure 9).

Table 14. The tensile strength in AP direction (AP: perpendicular to fibers wave direction) of membranes fabricated with one pair of steering electrodes ($V_1 = 11.8$ kV; $W = 12.5$ mm; $x_I = 5$ mm; $x_{II} = 20$ mm; $a = 50$ mm). f and V_2 were the varied parameters. The E-modulus was compared with the maximum slope (Formula 7) of the sine function approximating the wave pattern numerically (Formula 6).

Wave fibers structure		Tensile strength [MPa]	Standard deviation [MPa]	Slope calculated on basis of Formula 7
f [min ⁻¹]	V_2 [kV]			
50	11.5	3.34	0.59	± 2.19
100	11.5	3.30	0.54	± 2.88
200	11.5	3.18	0.63	± 3.83
200	13.5	2.17	0.67	$> 3.83,$ < -3.83

Like the E-modulus, the tensile strength was correlated with the maximum slope of the wave fibers structure. With increasing maximum slope of the wave fibers structure because of higher f or V_2 , the tensile strength decreased because the number of fibers interconnections in AP direction was lower (Table 14). Therefore, evidence was given to prove the relevance of the fibers orientation and the buckling structure on the mechanical properties of the membrane.

4.2.4 Cell culturing with cardiomyocytes

Random and wave structured (standard condition; $f = 250 \text{ min}^{-1}$) fibers (PLACL) were fabricated by electrospinning method for cardiac tissue engineering. Rabbit cardiomyocytes (CMs) were used for cell culturing and biocompatibility testing. The aim was to prove that the buckling fiber structure and the fibers electrospun with steering electrodes have potential for cardiac tissue engineering.

The proliferation of CMs was investigated by MTS assay (Figure 30). After 5 days of cell culture, the plasma treated samples showed 10-20% higher cell proliferation than non-plasma treated samples. The difference in cell proliferation on random structure and wave fibers structure with buckling morphology was negligible. After 10 and 15 days of cell culture, MTS assays gave two indications: First, plasma treatment improved proliferation on PLACL fibers both with random and wave structure by 32-34% after 10 days and ~60% increased after 15 days of cell culturing. Second, the samples with a wave fibers structure and a buckling morphology showed ~20% higher cell proliferation after 10 and 15 days.

Biocompatibility was proven and CMs also grow significantly higher on buckling fiber structure morphology. However, cell growth has to be enhanced in future studies as cell delivery is a central function of the cardiac patch besides ventricular restrain. Besides, the

elasticity has to be further enhance by electrospinning more elastic polymers like PGS with the presented controlling techniques. MTS assays proved that the wave structure and the buckling morphology of electrospun fibers with steering electrodes enhanced cell proliferation.

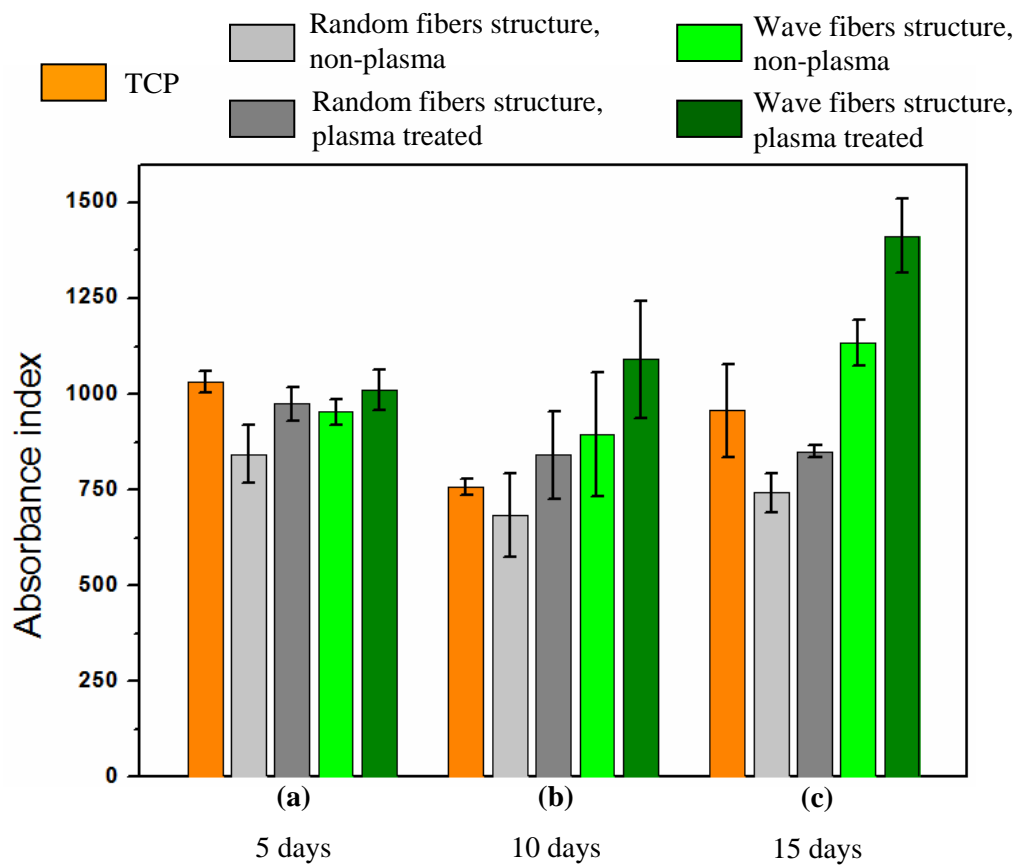


Figure 30. MTS assay for CM proliferation on TCP on PLACL fibrous membranes with random structure and wave structure with one pair of steering electrodes under standard conditions, after a) 5 days, b) 10 days, and c) 15 days of cell culturing.

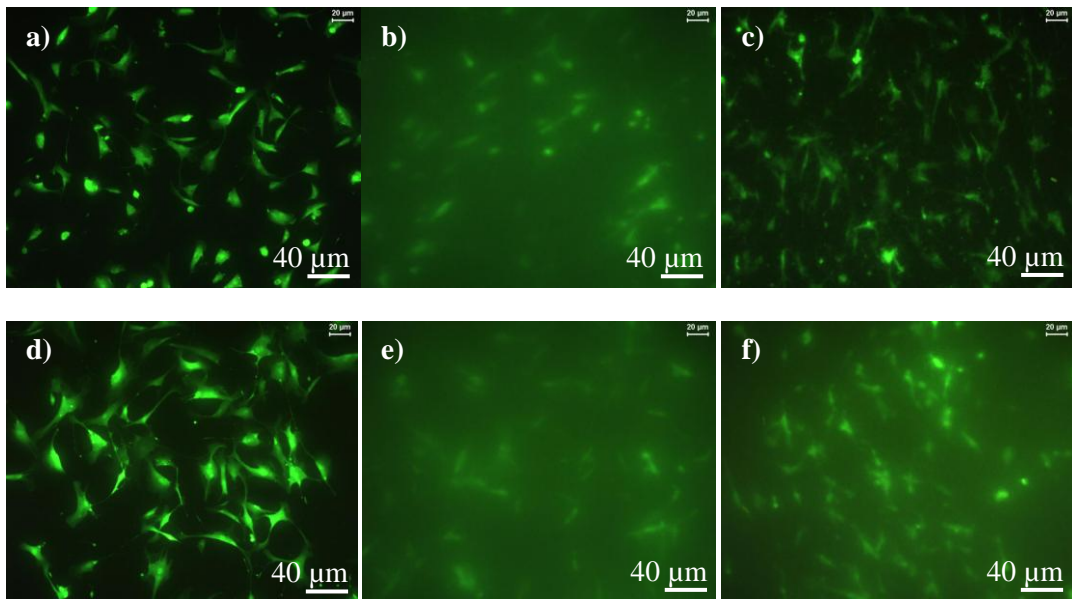


Figure 31. Morphology of CMs after 10 days of cell culturing a) TCP, b) PLACL fibers without plasma treatment, and c) PLACL fibers with plasma treatment as substrate. After 15 days of cell culturing d) TCP, e) PLACL fibers without plasma treatment, and f) PLACL fibers with plasma treated fibrous substrate.

The positive effect of plasma treatment of fibrous scaffolds for CMs growth was confirmed with CMFDA staining. Plasma treated samples showed a higher number of CMs adhesion after 10 and 15 days of culture. In addition, higher percentage of CMs was induced bi/multipolar elongations of the CMs, which were enhanced on plasma treated samples forming a network with each other during its growth. On the contrary, a higher percentage of cells had a spherical morphology and therefore indicated weak adhesion to the fibers substrate on non-plasma treated PLACL fibers. As expected, the number of cells increased between the measurement at day 10 and day 15 of the cell culture study.

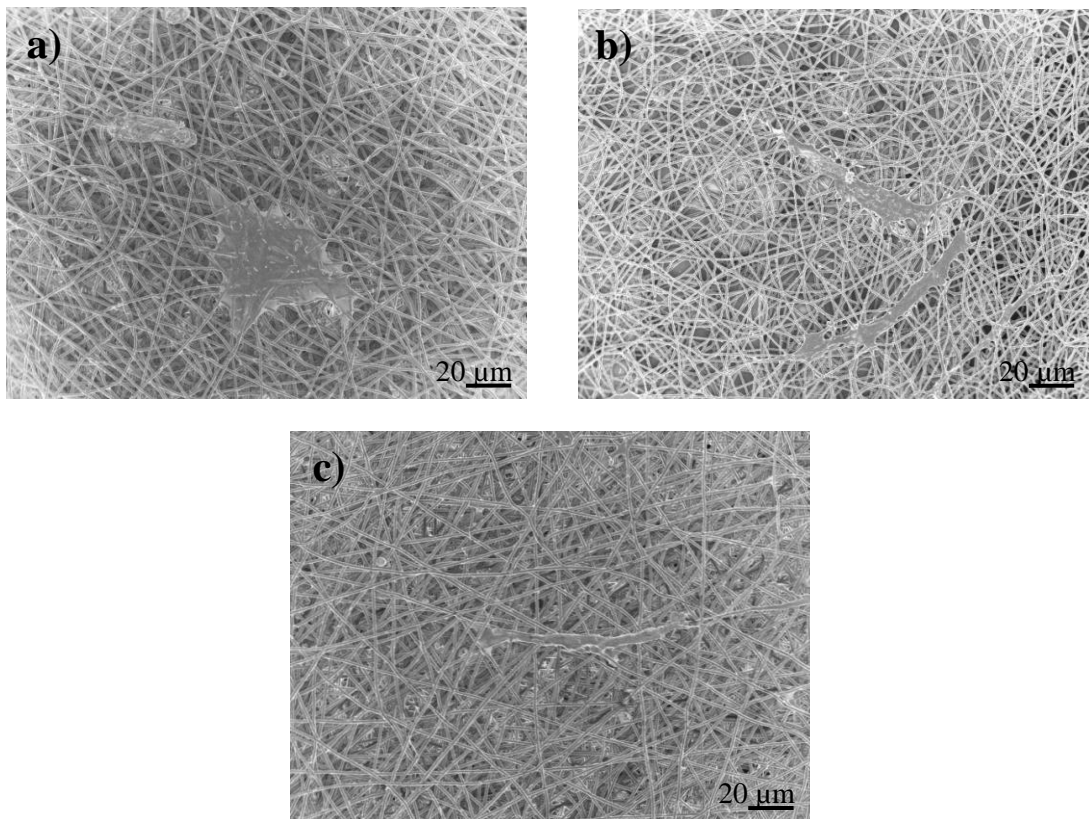


Figure 32. SEM images of CMs cultured for a) 10 days on plasma treated random PLACL fibers, b) 10 days on plasma treated PLACL fibers with wave structure, c) 15 days on non-plasma treated random PLACL fibers.

SEM images observed for 10 and 15 days (Figure 32) of cell culturing showed normal morphology of CMs. Cell orientated along the direction of fibers, clustered the fibers in a longitudinal fashion and showed normal bipolar and tripolar extensions. Significantly higher number of CMs with the longitudinal morphology was observed for plasma treated fibrous scaffolds (Figure 34a and Figure 34b). Non-plasma treated fibrous scaffolds, substantial quantity of CMs with spherical morphology and therefore poor adhesion to the fibrous scaffold were observed.

Consolidating the results from MTS assays, CMFDA staining and SEM analysis, a positive effect of the patterned fibers with buckling structure morphology was indicated and

its biocompatibility was proven for cardiomyocytes. Therefore, the fibrous scaffold structure developed in this study was proven to have potential for the application in cardiac tissue engineering.

However the number of cells on the fibers was not sufficient. Solutions to enhance the number of cells growing on the scaffold were discussed in the subchapter 4.3.

4.3 Discussion

For one dimensional control, pattern sizes of ~33 mm length were achieved. Therefore, the electrospinning polymer jet could be controlled over a width of ~33 mm with one pair of steering electrodes. With two pairs of steering electrodes and therefore two dimensional control over the polymer jet movement, controllability over a width of ~13 mm could be reported. Besides, the pattern size and structure could be correlated with process parameters like the voltage signal frequency f , the voltage applied at the steering electrodes V_2 and the steering electrodes geometry. Furthermore, these process parameters were shown to have a predictable impact on the mechanical properties of the fibrous membrane.

Comparing the developed method with patterned fibers structures with steering electrodes charged with a defined voltage signal, a significant progress in making electrospinning a more controllable process could be reported. Besides, the new method was advantageous because of its flexibility to fabricate difference size and shape of fibers pattern. Both one dimensional fibers alignment and two dimensional fibers patterning were achieved.

Lacking flexibility in the fibers orientation was the disadvantage of most fibers alignment and patterning methods reported in the past. E.g. the collection of electrospun fibers on a rotating collector resulted in a one-directional fibers orientation. Researchers have added auxiliary electrodes (Wu et al., 2007) and knife-edged electrodes bars as electrodes

(Teo et al., 2005) to the rotating drum as collector in order to enhance the controllability effect, but only membrane with orientation into one direction could be fabricated. Besides, sharpened electrodes were used as collector in order to enhance the one directional fibers alignment (Secasanu et al., 2009).

Besides, one dimensional fibers orientation was attained with two separate collector electrodes. Due to its instability, the polymer jet was moving between the two collector electrode and fibers were stretched and therefore aligned between the two collector electrodes (Ishii et al., 2009; Kim, 2006; Kim and Kim, 2006; Lee et al., 2007; Yan et al., 2009; Zhang et al., 2008). However this method showed limitations considering its flexibility. The fibers could only be oriented into one direction. In addition, the length of fibers alignment was small in some studies. Kim and Kim (2006) reported a collector electrode length and therefore length of alignment of only 0.5 mm. Others achieved longer one directional alignment than reported in this thesis. E.g. Yan et al. (2009) used two parallel collector electrodes. The aligned fibers with a length of ~70 mm were deposited on dielectric plate.

Attempts for two dimensional fibers deposition control applied patterned electrodes in order to achieve multidirectional fibers deposition. Collector electrodes with ring, rectangular, triangular cut outs allowed the collection of fibers with triangular or aligned fibers pattern (Kim and Kim, 2006; Li et al., 2005; Zhang et al., 2008). However, a new collector had to be designed for every attempt and the achieved pattern sizes were small with 1 mm (Li et al., 2005) for triangular cut outs. Kim and Kim (2006) reported the alignment of fibers in two dimensions on a length of ~10 mm with a ring electrode as collector charged and discharged with an alternating current (AC) high voltage power supply, however no defined two dimensional fibers patterns could be fabricated with this method.

With close distance electrospinning, very flexible operation was possible, however it was challenging to fabricate a uniform fibers membrane. Besides, the fibers diameter was affected by (Hellmann et al., 2009).

Two approaches with similar basic idea as used in this thesis have been reported. Acharya et al. (2008) introduced one pair of positively charged steering electrodes applied perpendicular to the primary electrostatic field. One dimensional fibers alignment over a length of 10 mm was achieved. Bellan et al. (2006) studied the two dimensional control of the electrospinning polymer jet. With the help of a circular steering electrodes system consisting of four electrodes elements with time varying electric field, control in two dimensions over a width of 1 mm was reported (Bellan and Craighead, 2009). These approaches were advanced in this study by gaining both one and two dimensional control over the polymer jet and by the fabrication of larger fibers patterns.

Besides the fibers structure, a change of fibers morphology to buckling fibers structure was observed in this study, when steering electrodes were applied. Han et al. (2007) have already found buckling fibers structure when depositing fibers on a moving collector. However, for the first time the potential of this fibers morphology regarding its impact on the mechanical properties of the fibrous membrane was investigated in that study.

An E-modulus of ~ 1 MPa was achieved for wave and square structured fibrous membranes after DMEM exposure. Comparing this value with E-modulus of random PLACL fibers, a decrease from ~ 19 MPa to ~ 1 MPa could be reported within this thesis on the basis of structural modifications of fibers membranes. Compared with the aim of the project to achieve an E-modulus similar to that of cardiac tissue either at the beginning or at the end of a diastole, an E-modulus 0.2-0.5 MPa was the target for the scaffold. In order to attain this aim, for future work the used material was suggested to be replaced by more

elastic biomaterial than PLACL. One option is to use the biodegradable elastomer PGS (Poly(glycerol sebacate)) for cardiac tissue engineering (Chen et al., 2008).

The tensile strength of the developed membranes and the risk of implant failure were found to be not critical. The tensile strength of the random, wave and square fibers patterns was multiple times higher than the tensile strength of human cardiac tissue (0.003-0.015 MPa).

In the contrary to fibers aligned on the rotating drum as collector, the wave and square patterned membranes with buckling structure have similar mechanical properties in all directions. Fibers aligned on the rotating drum showed very high stiffness and tensile strength in fibers direction, but very elastic behavior and low tensile strength for the direction perpendicular to the fibers. As in the heart tissue, the muscle was exposed to multidirectional forces due to its helix structure, strongly anisotropic membrane properties were not desirable for the scaffold (Appendix 1).

It was shown by growing CMs on random PLACL fibers structure and PLACL wave fibers structure with buckling morphology that the patterned fibers were beneficial for cardiac tissue engineering. As expected on the basis of the wettability measurement (Chapter 4.2.2), plasma treatment significantly enhanced the cell adhesion and proliferation of CMs. The morphology of the CMs was normal, however the number of CMs growing on the fibers has to be enhanced. Options to enhance their growth are to add natural ECM proteins like e.g. collagen to the polymer because collagen improves the cell adhesion but also weakens the mechanical strength of the fibers (Ananta et al., 2009; Prabhakaran et al., 2009). Due to the slow growth of CMs, longer cell culture periods might be an option to achieve more cells on the fibrous scaffolds. However, longer cell culturing resulted in further degradation of the polymer and therefore might decrease the tensile strength of the fibrous scaffolds. This could

be a critical aspect because the risk of an implant failure after implantation would be enhanced with longer cell culture time.

5 Controllability of electrospaying

Besides the controllability of electrospinning, the controllability of electrospaying was investigated within this thesis. Controllability of electrospaying was studied by using conductive nanostructured materials as collector. As such, a polyethylene oxide (PEO) polymer blend was used for electrospinning of fibers because PEO fibers have been shown to prove good long time filter performance (Patanaik et al., 2010).

5.1 Experimental details

5.1.1 Materials

Polyethylene oxide (PEO) (M_w ca. 100 000) (Figure 33), polyaniline (PANi) (emeraldine base ; M_w ca. 65,000) (Figure 33), (\pm)-camphor-10-sulfonic acid (β) CSA (Figure 33), poly(vinyl chloride) (PVC), N,N-dimethylformamide (DMF) and methanol (ACS reagent, $\geq 99.8\%$) were purchased from Sigma-Aldrich, Germany and used without any further purification. Chloroform (Merck, Germany), tetrahydrofuran (THF) (Merck, Germany), diethyl ether (Fisher Scientific Ltd., UK), heptane (Fisher Scientific, UK) and 2-chloroethyl phenyl sulfide (CEPS) (purity 98%, Sigma-Altrich, USA) were used as received. TiO₂ P25 nanopowder of mean surface area 50 m² kg⁻¹ (Degussa, Germany) was used for the study. 3(trimethoxysilyl) propyl (MEMO) (Degussa, Germany) was used as the stabilizer.

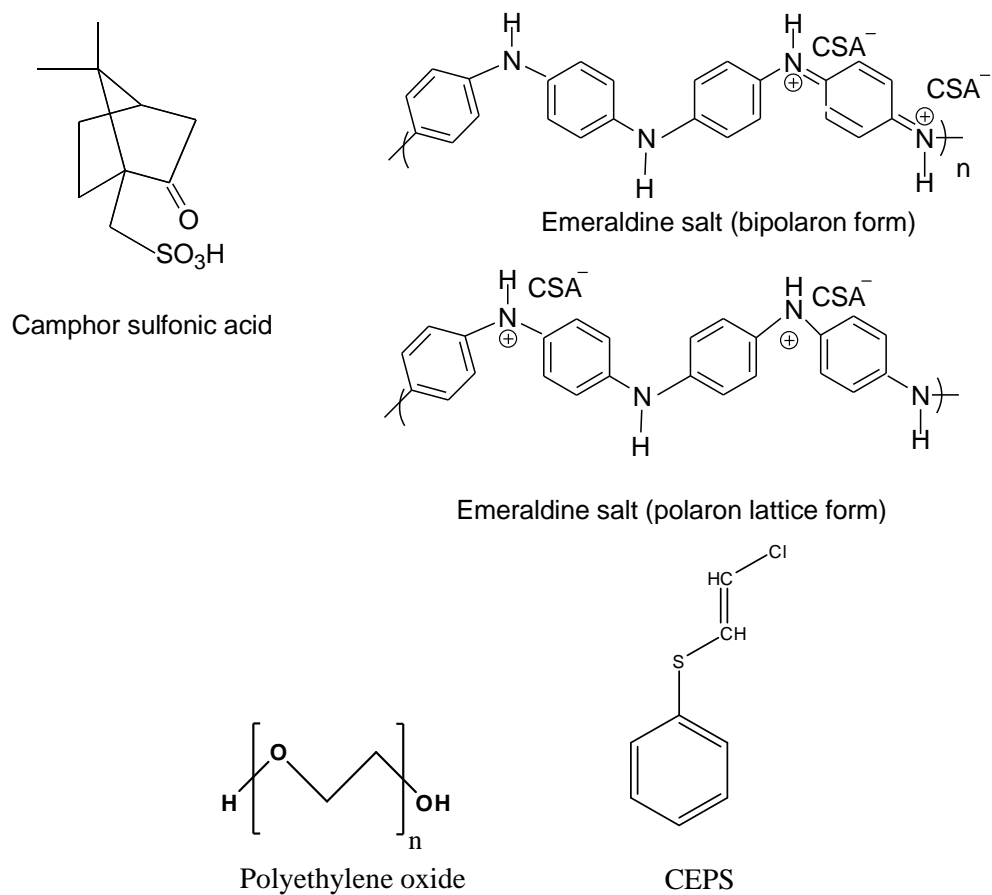


Figure 33. Structure of polymers and dopant used in this study.

5.1.2 Membrane fabrication

All experiments were carried out at room temperature. Different compositions of CSA doped PANi-PEO were prepared as shown in Table 15.

Table 15. Composition of electrospun CSA/PANi-PEO solutions.

	Solution A	Solution B	Solution C	Solution D
PANi	0.05 g	0.10 g	0.15 g	0.20 g
CSA	0.05 g	0.10 g	0.15 g	0.20 g
Chloroform	7.7 g	7.7 g	7.7 g	7.7 g
PEO	0.85 g	0.80 g	0.79 g	0.80 g
PANi concentration	6.0%	12.0%	19.0%	25.0%

The procedure used to prepare the 6, 12, 19 and 25% (w/w) was the following; the required quantity of PANi was first doped using CSA dissolved in chloroform. After filtering the solution with an syringe filter unit (Acrodisc, 0.2 μm Supor Membrane, UK), the PEO was added and stirred for 24 h.

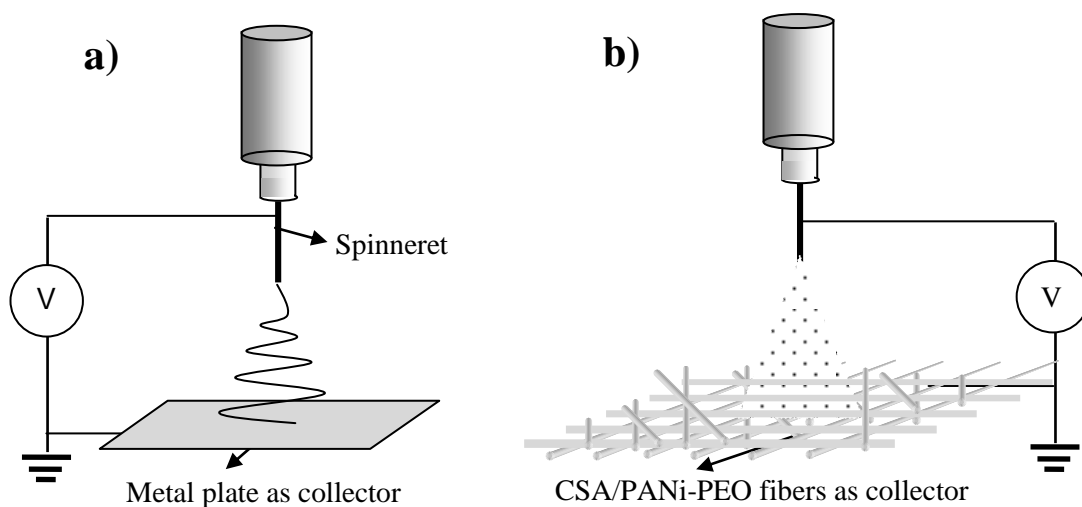


Figure 34. Setup for a) electrospinning, and b) electrospaying.

The as-prepared CSA/PANi-PEO solution were electrospun into fibers by setting the distance between spinneret and collector at 10 cm, solution flow rate at 0.8 ml/h, voltage at 13 kV and humidity at 30- 40% (Figure 34a). To prepare the PVC fibers, 0.3 g of PVC was first dissolved in the solution that contains 1.5 ml DMF and 1.5 ml THF, and then stirred for 24 h. The resultant solution was electrospun into PVC fibers by maintaining the spinneret and collector distance at 10 cm, flow rate at 1 ml/h, at 10 kV and humidity of 70% (Figure 34a). 5% (w/v) of TiO₂ NPs solution was prepared in methanol. The suspension was sonicated using a high intensity ultrasonic liquid processor (VCX 500 Sonic) at 30% intensity for 1 h. 0.25 g of MEMO was added into the solution and further sonicated for 180 s. As-prepared TiO₂ NPs solution was electrospayed by keeping the distance between spinneret and PANi-PEO fibrous membrane collector at 8 cm, flow rate of 0.3 ml/h and at 10 kV. During electrospaying, the conductive CSA/PANi-PEO fibrous membrane was laid on polyethylene (PE), and grounded (Figure 34b).

5.2 Results

5.2.1 CSA doped PANi-PEO fibers

The morphology of CSA/PANi-PEO fibers obtained at different weight % was investigated under SEM. PEO blended with 6% and 12% CSA/PANi yielded uniform and defect-free fibers (Figure 35a and Figure 35b) whereas 19% CSA/PANi-PEO showed irregularities in its fibers structure and beads (Figure 35c).

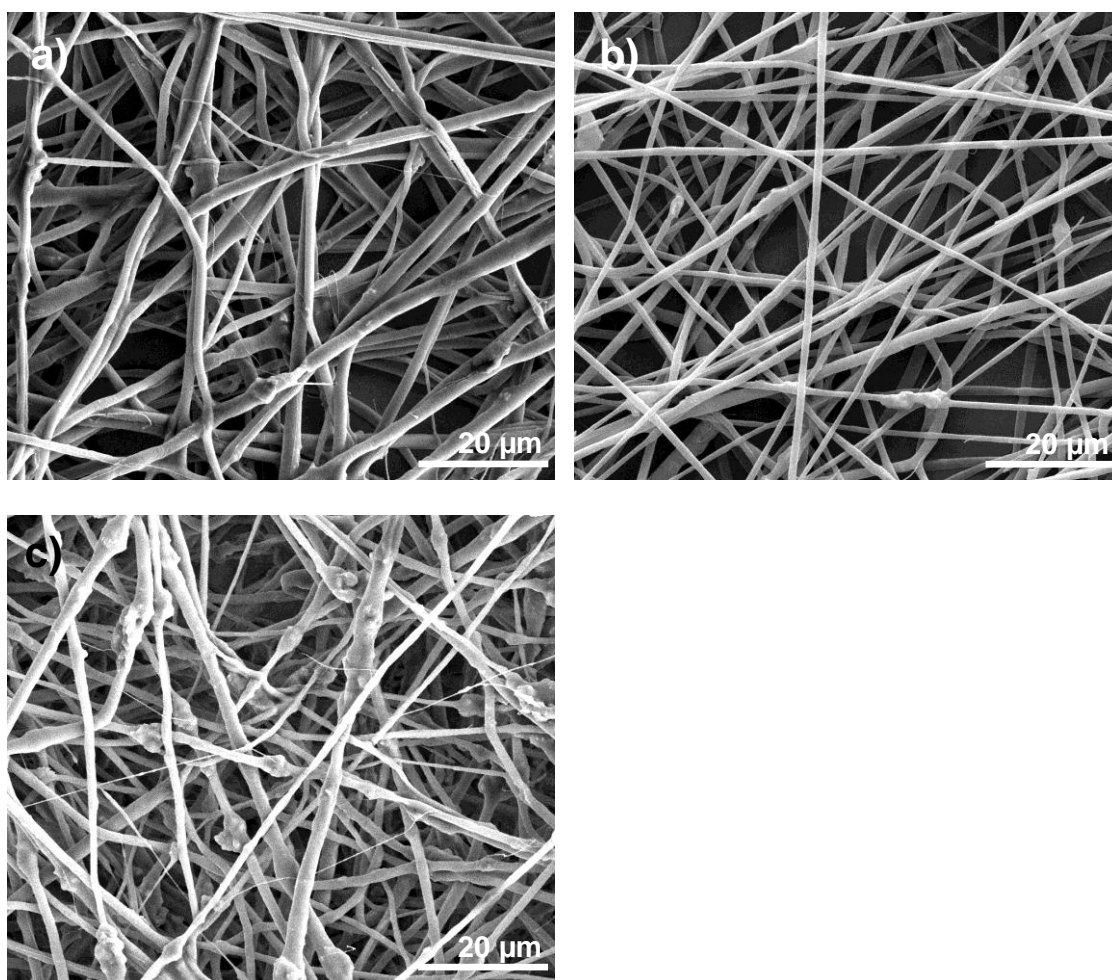


Figure 35. PEO fibers with a) 6% PANi concentration, b) 12% PANi concentration, and c) 19% PANi concentration.

The average diameters of 6% and 12% CSA/PANi-PEO fibers were 995 ± 184 nm and 987 ± 179 nm respectively but the 19% CSA/PANi-PEO fibers had an average fibers diameter of 997 ± 236 nm. The SEM analysis concluded that 6% and 12% PANi were ideal for preparing the catalytic membrane.

As high-voltage was applied between the spinneret tip and the grounded collector, fibers were attracted due to the conductive nature of metal collector. Conductive property of the as-prepared 6%, 12% and 19% PANi-PEO fibrous membranes of same thickness (~ 80 μm) was measured using I-V analysis (Figure 36).

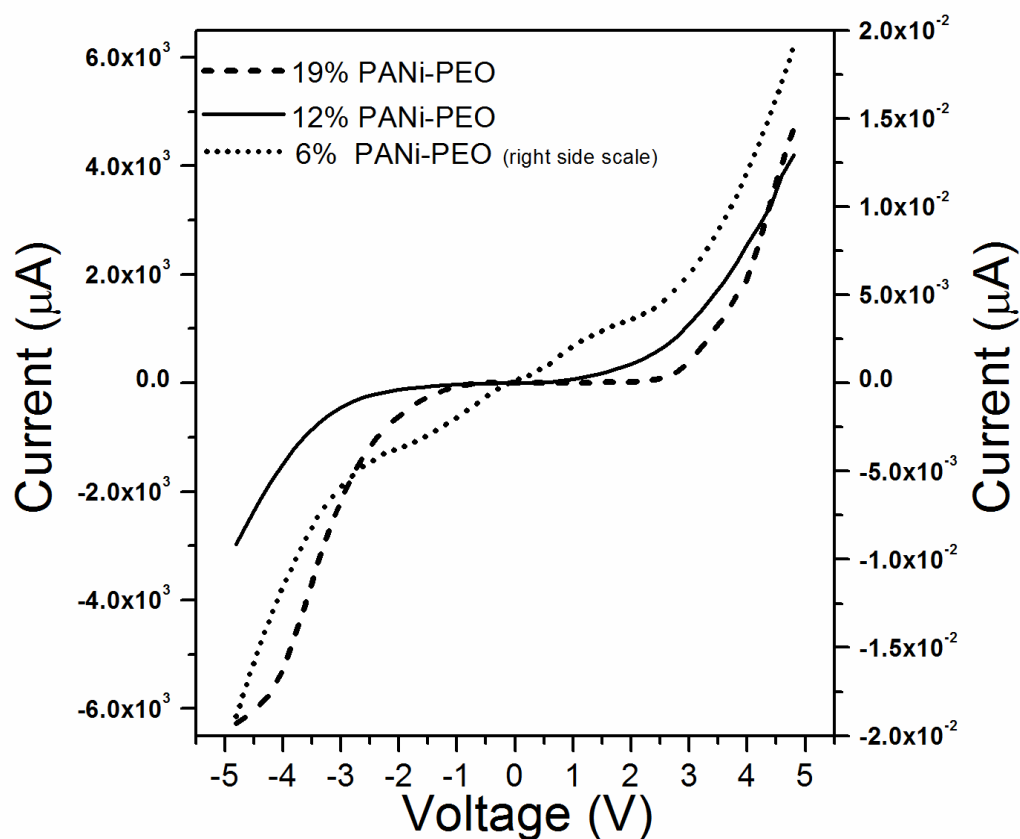


Figure 36. I-V curves of PEO fibers with a) 6% PANi concentration, b) 12% PANi concentration, and c) 19% PANi concentration.

The 6% PANi concentration in PEO resulted in nA current range, which is about five orders of magnitude smaller than that of 12% and 19%. A similar conductivity trend was reported for CSA/PANi-PEO fibers with varying PANi concentration by Norris et al. (2000). For 12% of PANi, the recorded current was approximately in the same mA range as 19% PANi composition in spite of the expected increase of the conductivity due to higher PANi concentration. This could be due to the morphological defects of 19% PANi fibers. The 19% PANi yielded beads and broken fibers (Figure 35c), which could dampen the current transport in the fibers. The I-V studies on 6%, 12% and 19% PANi-PEO fibers suggested that the 12% PANi could be the critical composition to prepare the fibers as collector.

5.2.2 Effect of collectors on the adhesion of TiO₂ nanoparticles

In classical electrospinning and electrospaying setups, metal usually aluminum foil has been used as the collector due to its conductive nature. The PANi-PEO solution was first electrospun into fibers and grounded with aluminum foil underneath. Electrospaying of TiO₂ NPs did not result in uniform coating over the fibers. TiO₂ NPs were found to be agglomerated on the fibers and the agglomeration was significant at 12% and 19% PANi, which would cause pores blockage, and thus larger pressure drop.

The experimental setup was modified such that the collected electrospun PANi-PEO fibrous membrane was placed on the polyethylene, an insulator, and was directly grounded. It established PANi-PEO fibers as the collector due to its conductive nature, maximum adsorption of electrospayed TiO₂ NPs on the surface of the fibers was achieved.

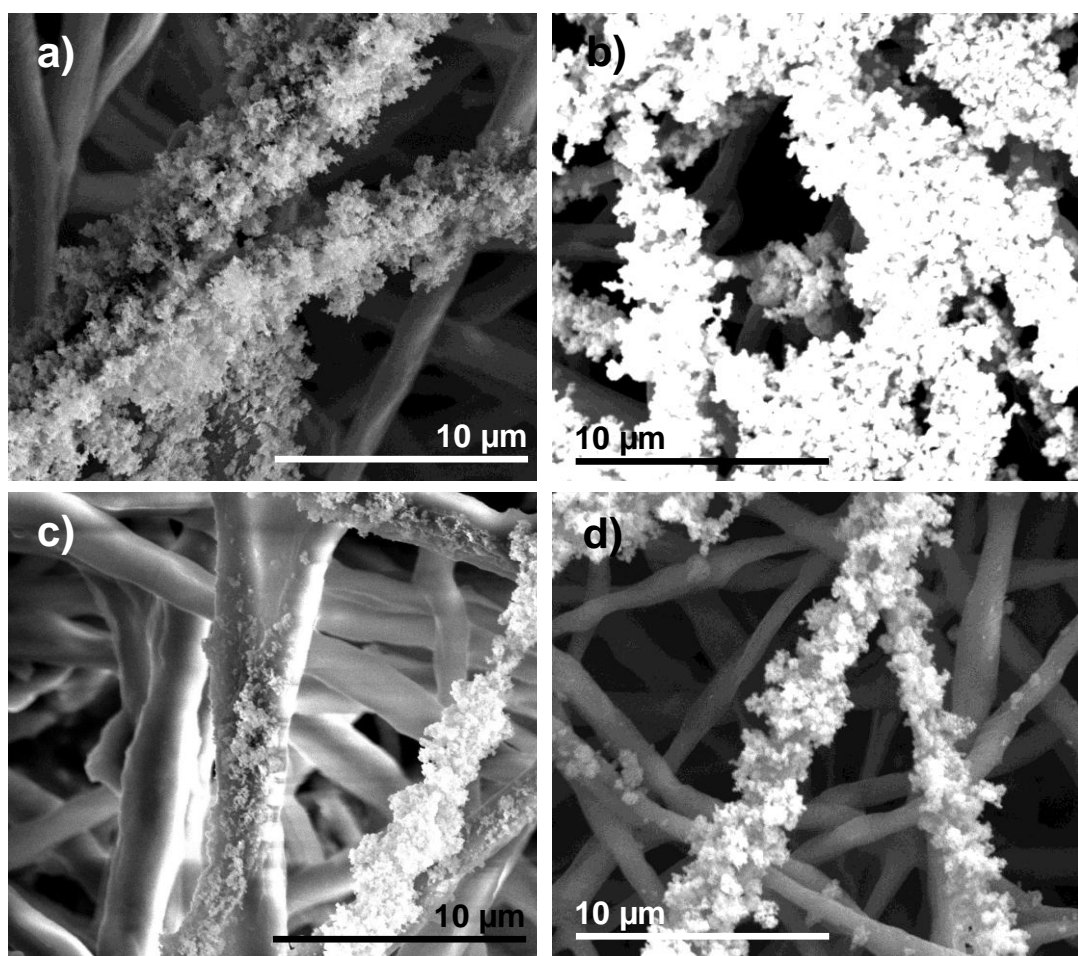


Figure 37. PANi-PEO fibers a) 6% of PANi and aluminum foil as the collector, b) 12% of PANi and aluminum foil as the collector, c) 6% of PANi collected without aluminium foil, and d) 12% of PANi collected without aluminum foil.

It also assisted to obtain the uniform dispersion of TiO₂ NPs over the PANi-PEO fibers (Figure 37). As seen in SEM picture (Figure 37c), 6% PANi-PEO fibers showed substantially lesser TiO₂ NPs on the fibers than that of 12% PANi-PEO (Figure 37d). It indicated that the higher fibrous membrane conductivity resulted in better and more uniform dispersion of TiO₂ NPs on the fibers.

The TiO₂ NPs were found as aggregates on the fibers when aluminum foil was used as the collector, which could be explained as follows; electric fields created by both conductive

PANi-PEO fibers and aluminum foil could be interfered. Due to such interference of electric fields between the spinneret tip and the fibers as well as the aluminum, the TiO₂ NPs deposition not only occurred on the fibers, but also within the pores of fibrous membrane (Figure 37a and Figure 37b).

To investigate the influence of the electric field interference on the adsorption of TiO₂ NPs, non-conductive PVC fibrous membrane was used as collector. PVC was electrospun to fabricate fibrous membrane using DMF/THF at 50/50% (w/w) solvent mixture (Figure 38), and placed on grounded aluminum foil. For comparison purpose, another PVC fibrous membrane was prepared, dried for overnight and used as collector for electrospayed TiO₂ NPs.

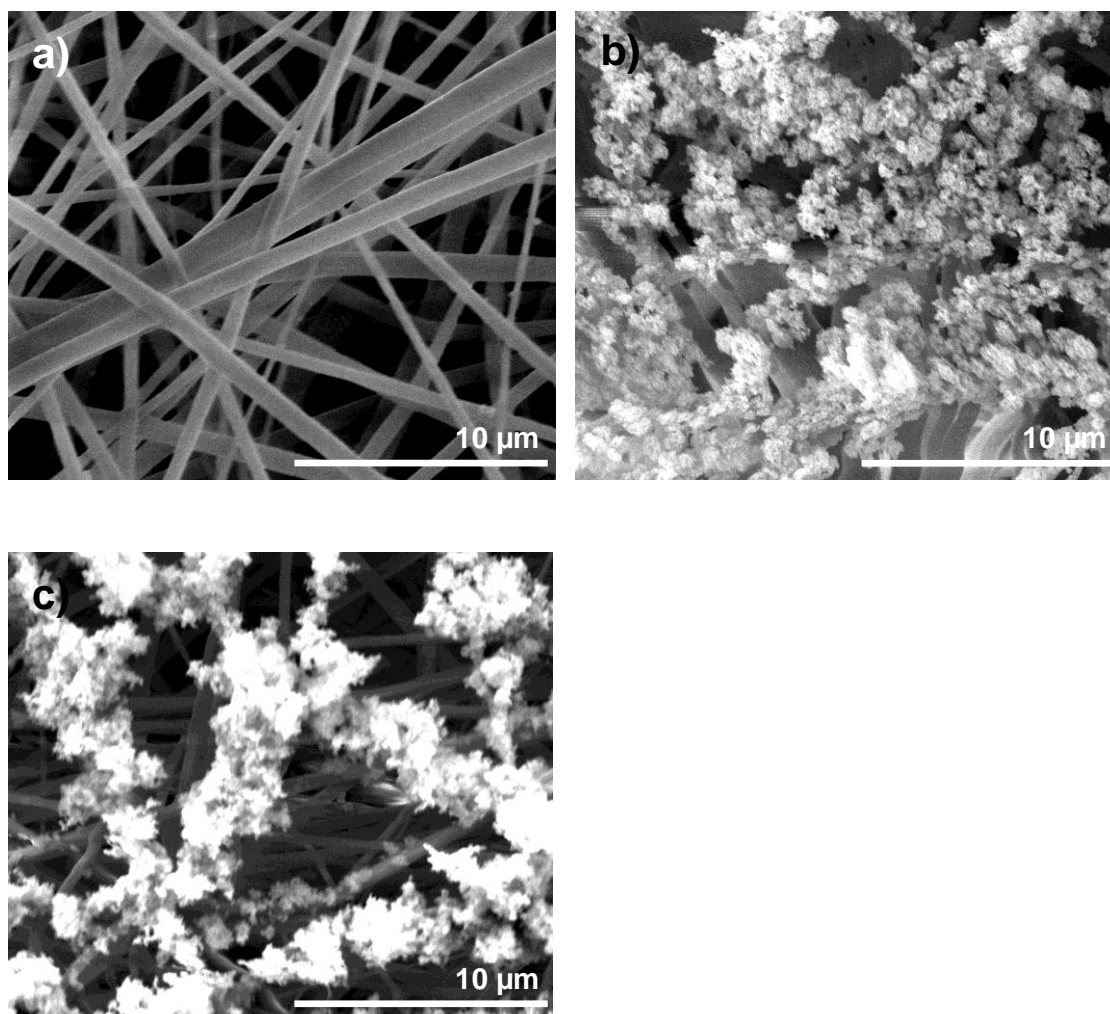


Figure 38. Grounded PVC fibers a) without DMF/THF residual and without aluminum foil, b) with DMF/THF residuals and with aluminum foil, and c) with DMF/THF residuals and without aluminum foil.

Investigation under SEM showed that there were no TiO_2 NPs adsorption on the dried PVC fibers (Figure 38a), whereas in the PVC fibers with residual DMF/THF solvent the TiO_2 NPs were found to be adhered (Figure 38b and Figure 38c). The presence of DMF solvent imparted the conductiveness to the PVC fibers, thus TiO_2 NPs were attracted on the PVC fibers. This conveys that the conductive nature of fibers played a dominant role in the adsorption of TiO_2 NPs on the fibers. The electrospun PVC fibers used with residual solvent

and without aluminum foil (Figure 38c) allowed the dispersion of TiO₂ NPs to be more uniform and lesser agglomeration.

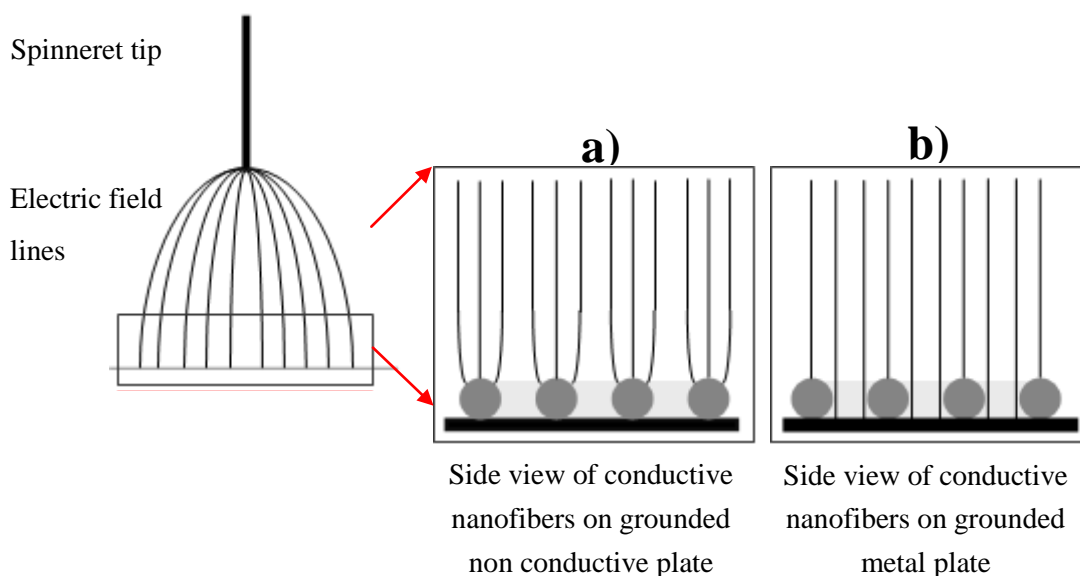


Figure 39. Schematic explanation on the electric field distribution between the spinneret tip and conductive PANi-PEO fibers in the presence of a) no aluminum foil beneath, and b) with aluminum foil.

This study confirms that the electric field interference from the conductive collector and the conductive fibers led for agglomeration of electrospayed TiO₂ NPs, which is not preferred for making catalytic filter membranes. Due to the undisturbed electric field distribution near the PANi-PEO fibers collector, the absence of aluminum collector (Figure 37d and 38a) offered the possibility to deposit TiO₂ NPs exclusively on the fibers. The presence of aluminum as collector (Figure 37b and 8b) for 12% PANi-PEO fibers caused blockage because of the interference of electric fields of the conducting fibrous membrane and the aluminum foil collector placed underneath. The binding strength of TiO₂ NPs onto the fibers was examined by sonication at 20% intensity level in diethyl ether medium using

ultrasonic liquid processor. It was found that the TiO₂ NPs retained its adhesion onto the PANi-PEO fibers (Figure 40).

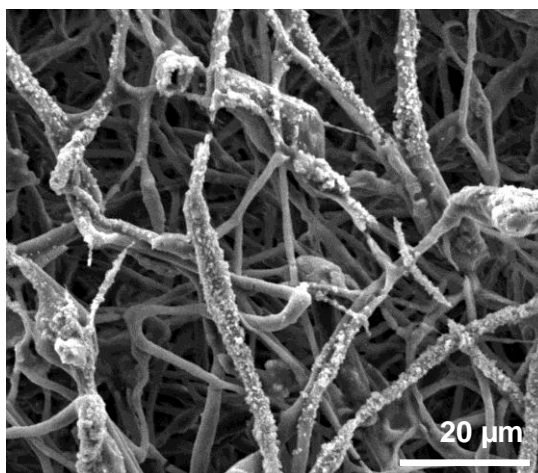


Figure 40. SEM image of 12.5% PANi-PEO fibers coated with TiO₂ nanoparticles (5 min of deposition) followed by sonication of the membrane.

5.2.3 Catalytic performance of TiO₂-PANi-PEO fibrous membrane

To estimate the catalytic activity of the membranes, 100 mg of TiO₂ embedded PANi-PEO membrane was introduced into the 10 ml solution prepared with CEPS in heptane at concentration of 0.05% (v/v). Then the membrane samples were exposed to UV light for 10 min and 60 min. The ultraviolet (UV) absorption spectrum of CEPS solution (Figure 41) showed two big peaks at 220 nm and 250 nm.

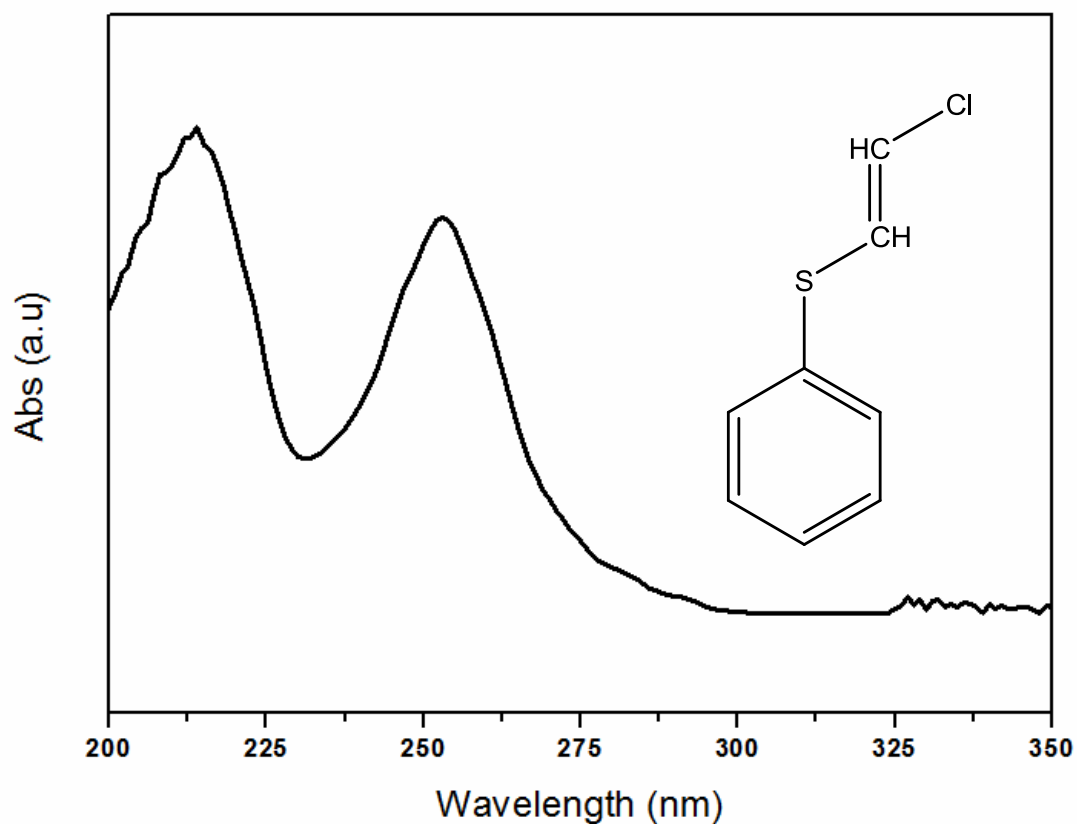


Figure 41. UV spectrum of CEPS in heptane at concentration of 0.05% (v/v).

TiO₂ being the photo-catalyst produces the active oxygen species under UV irradiation, which should decompose CEPS. The photolytic degradation of CEPS in the presence of TiO₂ NPs embedded PANi-PEO fibrous membrane was studied by measuring the absorbance decay at 220 nm.

6% TiO₂-PANi-PEO fibrous membrane was introduced into the 10 ml of CEPS solution and irradiated with UV light in a closed chamber for 10 min. 1 ml of UV irradiated CEPS solution was taken into quartz cuvette and its absorbance at 220 nm in the UV spectrophotometer was measured. The experiment was repeated for the 12% TiO₂-PANi-PEO fibrous membrane as well. The photo-catalytic decomposition of CEPS was correlated with the decrease in the absorbance of CEPS at 220 nm and plotted as shown in Figure 42.

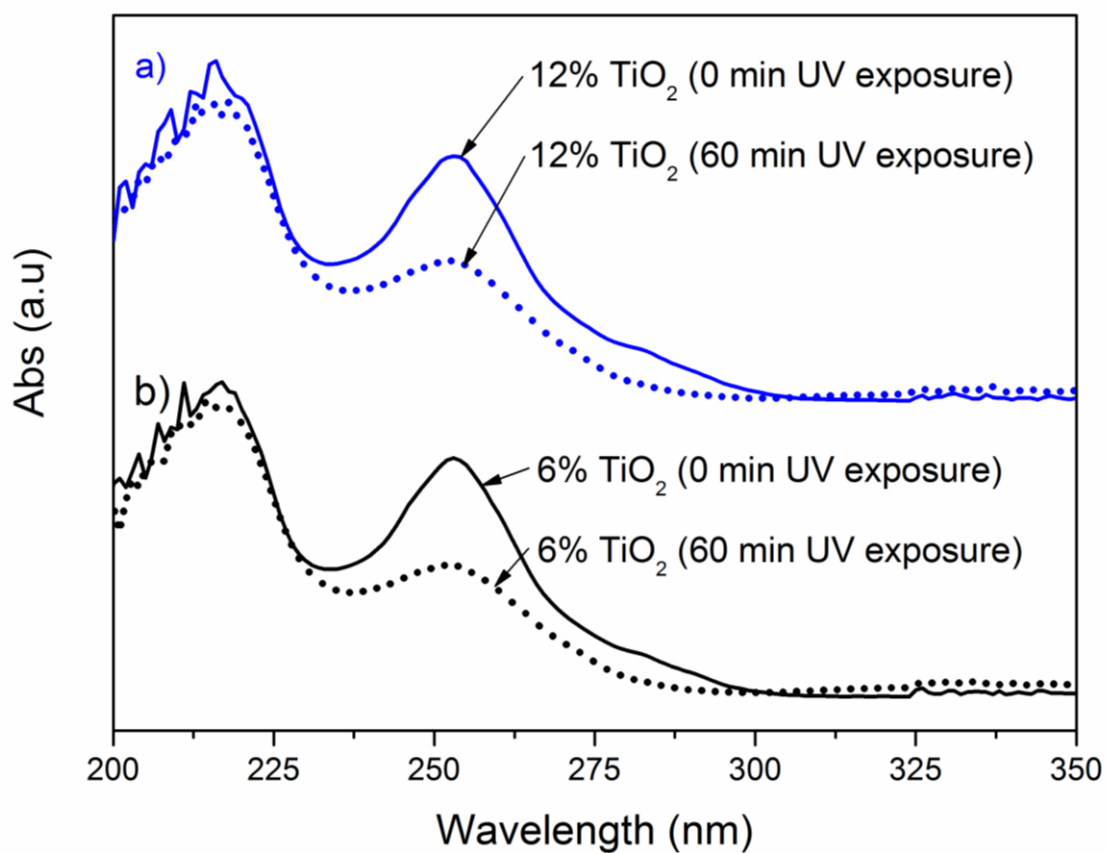


Figure 42. UV spectra for a) 6% TiO₂-PANi-PEO membranes after 0 min and 60 min UV light exposure, and b) 12% TiO₂-PANi-PEO membranes after 0 min and 60 min UV light exposure.

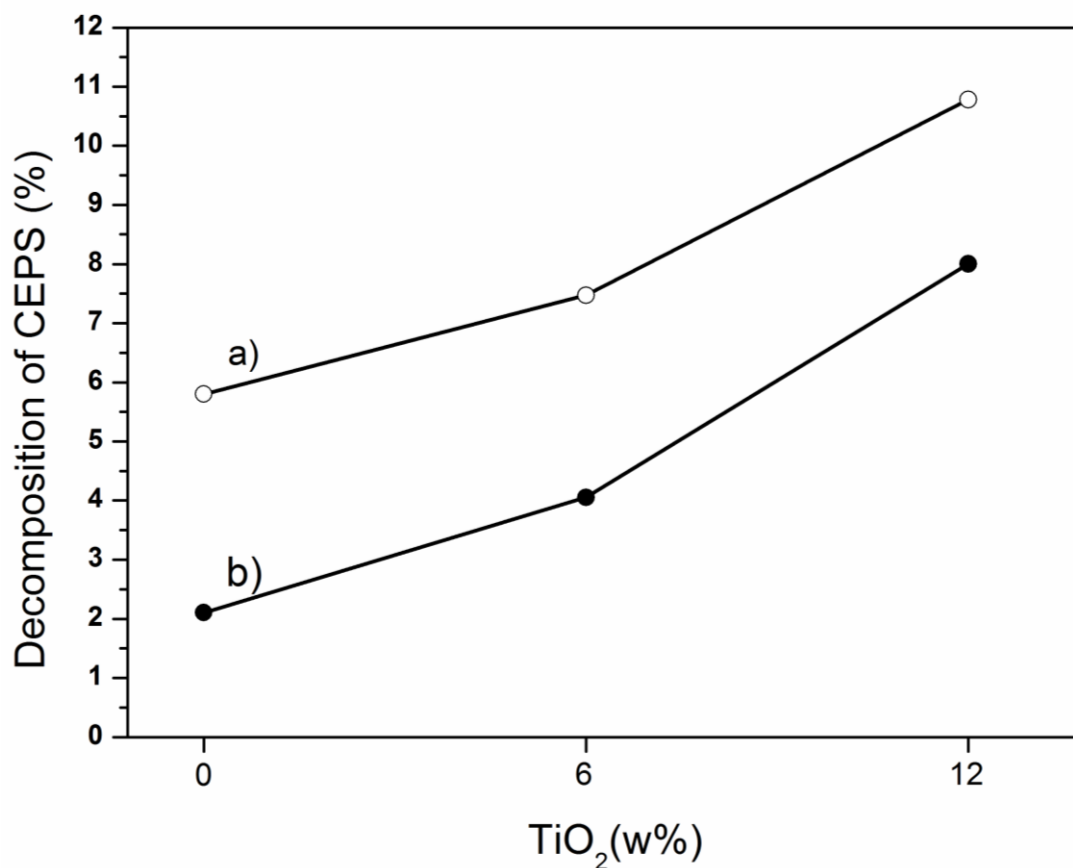


Figure 43. Photocatalytic decomposition of CEPS with respect to reaction time and TiO₂ quantity a), after 60 min UV light exposure, and b) 10 min UV light exposure.

In Figure 42 and Figure 43, it is clear that the higher quantity of TiO₂ decomposed the CEPS significantly. The catalytic activity was also investigated for 60 min UV exposure time. It was observed that the higher concentration of TiO₂ decreased the absorbance of CEPS especially, the second shoulder that exists at 250 nm tremendously after 1 h, which could be the result of the formation of adduct product (Figure 42 and Figure 44).

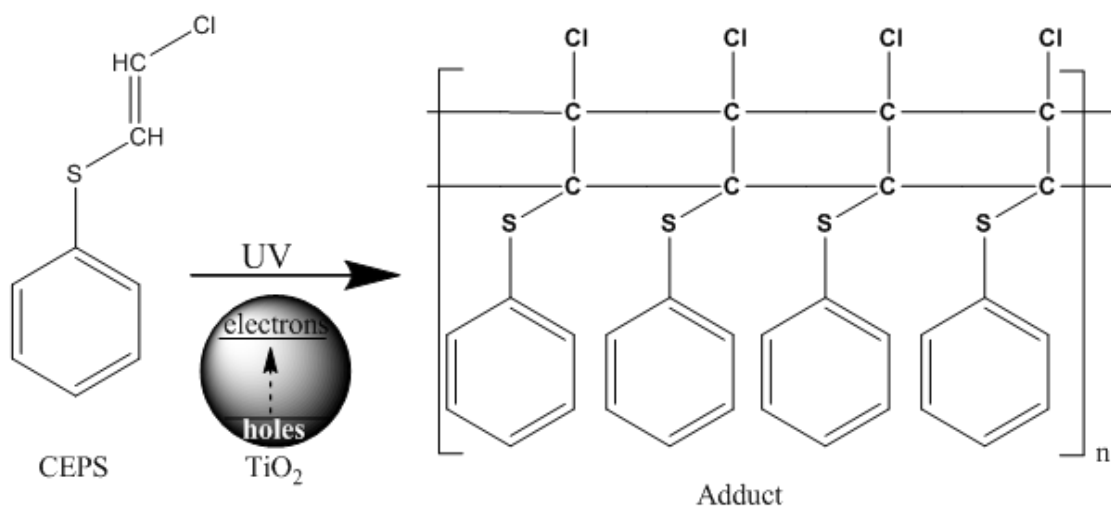


Figure 44. Proposed photocatalytic action of TiO_2 nanoparticles towards CEPS under UV environment.

TiO_2 produces the radical under irradiation of ultraviolet light that could allow the polymerization of decomposed CEPS and resulted in the formation adducts compound. In our study the greater dispersion and uniform coating of TiO_2 NPs made the PANi-PEO fibrous membrane to reduce the CEPS into 11% with only 12% (w/w) of TiO_2 NPs (Figure 43).

5.3 Discussion

Roso et al. (2008) has already reported an attempt to combine both the electrospinning and electrospraying and prepared the TiO_2 nano-catalysts embedded polysulfone (PSU) fibers by simultaneous spinning and spraying. However, the catalyts agglomeration was severe in this method, which in turn limited the performance of the nano-catalytic filters. In addition, the catalyst nanoparticles were not uniformly dispersed over the fibers that let the fibrous catalyst membrane not fully and potentially realized. Furthermore, this method led to more materials wastage. Therefore, Roso et al. (2008) obtained 11% decomposition of CEPS

using the 32% (w/w) of TiO₂ NPs adsorbed fibers, in comparison to 11% decomposition with only 12% (w/w) of TiO₂ NPs in this thesis. This study clearly highlights that effective dispersion of the nanocatalysts on the fibrous filter membrane is more important than the quantity of catalysts in improving the catalytic activity.

Besides, Sundarrajan et al. (2007) blended the polymer with magnesium oxide (MgO) nanocatalysts and electrospun into fibers. This method however resulted in relatively poor catalytic performance because most of the catalyst nanoparticles were covered up inside the polymer fibers. In another study, nanocatalysts were adsorbed on polymer fibrous membrane by liquid phase deposition (LPD) (Drew et al., 2003), nevertheless this method required the tedious selection of solvents.

Therefore, an advance of catalytic filtration membranes fabricated with a combination of electrospinning and electrospaying could be reported within this thesis.

However, electrospinning and electrospaying various other techniques have been explored to impregnate the catalysts onto the filtering membranes. E.g. Rojas-Chapana et al. (2005) prepared the catalytic filter membrane using an adhesive layer onto the polymer to adsorb the titanium dioxide (TiO₂) nanocatalysts, whereas Fujiwara et al. (Fujiwara et al., 2007) used ion exchange process, followed by precipitation process to immobilize the manganese oxide (MnO) nanoparticles.

Finally various aspects like e.g. the catalytic performance, the adhesion of the TiO₂ NPs to substrate and therefore its safe application as well as the fabrication cost will determine the success of the different applications on the market.

6 Conclusions and future perspectives

In this study, controllability of electrospinning has been developed. Focused fibers deposition on the basis of the polymers Nylon, PCL, PLACL and PVC was achieved. Both fibers spot sizes with a diameter of 3-4 mm and fibers stripes with a width of ~0.15 mm were achieved. In addition, the fabrication of wave, square and circular PLACL fibers patterns by electrospinning over a width of at the maximum ~33 mm could be reported. With these very determinable fibers structures, it was shown that the mechanical properties of the fibrous membrane could be controlled. Furthermore, the patterned fibers with buckling morphology were identified as a central element in order to enhance the elasticity of fibrous membranes.

Besides electrospinning, deposition of electrospayed nanodroplets could be controlled by the structure and size of the collector. The positively charged dispersed nanodroplets were collected exclusively on the grounded conductive fibers.

Comparing the controllability of electrospinning and electrospaying, electrospaying could be easily controlled by adapting the collector structure. The reason therefore was good attraction of the light and electrically charged nanodroplets dispersed by electrospaying.

Owed to the inertia of the polymer fibers, focusing of electrospinning by minimization of the collector did not result in high precision of the fibers deposition with a fibers spot size of 10 mm at the minimum. Instead, big efforts had to be made to focus electrospinning with electrostatic lens systems and with steering electrodes introducing an additional electric field into the electrospinning process in order to control fibers deposition.

Future work could contain the transfer of the developed methods to a wider range of polymers and ceramics.

In addition, further testing have to be performed with the developed nanostructures both for cardiac tissue engineering and for catalytic filtration. The stability of elastic fibers structures for cardiac tissue engineering has to be investigated for long term application to prevent risk to human health. It will have to undergo dynamic long term testing to avoid their failure after implantation into the human body because a human heart muscle contracts about ten million times per year. In the first step, this step can be done in a bioreactor modeling the real conditions within a human body. In the second step, these results have to be confirmed in animal trials. Besides, the number of CMs growth on the fibers has to be enhanced, e.g. by changing the chemical composition of the fibers or by using different cells.

Besides, health aspects have to be taken into consideration for the application of the catalytic filtration membrane. Although good adhesion of the TiO₂ nanoparticles to the electrospinning of ceramic nanoparticles solutions was proven, further tests have to be done to avoid any debonding of TiO₂ nanoparticles. This has highest relevance in order to be able to transfer the product to the market because TiO₂ nanoparticles increase the risk of cancer when breathed in.

Reflecting on the research presented in this study, substantial advances of both electrospinning and electrospaying could be reported. However, until the intended product reaches the market, some challenges are still to solve by future researchers.

Appendix 1

Heart failure is one of the leading causes of death in industrialized countries and is expected to become a global epidemic within the 21st century all over the world. The estimated figures are 5 million Americans, 1.8 million Britons and 25 million people worldwide suffering from heart failure, with approximately 550 000 and 120000 new cases diagnosed each year in the United States (US) and the United Kingdom (UK) respectively [http://www.acornvc.com/patients_families/heart_failure.cfm, 2010]. A challenge with heart diseases like e.g. the myocardial infarction is the high patients mortality rate of 40% within 12 months after the diagnosis, and a 10% annual mortality rate for the following years (Cowie et al., 2000).

Besides, the economic relevance of heart diseases in industrialized countries reaching more than \$33 billion in the US and more than 700 million in the UK annually have to be taken into consideration [http://www.acornvc.com/patients_families/heart_failure.cfm, 2010]. Both humanitarian and economic aspects motivate the development of repair mechanism to cure heart diseases.

The most common cause of left-sided cardiac tissue failure is isochemic heart disease also known as coronary artery disease with an episode of acute myocardial infarction.

It is well recognized that left ventricular dilatation is a precursor of ventricular dysfunction and congestive heart failure after myocardial infarction. The damaged left ventricle undergoes progressive “remodeling” and chamber dilation with myocyte slippage and fibroblast proliferation. The damage of the heart wall muscle is permanent because the myocardial tissue lacks significant intrinsic regenerative capability to replace the lost cells after a massive cell loss due to infarction. The enlargement in ventricular volume leads to progressive structural and functional changes in ventricles, well known as ventricular

remodeling. Ventricular remodeling is compensatory at the initial stages, but adds further inefficiency to the mechanical pumping of the ventricular muscle, predisposing towards the final stage of congestive heart failure (CHF). With CHF, the heart cannot pump sufficient amount of blood to meet the metabolic requirements of the body (Vogel, 2002).

The myocardium collagen matrix mainly consists of type I and III collagens, which form a structural continuum. Synthesized by cardiac fibroblasts, type I and III collagens have different mechanical properties, type I collagen mainly provides rigidity, whereas type III collagen mainly contribute elasticity. The two types of collagens jointly support and tether myocytes to maintain their alignment, whereas their tensile strength and resilience resist their deformation, maintain the shape and thickness, prevent the rupture and contribute to the passive and active stiffness of the myocardium (Chen et al., 2008b).

The heart muscle changes its E-modulus during its contraction. At the beginning of the diastole, the heart muscle is elastic. At the end of the diastole, it becomes stiffer and stiffer. The reported E-modulus of the myocardium at the beginning of the diastole varied depending on the measurement technique. Kanai (Kanai, 2005) measuring the wall vibrations after aortic valve closure and obtained values in the range 24-30 kPa. Rump et al. (Rump et al., 2007) induced external vibrations in conjunction with magnetic resonance imaging (MRI) and obtained values between 5 and 27 kPa. Sack et al. (Sack et al., 2009) using WAV-MRE measures of dynamic relativity elasticity changes obtained elasticity values in range 37.7 ± 10.6 kPa. At the end of the diastole, an E-modulus of 0.2-0.5 MPa was reported (Nagueh et al., 2004; Nakano et al., 1990 ;Watanabe et al., 2006).

The common end point of cardiac diseases is CHF or just heart failure, which is a condition when the heart is not able anymore to pump a sufficient amount of blood into the body because of a partly died myocardium.

Multiple options have been developed in order to recover heart diseases.

First, pharmaceutical therapy aims at the reduction of work load of the heart and the protection from the toxic humoral factors which are overactivated in heart failure (Young et al., 2004).

Second, interventional therapies like e.g. surgery or implantation of pacing devices are widely used to control electrical as well as mechanical asynchrony (Chen et al., 2002; Hawkins et al., 2006; Kohli and Elliott, 2005; Loebe et al., 2003; Martinez et al., 2006).

However, both pharmaceutical and interventional therapies have limitations for application at the end stage of the disease (Packer et al., 2002).

For end-stage heart failure, heart transplantation is the ultimate option. Because of the lack of organ donors and the complications associated with immune suppressive treatment, new options are required to cure spreading heart diseases. Numerous strategies were developed with cardiac tissue engineering.

1) Cardiomyoplasty (active systolic assist)

Preprepared skeletal muscles, which can work at power levels analogous to those of the heart, are wrapped around the heart and thereby improve the pumping power of the heart (Senning and Thorac, 1967; Walsh et al., 2005). However, Food and Drug Administration (FDA) has not approved any of these methods.

2) Cell-based therapy (isolated cell-delivery)

Transplantation of functional cardiac myocytes and improvements of the contractile function were reported (Koh et al., 1993a; Koh et al., 1993b; Soonpaa et al., 1994).

3) Left ventricular restraint (passive diastolic constraint)

4) Scaffold-free cell-sheet implantation

The heart is strengthened with a heart patch (Chen et al., 2008b)

5) Heart patch implantation (passive diastolic constraint and cell delivery)

A man-made heart patch is populated with cells in vitro and implanted afterwards in vivo (Chen et al., 2008c; Eschenhagen et al., 1997; Fujimoto et al., 2007).

In this work, the focus was set on the fabrication of an electrospun heart cardiac patch populated with cells in vitro with later implantation in vivo (Strategy 5) (Figure 45).

The primary functions of cardiac tissue engineering are the cells delivery, and ventricular restraint (Chen et al., 2008a). A scaffold may prevent heart failure by increasing the mechanical strength of the infarct, thereby preventing remodeling and deterioration of the cardiac function in a similar fashion to left ventricular restraints. On the other hand, a too stiff polymer may induce diastolic dysfunction. Therefore, the mechanical properties of the scaffold must be carefully examined. Owing to the helix shape of the cardiac muscle, both the muscle and the applied cardiac patch are exposed to multidimensional forces and therefore complex states of stress (Figure 46). Because of the helix structure of the cardiac muscle, superimposed compressive, torsion and bending forces occur.

Hence, a scaffold with defined anisotropic mechanical properties is required, which meets the requirements of tissue engineering like highly porous structure with large interconnected pores, good wettability, structural stability, biodegradability, and non-immunogenicity (Chapter 1.1).

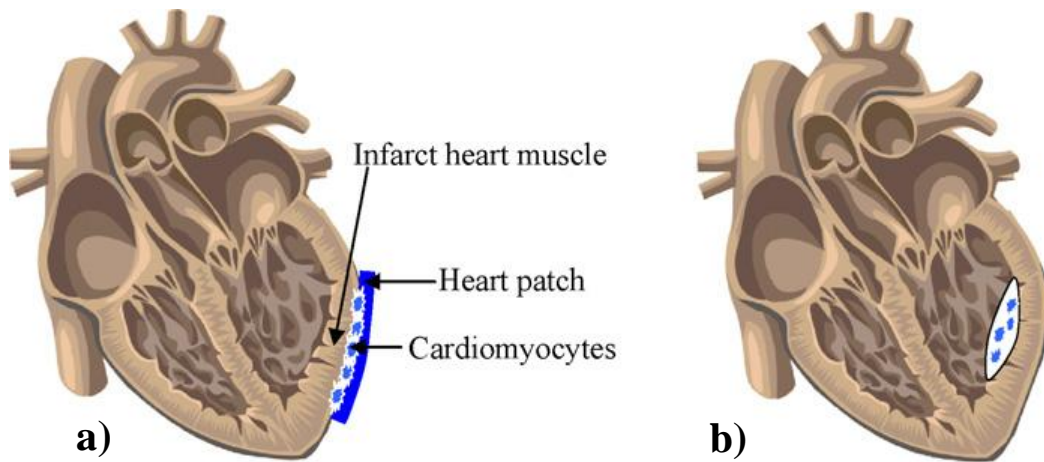


Image from Chen et al., 2008b

Figure 45. Application of the cardiac patch at the heart (Chen et al., 2008b) a) epicardial, and b) endoventricular heart patches.

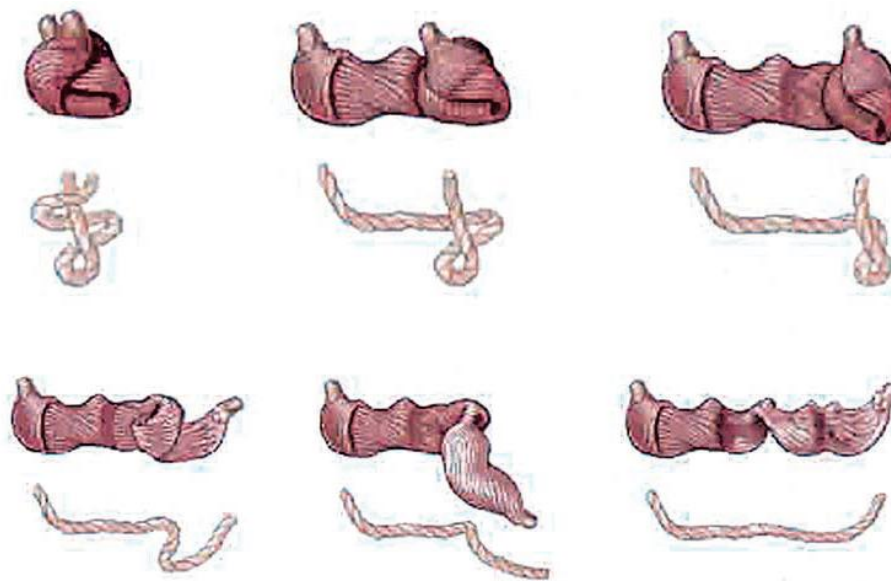


Image from Torrent-Guasp et al., 2001

Figure 46. Helix shape of the heart muscle. Therefore, the state of stress within the heart muscle is complex and multidirectional forces are induced into the muscle (Buckberg, 2002). To demonstrate the complex helix shape of the heart muscle, it is compared with the unfolding of a rope (Torrent-Guasp et al., 2001).

There are two options to approach the required mechanical properties of a scaffold:

- Modification of the applied materials composition of the scaffold.
- Modification of the scaffold structure, like the orientation of electrospun fibers and the fibers morphology.

The scaffold could be fabricated with a variety of very elastic materials with an E-modulus in the range of 10 Pa to 20 kPa, such as fibrin (~50 Pa), Matrigal (30-120 Pa), type I collagen gels (100 Pa to 6 kPa for 1-3 mg/ml), bioactive hydrogels based on N-isopropyl acrylamide (100-400 Pa) and alginate (100 Pa-6 kPa). However, for the very elastic materials lacking tensile strength is an issue to meet the requirements of long term stress.

In this study, the efforts were made to achieve the required mechanical properties of the scaffold by developing methods to determine the fibers structure and morphology by electrospinning and fibers orientation in the scaffold. With PLACL, a comparatively stiff biodegradable polymer was chosen.

Bibliography

Acharya, M., Arumugam, G. K., Heiden, P. A.

Dual Electric Field Induced Alignment of Electrospun Nanofibers.

Macromolecular Materials and Engineering, 293, pp. 666–674. 2008.

http://www.acornv.com/patients_families/heart_failure.cfm (accessed in June 2010)

Ananta, M., Aulin, C. E., Hilborn, J., Aibibu, D., Houis, S., Brown, R. A., Mudera, V.

Poly(Lactic Acid-Co-Caprolactone)–Collagen Hybrid for Tissue Engineering Applications.

Tissue Engineering: Part A, 15 (7). 2009.

Bellan, L. M., Craighead, H. G.

Control of an electrospinning jet using electric focusing and jet-steering fields

Journal of Vacuum Science Technology B, 24 (6). 2006.

Buckberg, G. B.

Basic science review: The helix and the heart.

The Journal of Thoracic and Cardiovascular Surgery, 124 (5). 2002.

Chen, F.Y., Cohn, L.H.

The surgical treatment of heart failure. A new frontier: nontransplant surgical alternatives in heart failure.

Cardiology in Review, 10 (6), pp. 326–333. 2002.

Chen, Q.-Z., Bismarck, A., Hansen, U., Junaid, S., Tran, M. Q., Harding, S. E., Ali, N. N.,

Boccaccini, A. R.

Characterisation of a soft elastomer poly(glycerol sebacate) designed to match the mechanical properties of myocardial tissue.

Biomaterials, 29, pp. 47–57. 2008a.

Chen, Q.-Z., Harding, S. E., Ali, N. N., Lyon, A. R., Boccaccini, A. R.
Biomaterials in cardiac tissue engineering: Ten years of research survey.
Materials Science and Engineering R, 59, pp. 1–37. 2008b.

Chen, Q.Z., Harding, S.E., Ali, N.N., Boccaccini, A.R.
In: Boccaccini, A.R., Gough, J. (Eds.), Tissue Engineering Using Ceramics and Polymers.
Chap 16: Myocardial tissue engineering.
pp. 335-352, Cambridge: Woodhead Publishing Limited. 2008c.

Choi, S. S., Lee, S. G., Im, S. S., Kim, S. H., Joo, Y. L.
Silica nanofibers from electrospinning/sol-gel process.
Journal of Materials Science Letters, 22 (12), pp. 891-893. 2003.

Choi, S. S., Lee, S. G., Joo, C. W., Im, S. S., Kim, S. H.
Formation of interfiber bonding in electrospun poly(etherimide) nanofiber web.
Journal of Materials Science, 39 (4), pp. 1511-1513. 2004.

Chronakis, I. S.
Novel nanocomposites and nanoceramics based on polymer nanofibers using electrospinning
process-A review.
Journal of Materials Processing Technology, 167, pp. 283-293. 2005.

Cowie, M. R., Wood, D. A., Coats, A. J. S., Thompson, S. G., Suresh, V.,
Poole-Wilson, P. A., Sutton G. C.
Survival of patients with a new diagnosis of heart failure: a population based study.
Heart Lung, 83 (5), pp. 505-510. 2000.

Craighead, H. G., Bellan, L. M.
Nanomanufacturing Using Electrospinning.
Journal of Manufacturing Science and Engineering, 131, 034001-1. 2009.

Deitzel, J. M., Kleinmeyer, J. D., Hirvonen, J. K., Tan, N. C. B.

Controlled deposition of Electrospinning Poly (ethylene oxide) Fibers.

Polymer, 42, pp. 8163-8170. 2001.

Drew, C., Liu, X., Ziegler, D., Wang, X.Y., Bruno, F.F., Whitten, J., Samuelson, L.A.,
Kumar, J.

Metal oxide-coated polymer nanofibers.

Nano Letters, 3, pp. 143-147. 2003.

Eschenhagen, T., Fink, C., Remmers, U., Scholz, H., Wattchow, J., Weil, J., Zimmermann,
W., Dohmen, H. H., Schäfer, H., Bishopric, N., Wakatsuki, T., Elson, E. L.

Three-dimensional reconstitution of embryonic cardiomyocytes in a collagen matrix: a new
heart muscle model system.

FASEB Journal, 11 (8), p. 683–694. 1997.

Fujimoto, K. L., Tobita, K., Merryman, W. D., Guan, J. J., Momoi, N., Stolz, D.B., Sacks,
M. S., Keller, B. B., Wagner, W. R.

An elastic, biodegradable cardiac patch induces contractile smooth muscle and improves
cardiac remodeling and function in subacute myocardial infarction.

Journal of the American College of Cardiology, 49 (23), pp. 2292–2300. 2007.

Fujiwara, K.

Separation functional fibers by radiation induced graft polymerization and application.

Nuclear Instruments & Methods in Physics Research Section B-Beam Interactions with
Materials and Atoms, 265, pp. 150-155. 2007.

Greiner, A., Wendorff, J.H.

Electrospinning: A fascinating method for the preparation of ultrathin fibres.

Angewandte Chemie-International Edition, 46 (30), pp. 5670-5703. 2007.

Gu, B. K., Shin, M. K., Sohn, K. W., Kim, S. I., Kima, S. J.

Direct fabrication of twisted nanofibers by electrospinning.

Applied Physics Letters, 90, 263902. 2007.

Han, T., Reneker, D. H., Yarin, A. L.

Buckling with jets in electrospinning.

Polymer, 48, pp. 6064-6076. 2007.

Hawkins, N. M., Petrie, M. C., MacDonald, M. R., Hogg, K. J., McMurray, J. J. V.

QRS duration alone to select patients for cardiac resynchronization therapy: flying in the face of the evidence?

European Heart Journal., 27 (11), pp. 1270–1281. 2006.

Heikkilä, P., Söderlund, L., Uusimäki, J., Kettunen, L., Harlin, A.

Exploitation of Electric Field in Controlling of Nanofiber Spinning Process.

Polymer Engineering and Science, pp. 2065-2074. 2007.

Hellmann, Ch., Belardi, J., Dersch, R. , Greiner, A., Wendorff, J.H., Bahnmueller, S.

High Precision Deposition Electrospinning of nanofibers and nanofiber nonwovens.

Polymer, 50, pp. 1197–1205, 2009.

Huang, Z. M., Zhang, Y. Z., Kotaki, M., Ramakrishna, S.

A review on polymer nanofibers by electrospinning and their applications in nanocomposites.

Composites Science and Technology, 63 (15), pp. 2223-2253. 2003.

Ishii, Y., Sakai, H., Murata, H.

Fabrication of a submicron patterned electrode using an electrospun single fiber as a shadow-mask.

Thin Solid Films, 518, pp. 647–650. 2009.

Ito, Y., Hasuda, H., Kamitakahara, M., Ohtsuki, C., Tanihara, M., Kwon, O. H.

A composite of hydroxyapatite with electrospun biodegradable nanofibers as tissue engineering material.

Journal of Bioscience and Bioengineering, 100, pp.43-49. 2005.

Jaworek, A.,

Micro- and nanoparticle production by electro spraying

Powder Technology, 176 (1), pp. 18-35. 2007.

Jaworek, A., Krupa, A.

Forms of the multijet mode of electrohydrodynamic spraying.

Journal of Aerosol Science, 27 (75). 1996.

Jaworek, A., Krupa, A., Lackowski, M., Sobczyk, A.T., Czech, T., Ramakrishna, S.,
Sundarrajan, S., Pliszka, D.

Nanocomposite fabric formation by electrospinning and electro spraying technologies.

Journal of Electrostatics, 67, pp. 435–438. 2009.

Jaworek, A., Sobczyk, A.T.,

Electro spraying route to nanotechnology: An overview.

Journal of Electrostatics, 66, pp. 197-219. 2008.

Kanai, H.

Propagation of spontaneously actuated pulsive vibration in human heart wall and in vivo
viscoelastic estimation.

IEEE Ultrasonics, Ferroelectrics, and Frequency Control, 52, pp. 1931-1942. 2005.

Kim, G. H.

Electrospinning Process Using Field-Controllable Electrodes.

Journal of Polymer Science: Part B: Polymer Physics, 44, pp. 1426–1433. 2006.

Kim, G. H., Han, H., Park, J. H., Kim, W. D.

An applicable electrospinning process for fabricating a mechanically improved nanofiber
material.

Polymer Engineering and Science, 47 (5), pp. 707-712. 2007.

Kim, G. H., Kim, W. D.

Formation of oriented nanofibers using electrospinning.

Applied Physics Letters, 88, 233101. 2006.

Kim, G. H., Kim, W. D.

Designed PCL Nanofibers Fabricated Using a Modified Electrohydrodynamic Process for Tissue Engineering.

Journal of Manufacturing Science and Engineering, 130, 021006-1. 2008

Koh, G.Y., Klug, M.G., Soonpaa, M.H., Field, L.J.

Differentiation and long-term survival of C2C12 myoblast grafts in heart

Journal of Clinical Investigation, 92 (3), pp. 1548–1554. 1993a.

Koh, G.Y., Soonpaa, M.H., Klug, M.G., Field, L.J.

Long-term survival of AT-1 cardiomyocyte grafts in syngeneic myocardium.

American Journal of Physiology, 264 (5), H1727–H1733. 1993b.

Kohli, S. K., Elliott, P.

Cardiac resynchronization therapy: the procedure and progress so far.

British Journal of Hospital Medicine, 66 (8), pp. 469–473. 2005.

Künzli, N., Kaiser, R., Medina, S., Studnicka, M., Chanel, O., Filliger, P., Herry, M., Horak J. F., Puybonnieux-Textier, V., Quénel, P., Schneider, J., Seethaler, R., Vergnaud, J. C., Sommer, H.

Public-health impact of outdoor and traffic-related air pollution: a European assessment.

The Lancet, 356, pp. 795-801. 2000.

Lee, S.-J., Cho, N.-I., Lee, D. Y.

Effect of collector grounding on directionality of electrospun titania fibers

Journal of the European Ceramic Society, 27, pp. 3651–3654. 2007.

-
- Li, D., Ouyang, G., McCann, J. T., Xia, Y.
Collecting Electrospun Nanofibers with Patterned Electrodes.
Nano Letters, 5 (5), pp. 913-916. 2005.
- Li, D, Xia, Y,
Electrospinning of Nanofibers: Reinventing the Wheel?
Advanced Materials, 16, p. 1151. 2004.
- Loebe, M., Soltero, E., Thohan, V., Lafuente, J.A., Noon, G.P.,
New surgical therapies for heart failure.
Current Opinion in Cardiology, 18 (3), pp. 194–198. 2003.
- Martinez, C., Tzur, A., Hrachian, H., Zebede, J., Lamas, G.A.
Pacemakers and defibrillators: recent and ongoing studies that impact the elderly
American Journal of Geriatric Cardiology, 15(2), pp. 82-87. 2006.
- Nagueh, S.F., Shah, G., Wu, Y., Torre-Amione, G., King, N.M.P., Lahmers, S., Witt, K.
Becker, Labeit, S., Granzier, H. L.
Altered Titin Expression, Myocardial Stiffness, and Left Ventricular Function in Patients
With Dilated Cardiomyopathy.
Circulation, 110 (2), pp. 155–162. 2004.
- Nakano, K., Sugawara, M., Ishihara, K., Kanazawa, S., Corin, W., Denslow, S., Biederman,
R. W. W., Carabello, B. A.
Myocardial stiffness derived from end-systolic wall stress and logarithm of reciprocal of
wall thickness. Contractility index independent of ventricular size.
Circulation, 82 (4), pp. 1352–1361. 1990.
- Norris, I. D., Shaker, M. M., Ko, F. K., MacDiarmid, A. G.
Electrostatic fabrication of ultrafine conducting fibers:
polyaniline / polyethylene oxide blends
Synthetic Metals, 114, pp. 109-114. 2000.

Pliszka, D., Sundarrajan, S., Jaworek, A., Krupa, A., Lackowski, M., and Ramakrishna, S.
Optimization of Electrospray Process by PIV in Nanostructured Membrane Preparation.
CIMTEC Proceeding of the 3rd International Conference on Smart Materials, Structures and
Systems - Smart Textiles, 60, June 2008, Acireale, Italy, pp. 117-122.

Packer, M.

The impossible task of developing a new treatment for heart failure.

Journal of Cardiac Failure, 8 (4), pp. 193–196. 2002.

Porter, M. C.

Handbook of Industrial Membrane Technology.

Park Ridge, New York, USA: Noyes Publications.1990.

Prabhakaran, M. P., Venugopal, J. R., Ramakrishna, S.

Mesenchymal stem cell differentiation to neuronal cells on electrospun nanofibrous
substrates for nerve tissue engineering.

Biomaterials, 30, pp. 4996–5003. 2009.

Radisic, M., Deen W, Langer R, Vunjak-Novakovic G.

Mathematical model of oxygen distribution in engineered cardiac tissue with parallel channel
array perfused with culture medium containing oxygen carriers.

American Journal of Physiology - Heart and Circulatory Physiology, 288, H1278–H1289.
2005.

Ramakrishna, S., Fujihara, K., Teo, W.-E., Lim, T.-C., Ma, Z.

An Introduction to Electrospinning and Nanofibers.

Singapore: World Scientific Publishing CO.Pte. Ltd. 2005.

Reneker, D. H., Yarin, A. L.

Electrospinning jets and polymer nanofibers.

Polymer, 49, pp. 2387-2425. 2008.

-
- Rojas-Chapana, J.A., Tributsch, H., Fink, D., Petrov, A.
Colloidal assembly and functionalization of pore channels in polymer foils.
Journal of Porous Materials, 12, pp. 215-224. 2005.
- Patanaika, A., Jacobsa, V., Anandjiwalaa, R. D.
Performance evaluation of electrospun nanofibrous membrane
Journal of Membrane Science, 352, pp. 136–142. 2010.
- Roso, M., Sundarrajan, S., Pliszka, D., Ramakrishna, S., Modesti, M.
Multifunctional membranes based on spinning technologies: the synergy of nanofibers and nanoparticles.
Nanotechnology, 19 (28), pp. 6. 2008.
- Rump, J., Klatt, D., Braun, J., Warmuth, C., Sack, I.
Fractional encoding of harmonic motions in MR elastography.
Magnetic Resonance Medicine, 57, pp. 388-395. 2007.
- Sack, I., Rump, J., Elgeti, T., Samani, A., Braun, J.
MR Elastography of the Human Heart: Noninvasive Assessment of Myocardial Elasticity Changes by Shear Wave Amplitude Variations.
Magnetic Resonance in Medicine, 61, pp. 668-677. 2009.
- Secasanu, V. P., Giardina, C. K., Wang, Y.
A Novel Electrospinning Target to Improve the Yield of Uniaxially Aligned Fibers.
Biotechnology Progress, 25 (4). 2009.
- Senning, A., Thorac. J.
Fascia lata replacement of aortic valves.
Journal of Thoracic and Cardiovascular Surgery, 54, pp. 465–470. 1967.

Soonpaa, M.H., Koh, G.Y., Klug, M.G., Field, L.J.

Formation of nascent intercalated disks between grafted fetal cardiomyocytes and host myocardium.

Science, 264 (5155), pp. 98–101. 1994.

Sundarrajan, S., Ramakrishna, S.

Fabrication of nanocomposite membranes from nanofibers and nanoparticles for protection against chemical warfare stimulants.

Journal of Materials Science, 42 (20), pp. 8400-8407. 2007.

Teo, W. E., Kotaki, M., Mo, X. M., Ramakrishna, S.

Porous tubular structures with controlled fibre orientation using a modified electrospinning method.

Nanotechnology, 16, pp. 918-924, 2005.

Thavasi, V.; Singh, G.; Ramakrishna, S.

Electrospun nanofibers in energy and environmental applications.

Journal of Energy and Environmental Science., 1, pp. 205. 2008.

Torrent-Guasp, F., Buckberg, G. D., Clemente, C., Cox, J. L., Coghlan, H. C.,

Coghlan, H. C., Gharib, M.

The Structure and Function of the Helical Heart and its Buttress Wrapping - The Normal Macroscopic Structure of the Heart.

Seminars in Thoracic and Cardiovascular Surgery, 13, p. 301-319. 2001.

Venugopal, J., Low, S., Choon, A. T., Ramakrishna, S.

Interaction of Cells and Nanofiber Scaffolds in Tissue Engineering

Part B: Applied Biomaterials, 84B, p. 34–48. 2008.

Venugopal, J., Prabhakaran, M. P., Zhang, Y., Low, S., Choon, A. T. and Ramakrishna, S.
Biomimetic hydroxyapatite-containing composite nanofibrous substrates for bone tissue engineering.

Journal of Phil. Trans. R. Soc. A, 368, p. 2065-2081, 2010

Vogel, G.

Embryonic Stem Cells: Stem Cells Not So Stealthy After All.

Science, 297, pp. 175-177. 2002.

Walsh, R.G.

Design and Features of the Acornm CorCop Cardiac Support Device: The Concept of Passive Mechanical Diastolic Support

Heart Failure Reviews, 10 (2), pp. 101–107. 2005.

Watanabe, S., Shite, J., Takaoka, H., Shinke, T., Imuro, Y., Ozawa, T., Matsumoto, D., Ogasawara, D., Paredes, O. L., Yokoyama, M.

Myocardial stiffness is an important determinant of the plasma brain natriuretic peptide concentration in patients with both diastolic and systolic heart failure.

European Heart Journal, 27 (7), pp. 832–838. 2006.

Wu, Y., Carnell, L. A., Clark, R. L.

Control of electrospun mat width through the use of parallel auxiliary electrodes.

Polymer, 48, p. 5653-5661. 2007.

Xu, L.

A mathematical model for electrospinning process under coupled field forces.

Chaos, Solitons and Fractals, 42, p. 1463–1465, 2009.

Yan, H., Liu, L., Zhang, Z.

Alignment of electrospun nanofibers using dielectric materials.

Applied Physics Letters, 95, 143114. 2009.

Yang, C., Jia, Z., Liu, J., Li, Q., Hou, L., Wang, L., Guan, Z.
Effect of electric field distribution uniformity on electrospinning.
Applied Physics Letters, 103, 104307. 2008.

Yang, C., Jia, Z., Liu, J., Xu, Z., Guan, Z., Wang, L.
Guiding Effect of Surface Electric Field of Collector Deposited Electrospinning Fibers.
IEEE Transactions on Dielectrics and Electrical Insulation, 16 (3), pp. 785- 792. 2009.

Young, J.B., Mills, R.M.
Clinical Management of Heart Failure.
Caddo, Oklahoma, USA: Professional Communications. 2004.

Zhang, J.-F., Yang, D.-Z., Nie, J.
Effect of electric potential and coulombic interactions on electrospinning nanofiber
distribution.
Polymer International, 57, pp. 1194–1197. 2008.

Zhang, Y. Z., Su, B., Verugopal, J., Ramakrishna, S., Lim, C. T.
Biomimetic and bioactive nanofibrous scaffold from electrospun composite fibers.
International Journal of Nanomedicine, 2 (4), pp. 623-638. 2007.